Faculty of Science

Microstructural evolution of ice under simple shear deformation

Carina Liebl

Degree of Master of Science (120 credits)
with a major in Earth Sciences
60 hec

Department of Earth Sciences
University of Gothenburg
2020 B1120

UNIVERSITY OF GOTHENBURG

UNIVERSITY OF GOTHENBURG
Department of Earth Sciences
Geovetarcentrum/Earth Science Centre

Microstructural evolution of ice under simple shear deformation

Carina Liebl

ISSN 1400-3821

B1120
Master of Science (120 credits) thesis
Göteborg 2020

Mailing address
Geovetarcentrum
S 405 30 Göteborg

Address
Geovetarcentrum
Guldhedsgatan 5A

Telephone
031-786 19 56

Geovetarcentrum
Göteborg University
S-405 30 Göteborg
SWEDEN

Table of content

Abstract

To investigate microstructure in ice deformed under simple shear conditions experiments were performed with artificial polycrystalline ice and natural ice samples form Vatnajökull glacier in Iceland. A new deformation apparatus was tested and results from deformation were compared to literature to validate the method. Boundary conditions for deformation were varied. Experiments were performed at -5°C and -10°C and three strain rates were applied (2.5×10^{-7} 1/s, 1.25×10^{-6} 1/s, 2.5×10^{-6} 1/s). It is shown that the natural samples, which contain only 2-3 grains, provide a close-up image on specific situation. This gives the opportunity to study them in detail.

A special focus is set on the behaviour of grain boundaries during deformation. A preferred arrangement with at least one side of the boundary close to a prism face is seen. While in warm or slow deformations a tendency to favour boundaries with a combination of $\{\bar{1}\bar{1}22\}$ and $\{10\bar{1}2\}$ faces. The type of crystall face and their orientation towards deformation direction befor deformation has an major influence on the development during deformation.

Brittle fractures were observed in the samples, which immediately filled with small new grains. This was only observed in samples deformed at -10°C but no dependency to strain rate was oberved.

1. Introduktion

Thinking about ice can be very diverse, from tasty ice cream in the summer to huge amounts of snow during wintertime. But lately the quick reduction of cryospheric regions on earth get more and more attention, especially as it is consequence of the changing climate and will have a major impact for the future (Hock *et al.*, 2019; Meredith *et al.*, 2019). The huge ice sheets also function as climate archives and provide insights through records taken from deep ice cores (review of Faria *et al.*, 2014) gives a nice overview on the topic). An important assumption for climate reconstruction with data from deep ice cores is that all the layers are stratigraphically correct, which is why they these cores are taken from central areas of glaciers. But this must not be true as suggested from for example Waddington *et al.* (2001), Wolovick *et al.* (2014) and Bons *et al.* (2016) . A good understanding of structures in micro and macro scale forming during the movement within an ice sheet as well as understanding how the mechanisms work is therefore beneficial.

The natural occurring forms of frozen water have quite a variety of appearances. From snowflakes transitioning over firn to ice, or frozen lakes and sea ice. Due to the different settings of formation, and therefore different history, the microstructures look different, as they combine a history depending on temperature, strain, strain rate and impurities (Petrenko & Whitworth, 2002; Schulson & Duval, 2009; Cuffey & Paterson, 2010). Although all these forms crystallize as ice Ih in a hexagonal crystal system, which is the on earth most common crystal form, their appearance shows a wide variety. Depending on an existing temperature gradient during freezing the ice can form elongated grains with a favored growth direction along the gradient. Temperature ranges have a major impact on the growing pattern on ice, as the kinetic favored crystal face is directly liked to certain temperature ranges (Nishinaga, 2015). This leads to for example columnar ice crystals with most of the <c>-axis being perpendicular to the temperature gradient (Grennerat *et al.*, 2012).

Also, the abundance of solutes during freezing has an impact. For example, the amount of salt in the water changes the freezing behavior, not only by decreasing the freezing temperature. The salt does not fit well into the crystal lattice of ice. Therefore, the remaining water relatively enriches in salt while the ice freezes. This brine can be trapped as an inclusion in the ice or sink deeper into the water reservoir producing a layer of very cold and salty water. Leading to a higher amount of dislocations during formation, which is why solutes influence deformation behavior of ice (Alley *et al.*, 1986; Alley *et al.*, 1986; Paterson, 1991; Alley & Woods, 1996; Thorsteinsson *et al.*, 1999; Durand *et al.*, 2006; Cyprych *et al.*, 2016). Impurities in form of solid particles or bubbles also change the behavior compared to pure ice.

The most common form of ice, the hexagonal crystal system covers most of the temperature/pressure habitats on earth with its stability field. Although it is only one of the possibilities for ice to crystallize (Petrenko & Whitworth, 2002; Cuffey & Paterson, 2010). Figure 1.1 shows the variety of lattice forms ice can form under right conditions. The natural occurring ice Ih plots in the blue area in lower left corner of the diagram. The only other natural possible form of ice on earth is cubic which only forms under special circumstances as described for example by (Whalley, 1983; Murray *et al.*, 2005; Thürmer & Nie, 2013).

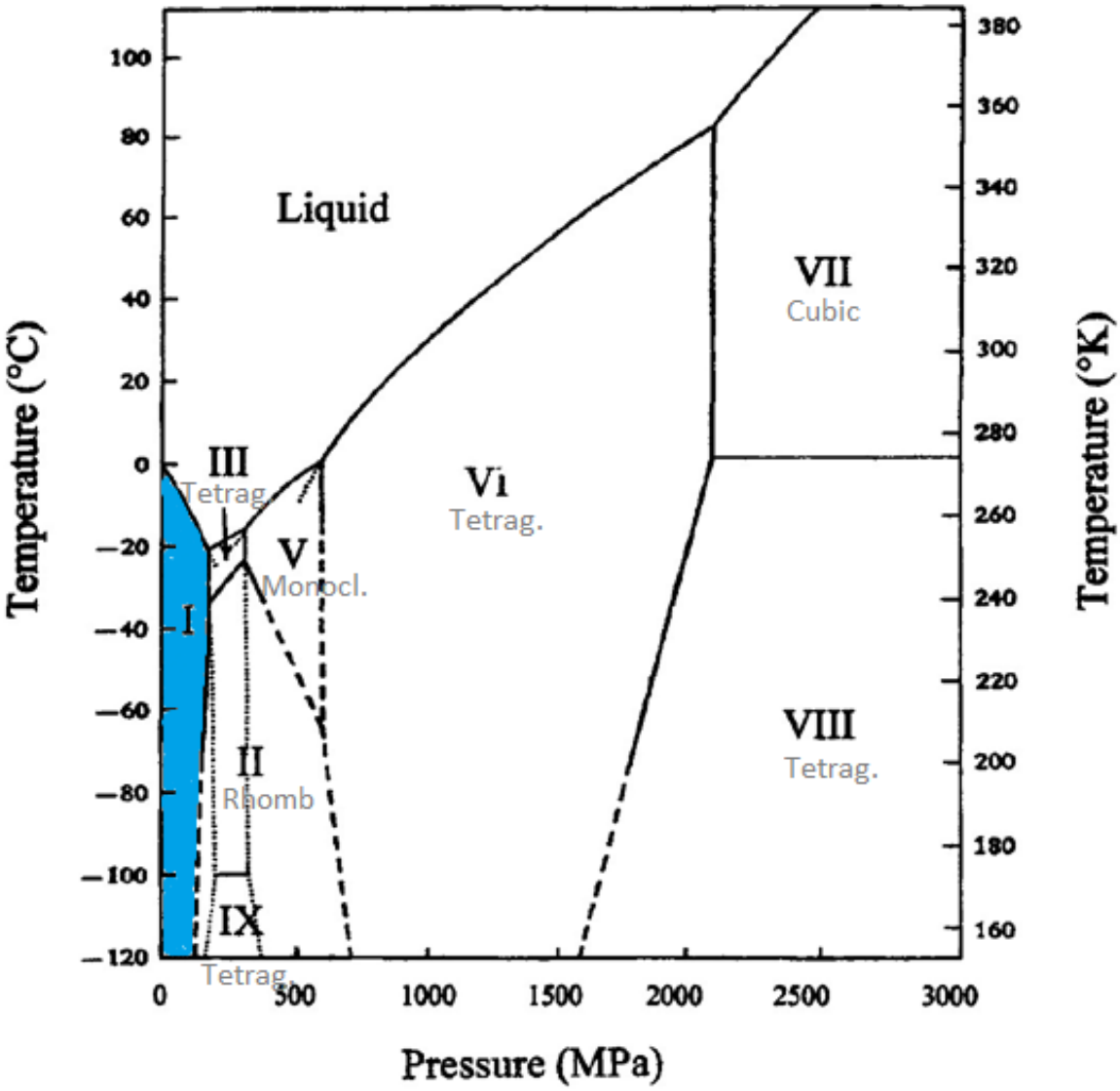

Figure 1.1: Phase diagram of water, including different crystal forms of ice. The natural on earth occurring hexagonal ice Ih is marked in blue (after Cheftel et al., 2000).

The crystal lattice of ice is similar to quartz which also features the hexagonal crystal system. While the distribution in quartz is because of the sp^3 hybridized silica giving an equal angle of 109.5° between the four bonding directions, for ice it is not as easy. Looking at a single water molecule the oxygen has two bonds with one hydrogen respectively and two free electron pairs. Following the VSEPR (Valence Shell Electron Pair Repulse) model the free electron pairs need more space leading to a slightly smaller angle between the two H-O bonds of 104.5°. Still water molecules arrange in a crystal lattice with oxygen tetrahedrally surrounded by the other oxygens (Bernal & Fowler, 1933; Binnewies *et al.*, 2016). This variation in angle and the resulting changes in the lattice might be a reason why not all crystal faces of quartz appear in an ice crystal.

As many crystal faces and slip systems from quartz are also abundant in ice (see Figure 1.2) it is an ideal analogue material for quartz rich crustal rocks. Giving the opportunity to perform in situ experiments and observe microstructures (Wilson *et al.*, 2014).

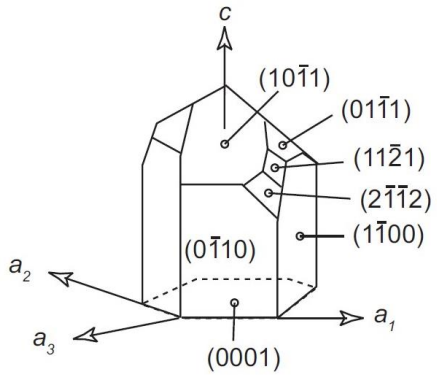

	QUARTZ	ICE
Glide plane	**Glide direction**	**Glide direction**
(0001) *basal*	*a* <$\bar{1}2\bar{1}0$>	*a* <11$\bar{2}$0> <0001> climb <11$\bar{2}$3>climb
{$\bar{1}0\bar{1}0$} *prism*	*a* <$\bar{1}2\bar{1}0$> *c* <0001> *c* + *a* <$\bar{1}2\bar{1}3$>	*a* <11$\bar{2}$0> *c* <0001>
{10$\bar{1}$1} *(+) rhomb*	*a* <$\bar{1}2\bar{1}0$> *c* + *a* <$\bar{1}\bar{1}$23>	*c* <0001> *c* + *a* <11$\bar{2}$3>
{01$\bar{1}$1} *(-) rhomb*	*a* <$\bar{1}2\bar{1}0$> *c* + *a* <$\bar{1}\bar{1}$23>	*c* <0001> *c* + *a* <11$\bar{2}$3>
{2$\bar{1}\bar{1}$1}, {11$\bar{2}$1} *trigonal dipyramid*	*c* + *a* <$\bar{1}2\bar{1}3$> *c* + *a* <$\bar{1}\bar{1}$23>	
{2$\bar{1}\bar{1}$2}, {11$\bar{2}$2} *trigonal dipyramid*	*c* + *a* <$\bar{1}\bar{1}$23>	*c* + *a* <1123>

Figure 1.2: Comparison of planes and glide directions of quartz and ice (Wilson et al., 2014).

But still there are differences between the two crystal lattices. The c/a axis ratio of quartz (1.109, Kimizuka *et al.*, 2007) and ice (1.628, Petrenko & Whitworth, 2002) differs leading to slightly different angles of the crystal faces to the <c>-axis. It is known that the length of the crystallographic axis changes with temperature, but the c/a ratio remains constant

(Petrenko & Whitworth, 2002) and was therefore used for the calculation of the angles between crystal faces and crystallographic <c>-axis.

A focus in this current study will be set on the behavior of the grain boundaries. Therefore, a brief introduction to crystal faces and grain boundaries will be given in the following.

The water molecules in the ice Ih crystal follow the Bernal-Fowler rules, also referred to as the 'ice rules' (Bernal & Fowler, 1933). They say near to each oxygen two hydrogen atoms need to be located and only one hydrogen lies on each O-O bond. Following these rules, the arrangement of the molecules builds up a disordered structure in relation to the orientation of the water towards each other in respect to the spatial distribution of the hydrogen bonds to the hydrogen bridges. The disorder leads to a large amount of remaining zero-point entropy (3.41 J $°C^{-1}$ mol^{-1}; Pauling, 1935; Schulson & Duval, 2009) depending on the individual distribution (Ramirez *et al.*, 1999; Nishinaga, 2015). Whit this in mind and the fact that each crystal face features a certain arrangement of the oxygen atoms (Figure 1.3) leads to the idea that different crystal faces feature different stability levels based on energetic sinks on different levels. Measurements of the neutron refraction for the basal and the prismatic face for deuterated ice by Li *et al.* (1994) show the difference for the electron density on the two faces. Differences in the energy levels need to very small, as measurements of the surface energy of ice to ice interfaces show an energy of 0.065±0.003 J m^{-2} independent of the measured combination of crystal faces (Ketcham & Hobbs, 1969). This effect of an irregular electron density pattern on crystal surfaces is also studied with analogue materials referred to as 'spin ice' used in experimental studies (Ramirez *et al.*, 1999; Fennell *et al.*, 2009; Morris *et al.*, 2009). Materials with this specific feature were first discovered in 1997 by Harris *et al.*, 1997) and a review on the topic summarizing the huge amount of publications is given by Bramwell & Harris, 2020.

This arrangement of oxygen atoms also has an impact on growth kinetics for the different faces and is connected to temperature (Nada *et al.*, 2004; Nada & Furukawa, 2005). By using this, ice samples with specific orientations can be made, as for example columnar shapes with preferred growth in direction of the a-axis by applying a temperature gradient within the range for growth in this specific direction (Grennerat *et al.*, 2012). The combination of growth kinetics and higher abundances of certain crystal faces in a crystal lead to a statistical higher abundance of prism faces compared to others. The hexagonal crystal system contains for example six prism faces but only two basal planes (see Figure 1.3).

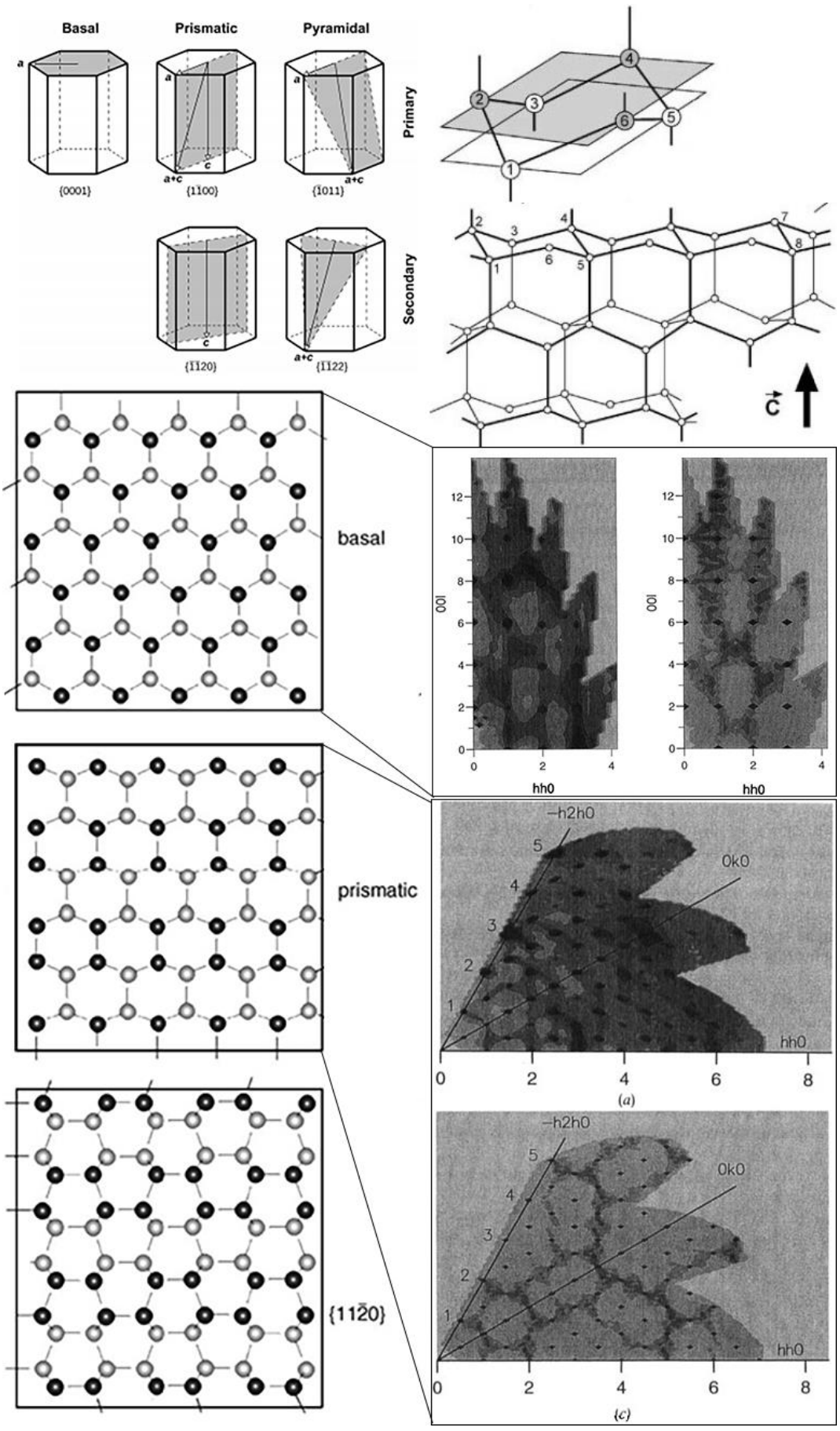
Basal
Prismatic
Pyramidal
Primary
Secondary
{0001}
{1100}
{1011}
{11̄20}
{11̄22}
basal
prismatic
{11$\bar{2}$0}
hh0
−h2h0
0k0
(a)
(c)

Figure 1.3: Upper left: Orientation of crystal faces in the hexagonal system. Upper right: Arrangement of the oxygen atoms within the rings containing six atoms. Example for the placement in the basal plane with alternating oxygens in the upper and lower subplane. And a sketch of the 3D arrangement for the lattice. Lower left: Positioning of oxygen atoms on basal, prismatic and {1 1 -2 0} crystal faces. Black indicates atoms in the upper subplane and white in the lower subplane. Lower right: Neutron scattering pattern for the basal and prismatic face for deuterated ice from experimental measurement (darker gray) and from simulations using the Bernel-Fowler rule (after: Li et al., 1994; Nada & Furukawa, 2005; Cuffey & Paterson, 2010; Faria et al., 2014).

Looking on a polycrystalline aggregate of ice grain the boundaries become more prominent due to their higher abundance. These are planes of misorientation in the lattice. Depending on the angle of misorientation between two grains it is distinguished between a subgrain boundary (SGB) and a grain boundary (GB). As the misorientation angle can change continuously there is no clear point on which a subgrain boundary is determined a grain boundary. For polar ice no higher misorientation angles as 5° have been found for subgrain boundaries (Weikusat *et al.*, 2011). Also subgrain boundaries can show a variety of diverse types (Weikusat *et al.*, 2011; Weikusat *et al.*, 2017). The positioning and occurrence of subgrain boundaries influence grain boundary migration mechanisms, as a migration tends to follow a path of high misorientation densities which includes subgrain boundaries (Steinbach *et al.*, 2017).

With the knowledge of how the crystal lattice is built and how aggregates of several crystals are connected now mechanisms happening during deformation are discussed. The activation of different slip systems in the lattice depends on the resolved shear stresses and happen in ice mainly on the basal plane (Weertman, 1983; Wilson *et al.*, 2014). As the activation energy for basal slip is 60 to 100 times smaller than for any other system (Wakahama, 1967; Duval *et al.*, 1983; Ashby & Duval, 1985) a non-basal slip is generally not significant (Duval *et al.*, 1983). Although Chauve *et al.* (2017) found evidence for a possibly bigger amount of non-basal slip than expected. Moving dislocations and the resulting rearrangement in the crystal lattice lead to effects changing the <c>-axis orientation leading to formation of kink bands and subgrain boundaries. Also changes regarding the grain shape and boundary movement are related to dislocation movement or diffusive effects (Petrenko & Whitworth, 2002). The number of dislocations increases rapidly with application of stress (Montagnat & Duval, 2004). New dislocations can be generated due to shear along discrete atomic planes in one crystal or due to slip along grain boundaries leading to a focused stress at the boundary of a neighboring grain (Hooke, 2020)(Figure 1.4 A). Another possibility to generate new dislocations is a Frank-Read source, which consists of a dislocation positioned between two points where the dislocations position is fixed. Applied stress leads to a bowed dislocation until it meets itself again. As the dislocation at this point are direct opposites, they locally annihilate

themselves. This leads to a dislocation in a ring around the original source and a second new dislocation between the originally fixed points (Cottrell, 1953; Weertman, 1955; Hooke, 2020) (Figure 1.4 B).

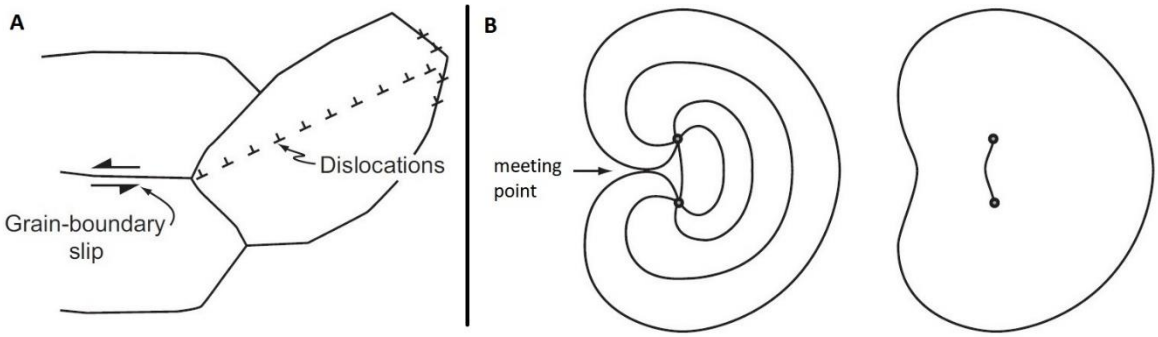

Figure 1.4: (A) Generation of dislocations due to slip along grain boundaries leading to a focused stress at the boundary of a neighboring grain. (B) Generation of dislocations at a Frank-Read source. Lines in the left picture represent progressively further bowed dislocation until they meet. Right picture shows dislocation ring around the new dislocation at the fixed points. (from Hooke, 2020).

During deformation different mechanisms can occur, leading to increasing or decreasing grain sizes and changes in shape and grain boundary traces. Recrystallization processes occurring during deformation are referred to as dynamic recrystallization. This combines processes such as polygonization, migration recrystallization and nucleation. Further possible mechanisms are grain boundary migration (occasionally goes along with grain growth), grain boundary rotation or grain boundary sliding (in general only for very small grain sizes) (Bresser *et al;* Doherty *et al.*, 1998; Bresser *et al.*, 2001; Petrenko & Whitworth, 2002; Cuffey & Paterson, 2010; Faria *et al.*, 2014; Chauve *et al.*, 2015).

Many studies on natural ice cores have been done throughout the years (La Chapelle *et al;* Vallon *et al.*, 1976; Fisher & Koerner, 1986; Lipenkov *et al.*, 1989; Alley & Woods, 1996; Jun *et al.*, 1998; Weikusat *et al.*, 2009; Faria *et al.*, 2014; Eichler *et al.*, 2017; Steinbach *et al.*, 2017; Weikusat *et al.*, 2017; Haseloff *et al.*, 2019). To understand the mechanisms leading to the found microstructures many laboratory deformation experiments were done with variation of temperature and strain rate (e.g. Bouchez & Duval, 1982; Jacka, 1984; Cole, 1987; Wilson & Zhang, 1994; Goldsby & Kohlstedt, 2001; Wilson *et al.*, 2003; Wilson & Peternell, 2012; Piazolo *et al.*, 2013; Peternell & Wilson, 2016; Craw *et al.*, 2018; Prior *et al.*, 2018; Journaux *et al.*, 2019; Peternell *et al.*, 2019; Qi *et al.*, 2019; Fan *et al.*, 2020). Different techniques to induce the deformation were used. For 3D experiments deforming small ice cores deformation can be induced ether trough torsion by rotation of the sample core around the long axis (Journaux *et al.*, 2019) or compression due to

pistons cut with a specified angle towards movement direction (Qi *et al.*, 2019). A big disadvantage of these kinds of experiments is that only the situation before or after a deformation can be directly observed. Therefore, thin sections need to be cut for each observed step individually. To prevent unwanted annealing processes in the deformed sample during the time until sections are cut, they need to be stored very cold immediately. Also, material from start and end are not the same core. This on the other hand is an advantage of 2D deformation experiments, as thin sections are deformed and observed during deformation. Giving the opportunity to observe the microstructures *in situ*. As the thin section sample is placed between glass plates for this kind of deformation experiments, the influence of the glass needs to be considered, as it can restrict movements in certain directions (Peternell *et al.*, 2019). Depending on the orientation of the grain the main slip happening on the basal plane is glass dependent or not (Figure 1.5).

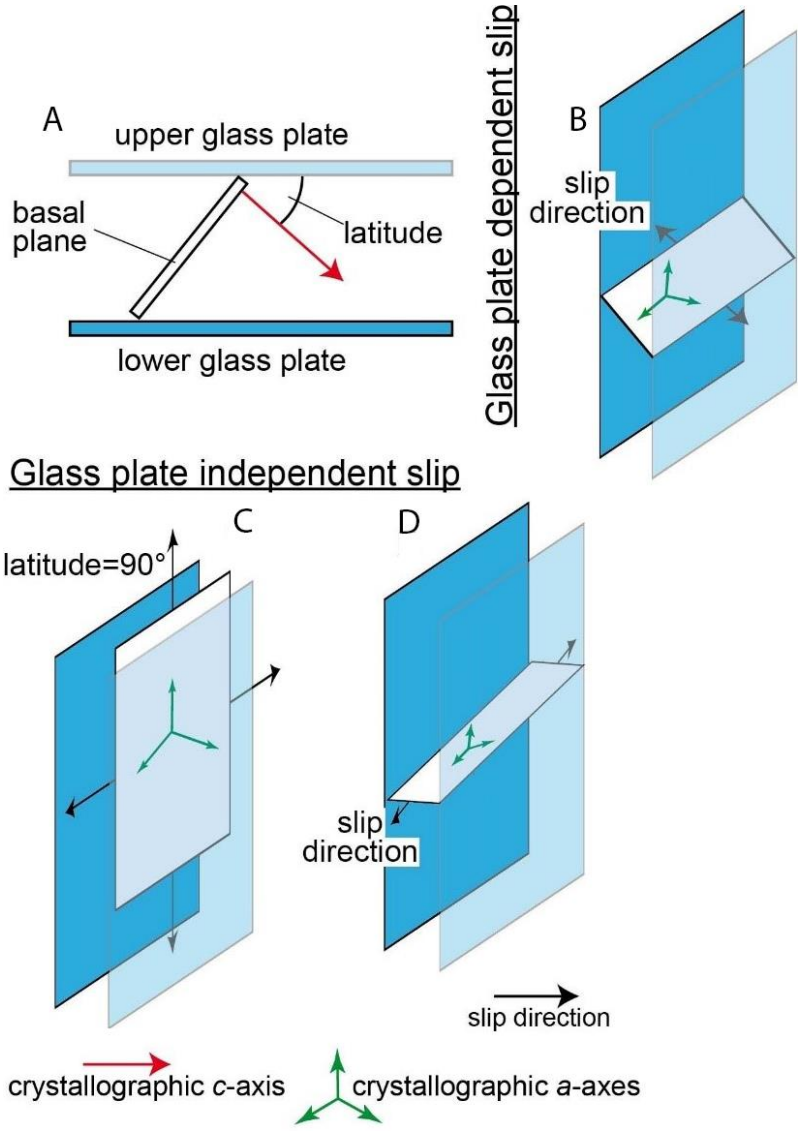

Figure 1.5: Influence of the glass plate on the movement possibilities for slip on the basal plane. (after Peternell et al., 2019).

Slip parallel to the glass is not dependent. The restriction from the glass can induce prismatic slip and/or kinking (Wilson & Zhang, 1994; Peternell *et al.*, 2019). During experiments for this thesis the ice samples do not have direct contact with the glass, as they are placed in between layers of silicon oil. Even though the oil is softer than the glass, the phase boundary still has the same effect as the glass.

Results from 2D experiments show same results in terms of grain size evolution, fabric development and observed microstructures (see references for experimental studies in 2D and 3D listed above). Three phases of creep during deformation are distinguished. The initial primary creep is dominated by grain boundary migration during hardening. The second phase (secondary creep) is marked by dynamic recrystallization up to reaching a steady-state creep (tertiary creep) where grain size increasing and decreasing effects are in balance (Schulson & Duval, 2009; Wilson *et al.*, 2014). Figure 1.6 shows the strain rate variation with strain for constant applied stress.

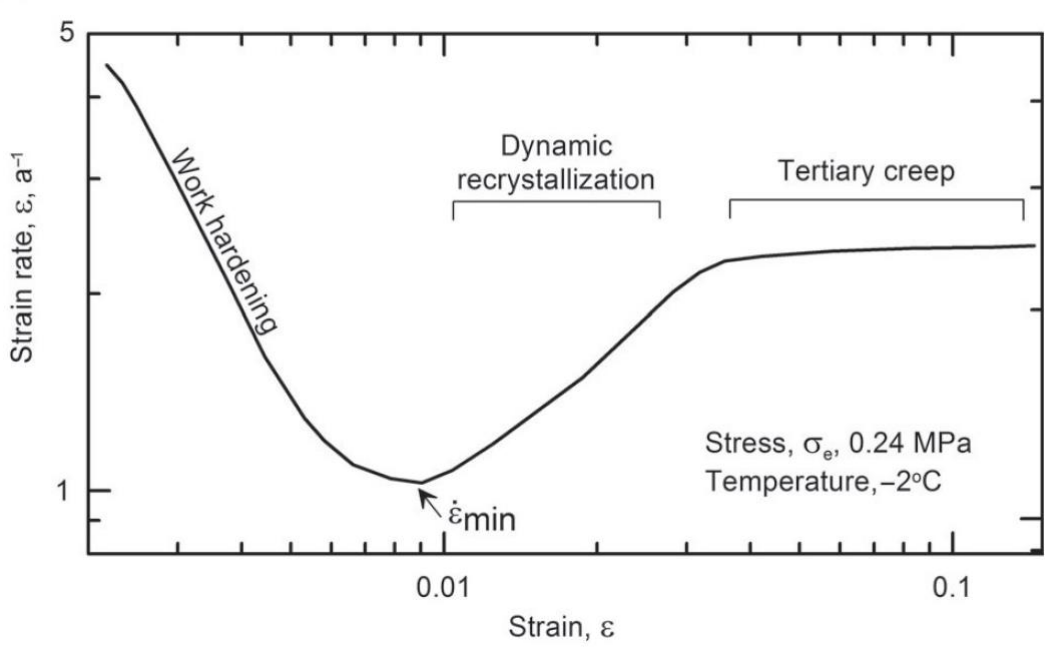

Figure 1.6: Phases of creep for a constant applied stress. Work hardening during primary creep, dynamic recrystallization during secondary creep and steady-state for tertiary creep (from Hooke, 2020) Copyright: International Glaciological Society).

Boundary conditions like strain rate, temperature can shift the time needed to reach the different creep phases. Also, a second phase can influence the behavior during deformation. Second phase articles disturb the crystal lattice, as they don't fit in and disturb migration of boundaries (pinning effect). This leads to faster deformation as some pathways are disturbed (Weertman, 1968; Middleton *et al.*, 2017; Wilson *et al.*, 2018; Saruya *et al.*, 2019).

The aim of this study is to show if the method used is valid to induce simple shear deformation *in situ*, and a special focus is set on the behavior of the grain boundaries to see if a dependence the boundary conditions, such as temperature, strain or strainrate, can be drawn.

2. Methods

The following sections gives an overview of the used material and methods/software. The preparation of the ice used, artificial as well as natural samples, is described. The deformation apparatus is explained and the functioning of the fabric analyzer as measuring instrument is shown. And the used software for the later analysis is listed and briefly mentioned what it is used for.

2.1 Sample preparation

Deformations were performed on artificial and natural ice samples. The preparation of the artificial ice samples takes two days plus an annealing time of several weeks. The necessary steps will be explained in the following. Picking a suitable section from the natural samples is much faster and the procedure will be explained afterwards.

Artificial, polycrystalline ice

The artificial, polycrystalline ice samples were produced following the procedure for standard ice (Stern *et al.*, 1997; Prior *et al.*, 2015) with slight modifications. Sieved ice grains, made from precooked distilled water, with grain sizes of 300-500µm and 0.5-1mm were packed into a cylindric mold. For each mold, an equal amount of ice grains (30g) was used. Figure2.1 shows a schematic sketch of the molds. The sample preparation press features four identical molds attached to an aluminum base plate. The molds have an inner cylinder made of polymer material, it is closed on the bottom by an aluminum plug with small holes and on the top by a hollow stamp. This system is connected to a water tank filled with pre-cooked distilled water from the bottom and a vacuum pump from the top. All connecting tubes are split equally in length and diameter to connect all four molds and are joined in the same way after passing the molds. The outer cylinder consists of a polymer material and serves as an isolation.

The sample preparation press is pre-cooled to -25°C and filled with the seeding grains. The whole system is connected and rests in an ice-water-bath for about 10-12 hours. During this time the press, seeding grains and distilled water in the tank equilibrate at a

temperature of 0°C. The system is then evacuated for several minutes and then flooded with the distilled water filling the cylinders and therefore the pores in between the seeding grains from bottom to top. The sample press then is disconnected from the water tank and vacuum pump. Closed at the ends of the tubes to prevent contamination. And set to rest at -25°C on a cold metallic surface for at least 12 hours. As the sides of the mold are isolated by the outer cylinder the mixture of seeding grains and water in the mold will freeze from the bottom to the top. The ice cores are extracted from the mold, vacuum packed in foil and laid to rest in an annealing bath at -3°C for at least 2-3 weeks.

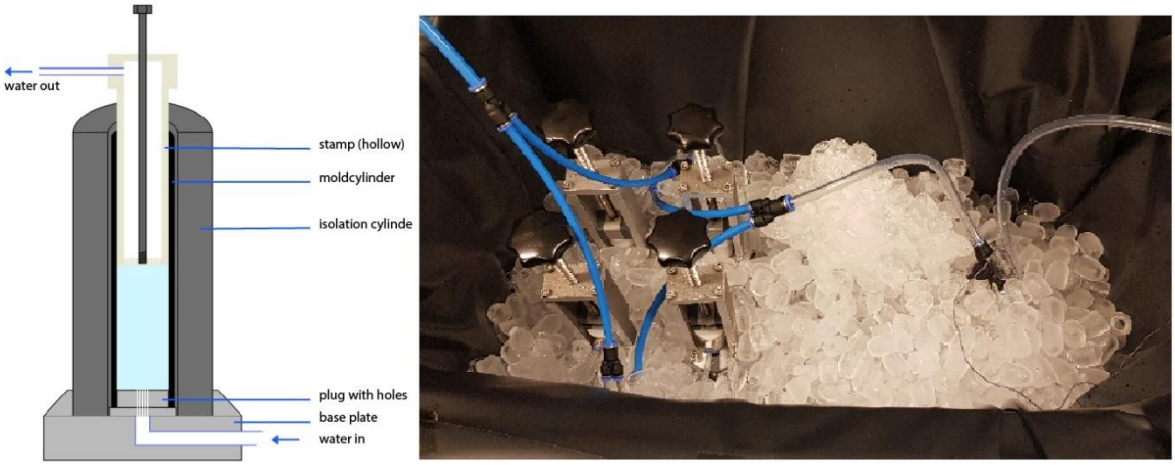

Figure 2.1: Left: schematic sketch of a mold from the sample preparation press. Right: assembled sample preparation press resting in the ice-water-bath with the four identical molds connected to the water reservoir on the right.

In this time the grains will grow and even out their grain boundaries leading to samples with equally distributed grain size, straight grain boundaries and a randomly distributed <c>-axis orientation.

Natural ice

Natural ice samples used originate from Vatnajökull glacier in Iceland (2.2). As the samples feature large grain sizes, which leads to only a few grains visible in each sample (Figure 2.2 right), an observation of the possible areas to take samples were made with polarization paper. With this method the orientation of the grain boundary trace towards deformation direction can be chosen. Suitable areas were chosen with possibly low content of bubbles and impurities.

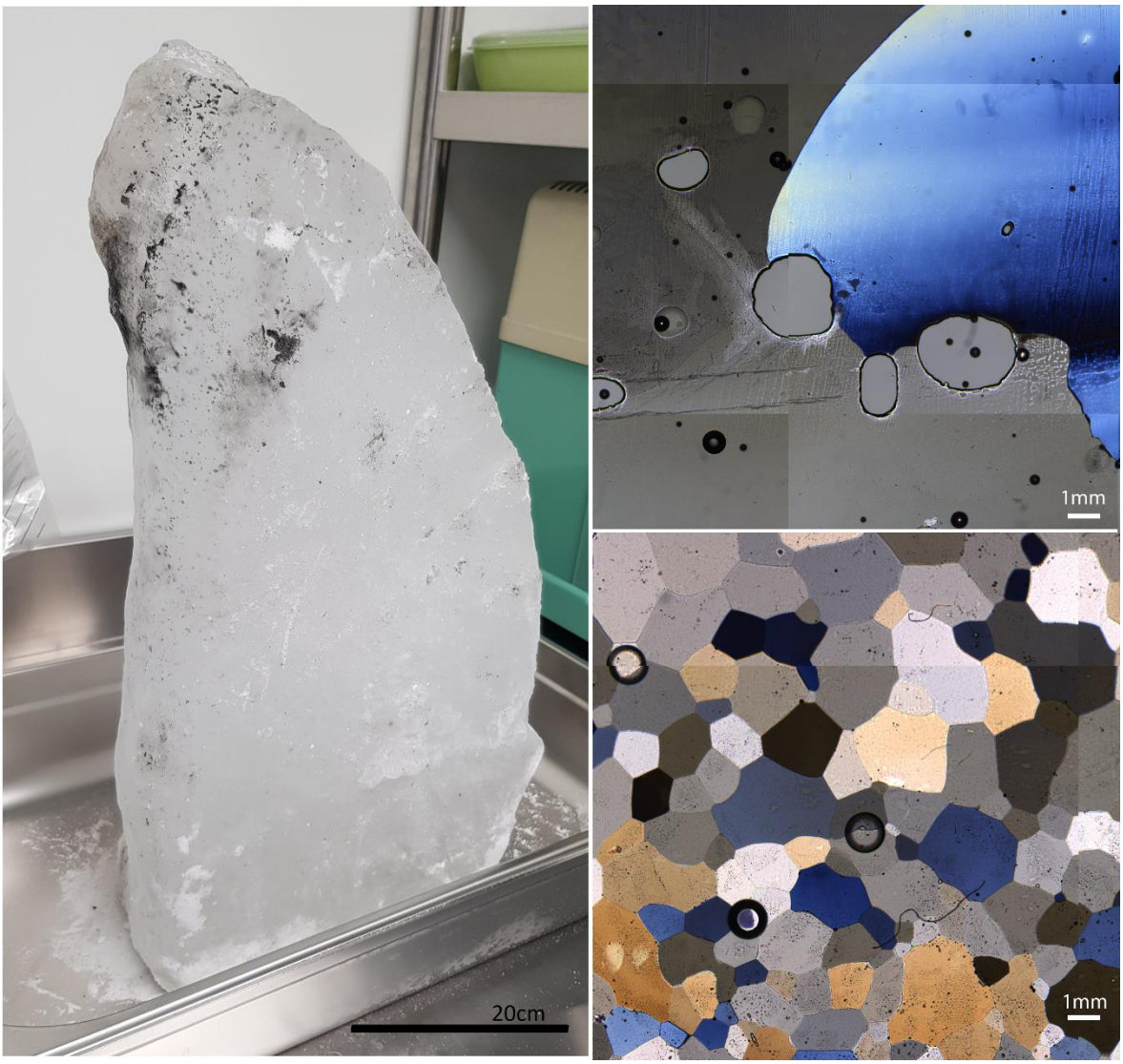

Figure 2.2: Ice sample form Vatnajökull glacier in Iceland. Black areas have a higher particle content. Right: Thin section from natural ice (top) sample with two grains partly seen and bubbles of several millimeters, compared to a thin section of an artificial polycrystalline ice sample (bottom).

2.2 Thin sections

The artificial ice cores (produced as described in section 2.1) are cut along the long axis of the core with a band saw in pieces of 30x40mm with variable height. Most likely between 8-10mm. Samples from the natural ice were cut in the same size. The samples were attached to a glass plate by using distilled water as glue (Figure 2.3 top left). The upper side was then cut with a microtome until a completely even surface was achieved. This is necessary to attach the section surface over the whole area with the glass.

At this point different options of proceeding were tested. The best results in the later deformation were archived by attaching pieces of fiber at the shorter sides of the section (Figure 2.3 top right).

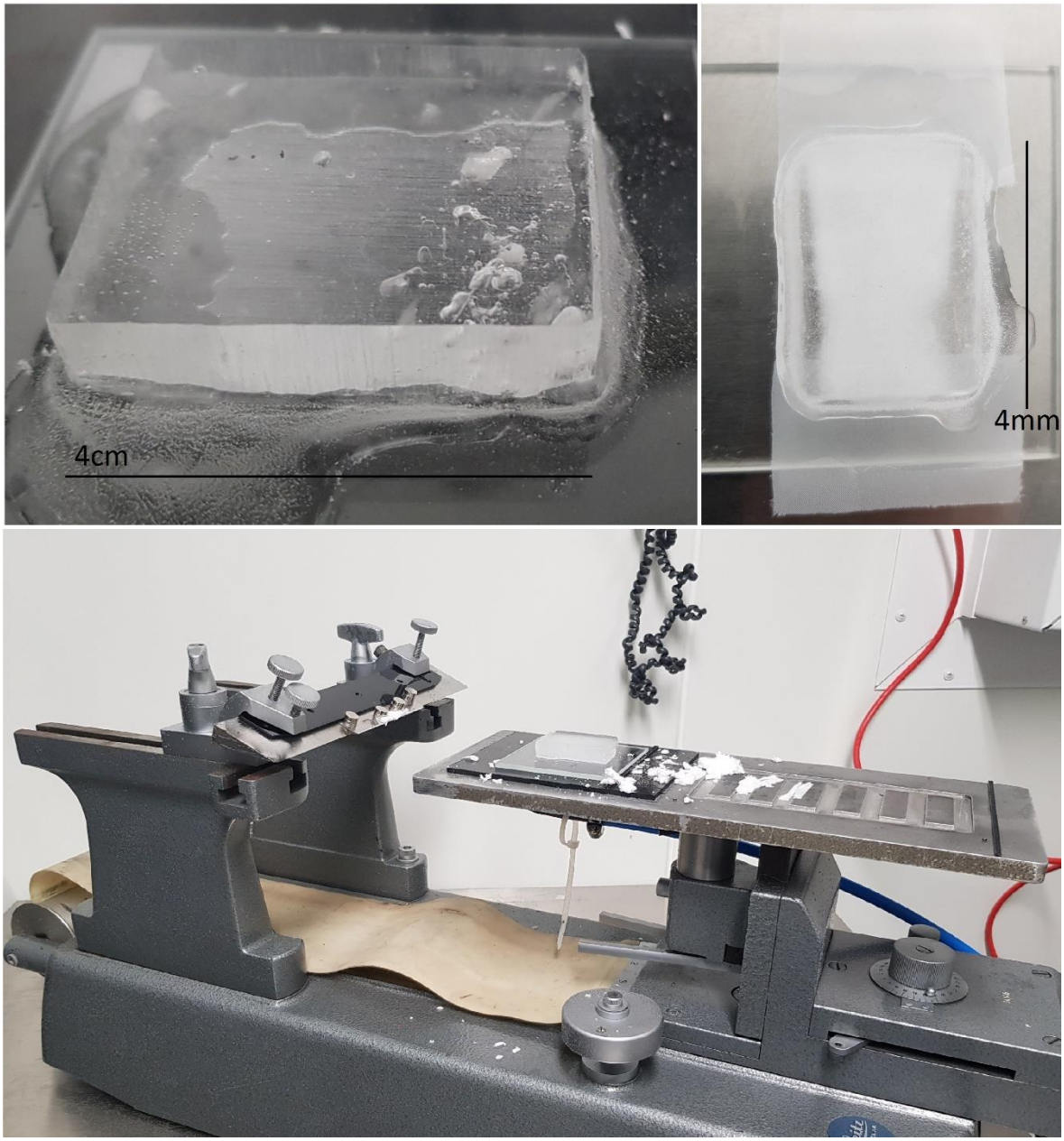

Figure 2.3: Top: Ice samples glued to glass with distilled water (left) as preparation to even one side of the sample. Sample with attached fiber (right). Bottom: Microtome to cut thin sections with sample.

Therefore, two pieces of fiber were cut diagonal to the mesh direction with a size of 4x3 cm soaked in distilled water and frozen in position between 2 glass plates while pressure

from above was applied. This results in the two pieces of fiber being frozen flat on the glass. By slightly warming one of the two glass plates they could be disattached with the fiber still sticking to one of the glasses. Excess water around the fiber was cut away with a handheld microtome blade and the glass afterwards cleaned with acetone. This step needs to be prepared before evening out the surface of the sample section. As the fresh cut surface of the ice samples can undergo fast changes due to sublimation depending on the temperature or frosting effects depending on the water saturation in the surrounding air, the time the section is not covered needs to be minimized (Prior *et al.*, 2015).

The prepared ice sample was set in position on top of the fiber pieces and pressure was applied while the bottom glass with the fiber was warmed form underneath to melt the fiber into the sample and at the same time attach the full surface of the sample to the glass area between the fibers. Afterwards the sample was again cut with a microtome until it reached a thickness of about 250µm.

The thin section is then floated onto a layer of silicon oil (AK 50000 of AK 25000) by warming the transferring glass plate from underneath and carefully pushing the sample. The section then was covered with a second layer of silicon oil. A second glass plate was placed on top, so we get a sandwich with glass on the bottom, silicon oil, ice, silicon oil and glass on top.

The microtome used (Figure 2.3 bottom) makes it easy to archive an even surface with an equal thickness for the whole thin section. The sample is placed on a slider and hold in place due to an applied vacuum from underneath. By moving the slider back and forth thin slices are cut every time. The thickness of the slices can be varied. Although the final touches for the thin sections sometimes had to be done with a handheld microtome, as the fiber can be cut easily otherwise.

2.3 Simple shear apparatus

With the simple shear deformation apparatus shown in Figure 2.4 a theoretically maximum shear strain of about 2.8 is achievable. This was calculated with the maximum possible distance the two clamps can move relative to each other. The archived shear strains in this study are way lower for different reasons discussed later.

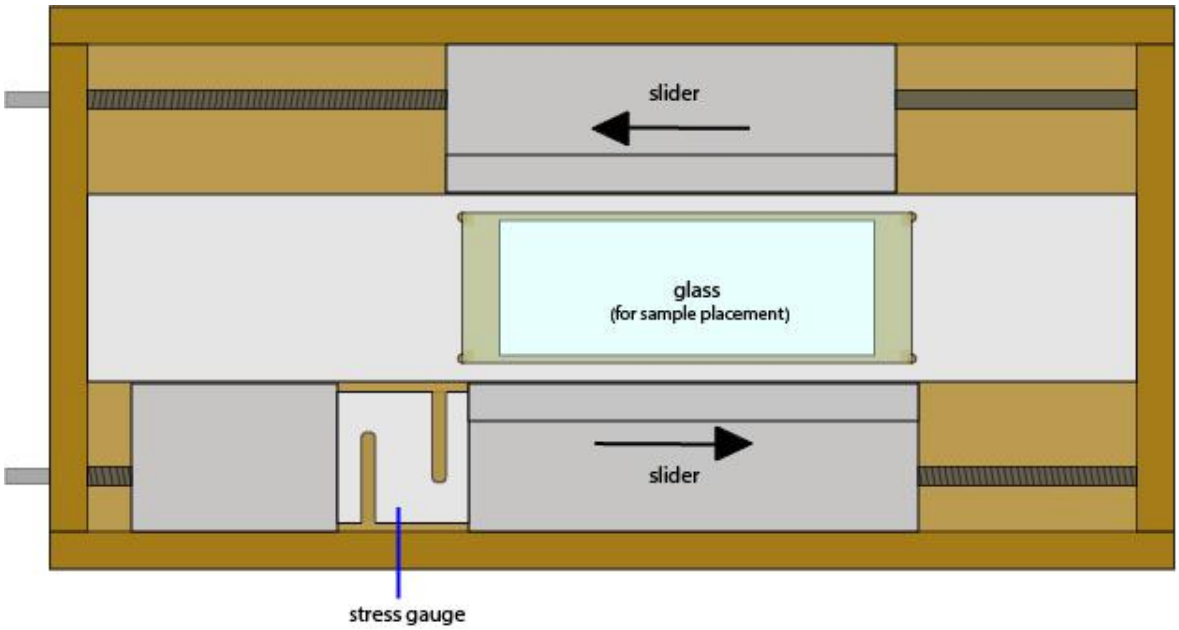

Figure 2.4: Schematic sketch of the deformation apparatus, bird's eye view. Showing the two sliders and with indication of their movement direction, the stress gauge and area for the sample placement. The cuts of the two threaded rods are opposed leading to a movement of the sliders in opposite directions even though the rotation directions of the threaded rods are the same. The relative movement of the sliders leads to a sinistral shear sense.

The shear strain γ is defined by the relative movement of two points on opposite sides of the sheared zone. Therefore, it is calculated as $\gamma = tan(\psi) = \frac{G}{A}$, with G is the opposite and A the adjacent of the opening angle ψ (Figure 2.5) (Wilson & Zhang, 1994; Fossen, 2016).

To create a shear deformation the two slides are attached on a threaded rod with opposing cuts for each side. Leading to a movement in opposite directions of the slides while the threaded rods are rotating in the same direction.

The movement is provided through a connecting part with a motor (Faulhaber spur gearheads series 15/5) which can be controlled and observed for constant speed. Two different motors from of the same model with different reduction ratio were used, 126741:1 for the slowest deformation and 19813:1 for all other deformations.

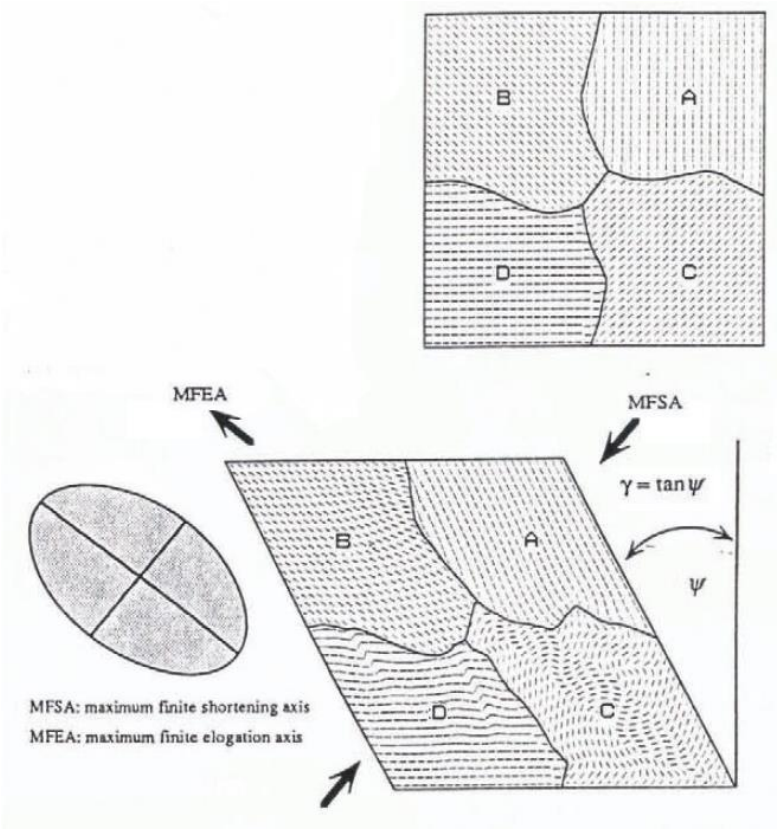

Figure 2.5: Undeformed sample (top) and sheared sample (bottom) with indication of the maximum shortening and maximum elongation axis and the resulting strain ellipse. Shear strain is calculated with $\gamma = tan(\psi)$ (after Wilson & Zhang, 1994)).

Initial tests with fiber attached on both sides of the thin section, clamped to the sliders were done. The flexibility of the fiber lead to a rotation of the section as the fiber waved in the free space between slider and glass (see Figure 2.6). To avoid this effect another test was done with copper blades with a thickness of 0.5mm, so the blades were thicker than the sample. Two blades on opposing sides of the sample were cut with step like pattern with an overall angle of 45° to push the thin section to induce the shear deformation. A second pair of blades was placed on the other side of the sections to prevent rotation of the ice (see Figure 2.7). But the section slipped underneath the blade and did not deform. This could be prevented by pushing the two glass plates together so that there is no space between copper blades and glass, but the silicon oil does make this hard to manage. Another option would be to increase the thickness of the copper blades but would lead to thicker layers of silicon oil needed. This would probably be a problem as the ice has too much room to move up and down in the oil and is most likely to fold within itself or break.

The finally used technique includes the fiber wings and two additional copper blades underneath and above the fiber in the space between clamp and glass to minimize the bending of the fiber but still giving the silicon oil room to move. Two pieces of copper on both ends of the glass keep the top glass in position in respect to height. The deformations still show a small amount of rotation, but most movement is due to shear deformation.

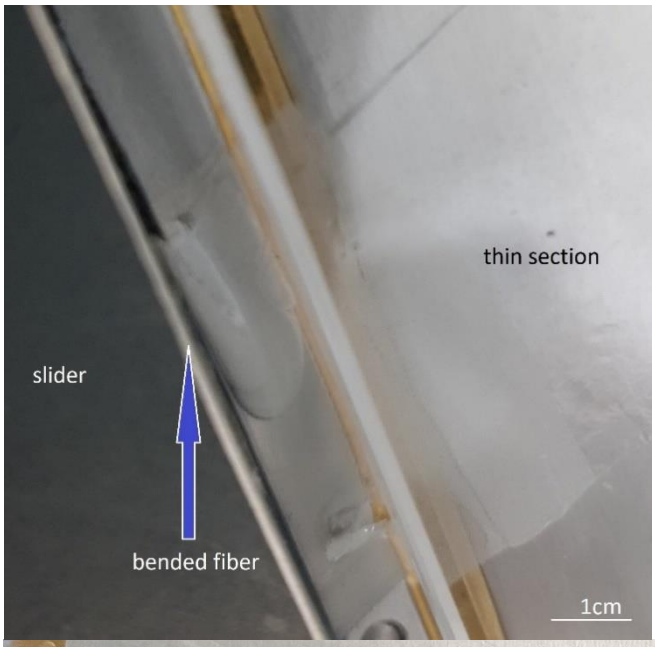

Figure 2.6: Bend fiber in the free space between glass and slider after movement of the sliders.

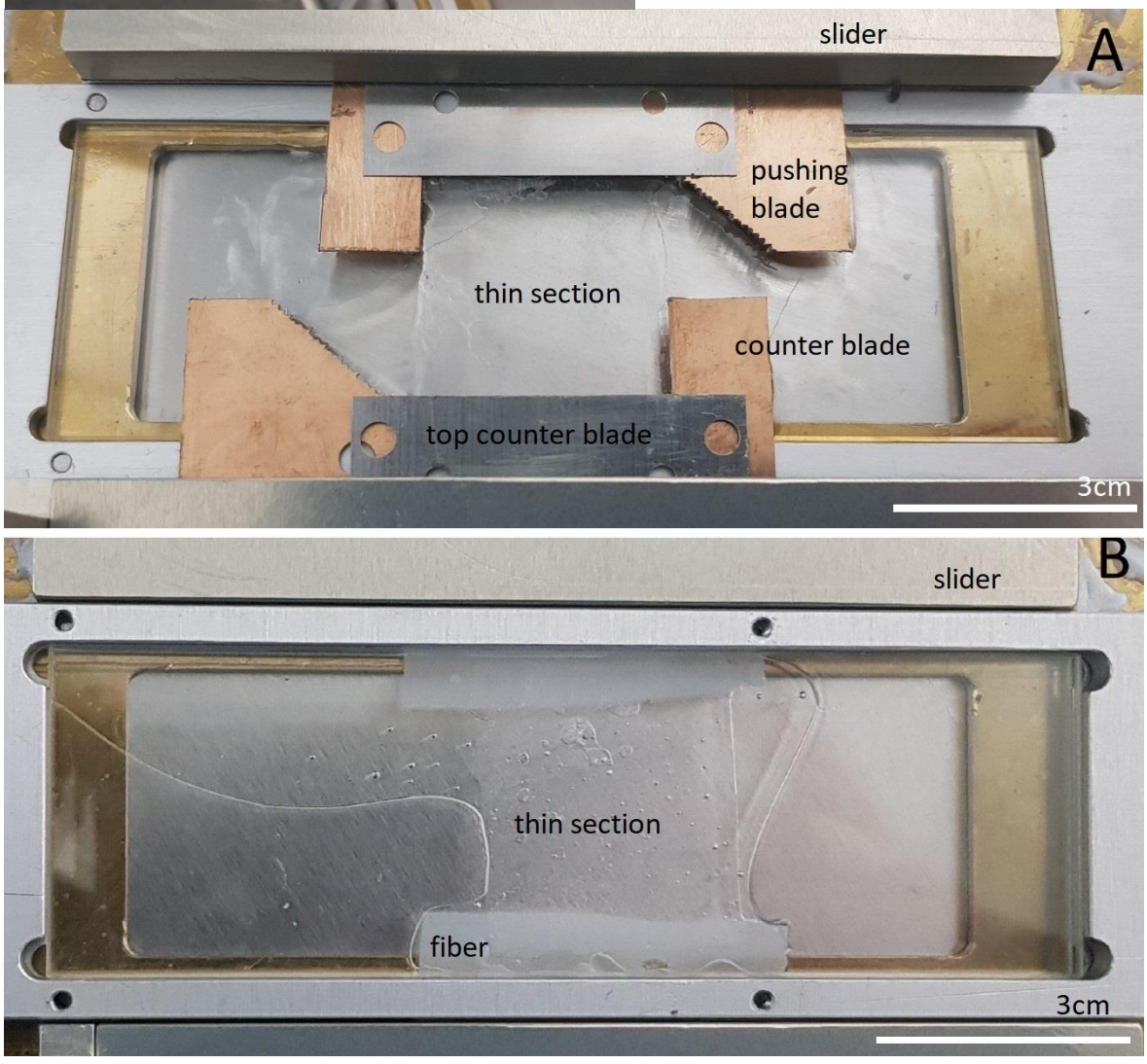

Figure 2.7: (A) Attempt to induce deformation with diagonal cut blades and (B) with attached fabric.

Calibration of deformation speed

To determine the needed rotation rate for the motor for specific shear strain rates several tests have been run to calibrate the system and determine an equation. Therefore, the press was moved with different motors and different rotation rates. The distance after several times was measured. This leads to the following equation to calculate the needed motor speed as rpm (=rounds per minute):

$$rpm = \frac{Motor*42*60*velocity}{2}$$

Hereby 'Motor' is a specific number depending on the translation of the gears from the motor, the number 42 refers to the number of cuts in the gears within the translation component which connects motor and deformation apparatus. The 60 is a determined constant for proportionality, speed equals the velocity for the deformation which is linked to the shear strain rate with $v = \dot{\gamma} * d$ (Staroszczyk, 2019). Hereby v is the velocity, $\dot{\gamma}$ the shear strain rate and d the thickness of the sheared zone. The velocity is taken for both clamps moving away relative to each other as this is equal to only one side moving with double the speed. Everything is divided by two because the rotation is transferred into movement over two threaded rods.

Calibration of stress measurement

A calibration for the stress measurement has not been done yet. But even with calibration measured the correction would still be a relative amount as the distribution of the silicon oil in the deformation apparatus changes the internal stresses that need to be corrected. The exact distribution of the oil can differ for the experiments and can therefore not be imitated perfectly.

Stress gauge

The s-shaped mini stress gouge by interfaceforce (manufacturer) is placed on the bottom slider as can be seen in Figure 2.4. The measured stress is the total amount and must not be multiplied by two for the second slider, as the force measured on the one side represents the whole system. The gauge is connected to an interface outside the cold room and continuously captures data in selectable time intervals.

2.4 Fabric Analyzer G60

To capture the pictures during the deformation a fabric analyzer G60 was used. This is an automated polarizing light microscope and can be used to determine the <c>-axis

orientation for each measured pixel in the observed area with a maximum spatial resolution of 5µm/pixel (Wilson *et al.*, 2007; Peternell *et al.*, 2009; Peternell *et al.*, 2010; Wilson & Peternell, 2011). Therefore, images with light sources from nine different positions are measured and for each position the polarizers are rotated giving stacks of 18 images for each light position. The <c>-axis orientation is derived by overlapping these images. Each stack with 18 pictures from one light position gives a plane containing the <c>-axis, combining these planes the intersection point gives the orientation (Figure 2.8). The quality of these intersections is represented by the geometrical quality (gq) index by a number between 0 (very poor) and 100 (very good). The automatization of the measuring of a specified area in determined time intervals offers the option to observe in situ experiments over a large time in regular time steps.

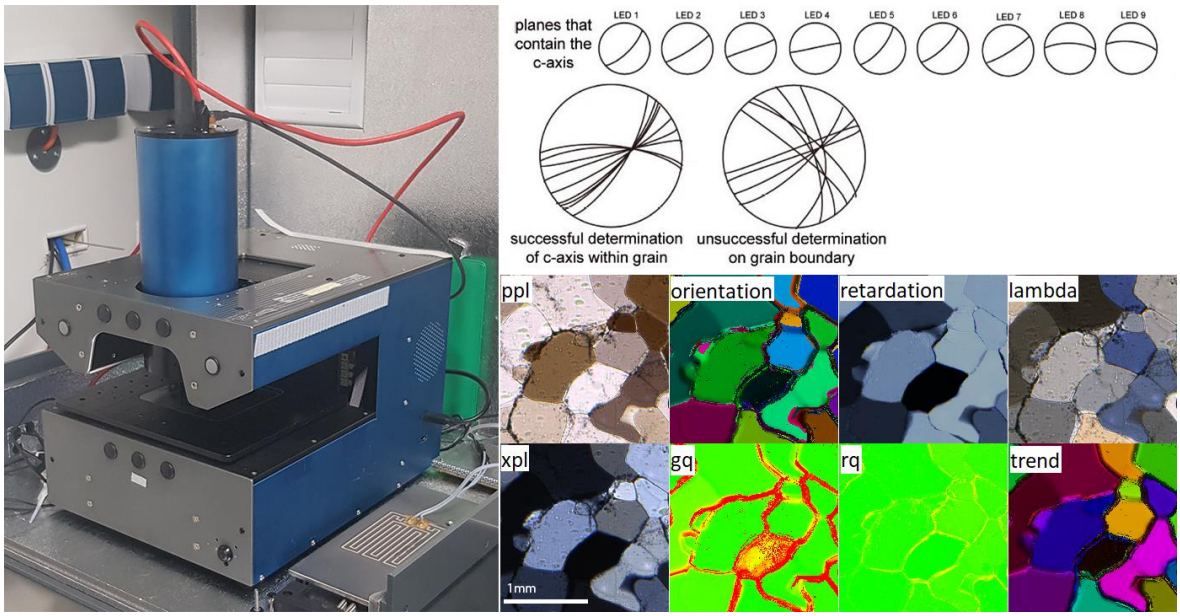

Figure 2.8: Left: Photography of the fabric analyzer G60. Right top: Determination of orientations by overlapping planes from the different light origins. Depending on how good these planes intersect the <c>-axis orientation was successful or not (Wilson et al., 2007)). Right bottom: Types of pictures taken. ppl=plain polarized light, orientation=<c>-axis orientation, retardation=maximum birefringence, lambda=with gypsum plate, xpl=cross polarized light, gq=geometrical quality, rq=retardation quality, trend=<c>-axis orientation trend.

For this thesis eight picture types were saved for each time step during deformation. Plain polarized light (ppl) picture, cross polarized light (xpl) picture, lambda (with gypsum plate), orientation (<c>-axis orientation), trend (<c>-axis trend independent of dip direction) and quality information for geometrical (refers to orientation) and retardation were gathered with a resolution of 10µm per pixel and for one of the experiments with 5µm per pixel (experiment -10_02). The measured area for each timestep for all

experiments varies throughout the experiments from the smallest with 2x2 tiles to the largest with 4x4 tiles. Each tile equals an area of 1000x1000 pixels.

The data is saved in a .cis data format and each pixel contains a specific value for each measured parameter.

2.5 FAME Software

FAME (Fabric Analyser based Microstructure Evaluation) is a MATLAB® software to process fabric analyser data. It allows the calculation of several deformation steps as a whole experiment and therefore calculating time/strain dependent statistical data (Hammes & Peternell, 2016). The software is an evolved version of a set of individual MATLAB® scripts (Peternell *et al.*, 2014).

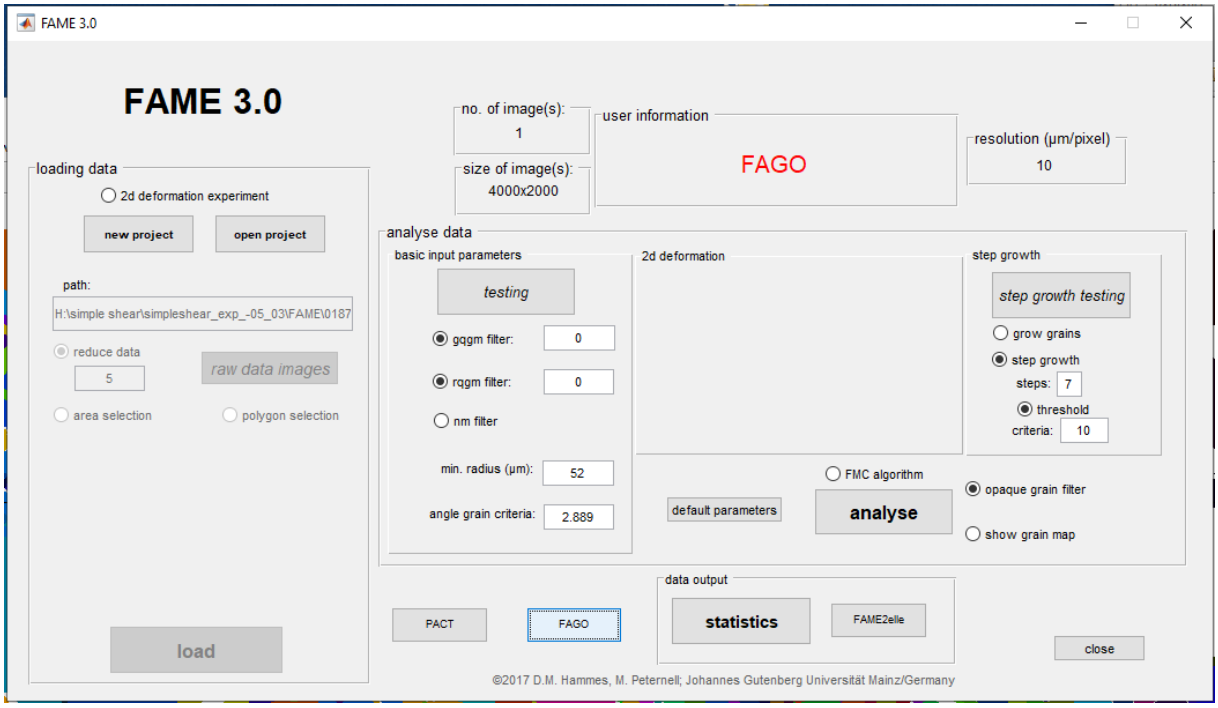

Figure 2.9 Graphical user interface of the FAME software. The interface is partitioned in loading, analyzing and output of the processed data recorded from fabric analyser.

The graphical user interface (GUI) of the software reflects the parting of the software into three main sections, loading, analyzing and data output (Figure 2.9).

The first step is to load the fabric analyser data. Different options are available depending if a single analysis or a whole experiment should be analyzed. The option to reduce the data can help to reduce the calculation time but needs to be used carefully as a too great

reduction might lead to false results and must therefore be tested carefully (Peternell *et al.*, 2014). The area for analysis can be determined by ether selecting a polygon by clicking on an image or loading a .txt file with the coordinates of the edges divided by tab. Giving the opportunity to easily calculate individual statistics for different areas, e.g. higher/lower strained areas.

After converting the pixel related data from the fabric analyzer (.cis) to a MATLAB® compatible format with the before chosen data reduction and selected polygon the testing option provides an environment to Figure out the optimal parameters to create the best fitting grain map for the later analysis. The measured orientation data is the main source to detect individual grains (Figure 2.10). The four parameters which can be varied fulfill specific functions. The two quality parameters gqgm filter (geometric quality) and rqgm filter (retardation quality) can be used to eliminate data points with not trustworthy measurements and therefore reduce fuzzy little dots than could mistakenly be detected as grains even though they are just pixels with lesser image quality. The minimum radius gives a value for how big a detected “grain” needs to be to be taken seriously. Giving a minimum number of pixels to be counted as a grain. This value should always be taken with the resolution in mind, grains with less than 5 pixels should be avoided. The angle grain criterium is the only variable changing during the experiment. It gives a buffer for the misorientation between to pixels so that they are still detected as the same grain.

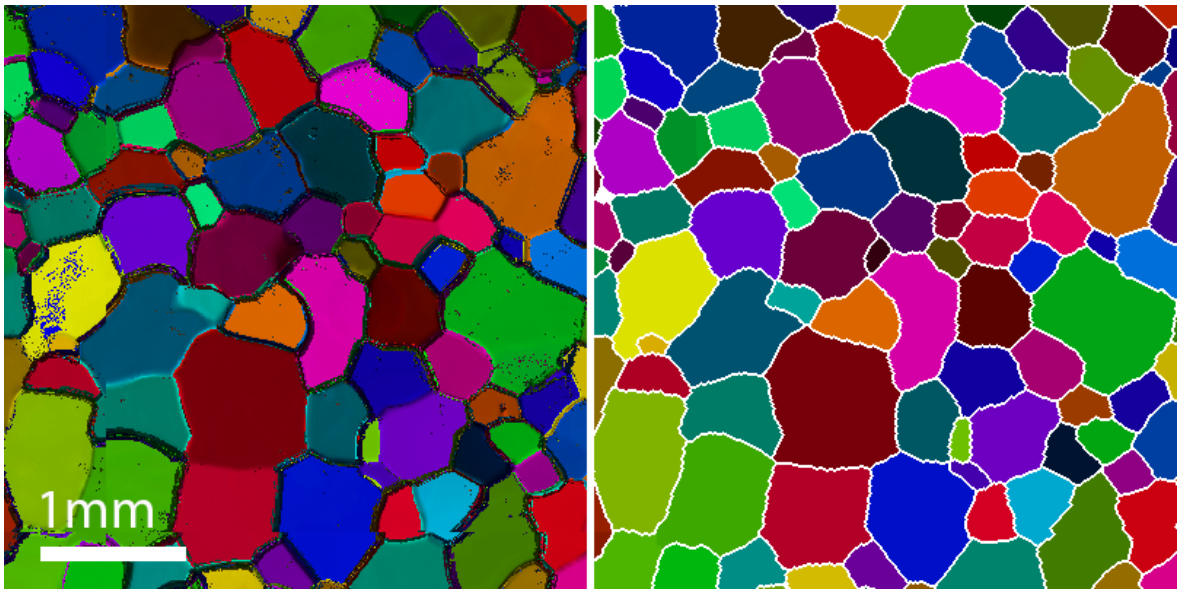

Figure 2.10: Grainmap created by FAME (right) based on the orientation measurements of the <c>-axis (left). Grainmap wit determined with fitted parameters and after step growth function. White lines represent path of grain boundaries.

With these parameters as many as possible grains should be detected at the right position and shape. To fill the empty areas between grains the grain growth function is provided. For each growth step all grains gain a row of pixels to their area along the whole boundary until they reach another grain. This function also provides a testing option (Hammes & Peternell, 2016). Analysis of the data is based on the grainmap.

After analyzing the data, the software provides different statistic calculation options. For this thesis statistics for mean grain size, grain shape, area fraction, <c>-axis orientation, the ternary path, grain size histogram and hard/soft maps were calculated.

The hard/soft criteria used for these maps provides a quantitative value for the orientation describing their likelihood to be easy or hard to deform. It is a value between 0 and 1 depending on the angle to the deformation direction representing the quality of the grain to be in an easy or hard glide position (Wilson & Zhang, 1994). The calculation is based on the Schmid factor. The analysis as well as the statistics can be performed for single deformation steps or automated for the whole deformation experiment.

2.6 FAGO tool

The FAGO (Fabric Analyser Grain boundary recOnstruction; *Hammes & Peternell, 2018*) tool is part of the FAME software and was used to determine the orientation of grain boundaries. The software uses the retardation images taken by the fabric analyser for the determination. A graphical user interface helps to pic the grain boundaries for analysis choosing the desired boundary on the calculated grainmap of the area. Different options are available, a single or a multigrain analysis. For this study only single grain analysis was used and in addition each grain was divided into sections depending on the shared grain boundary to one neighboring grain. An image of the GUI of FAGO is shown in Figure 2.11.

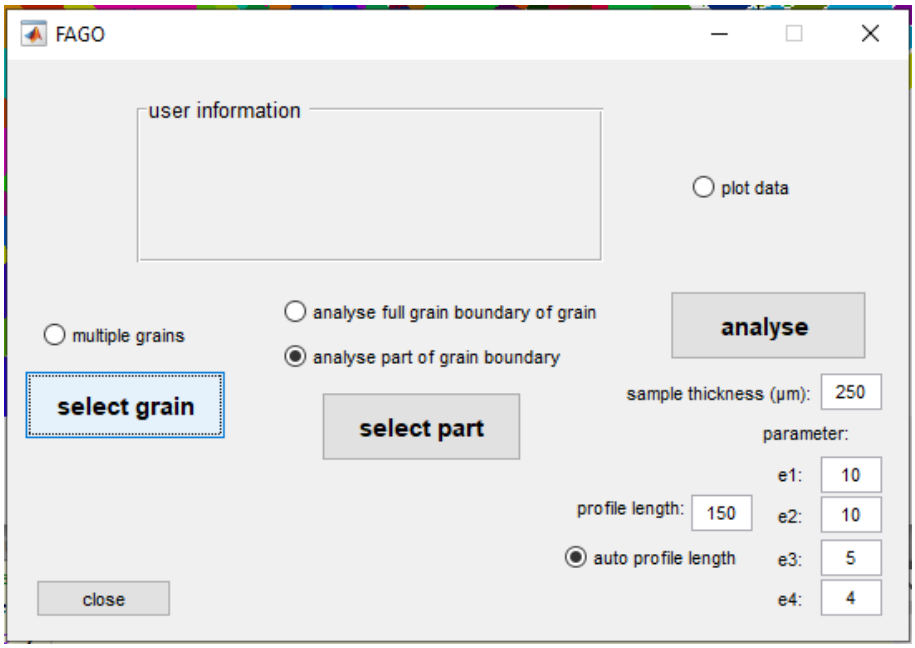

Figure 2.11: Graphic user interface for the in FAME implemented toll FAGO to investigate orientations of grain boundaries from fabric analyser data.

Azimuth

The angle for the azimuth of the grain boundaries is determined from the grain map. Pixels which align to a straight line within a set threshold are joint into a segment. For each segment dip and inclination direction are calculated. The angle of these segmented lines to the north direction gives the angle for the azimuth

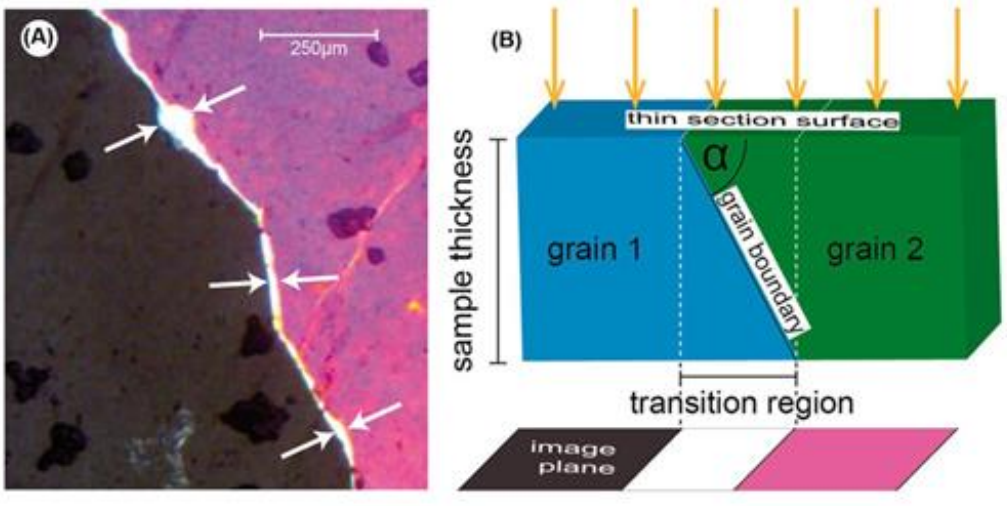

Figure 2.12: (A) Retardation image with transition zone visible in white. (B) Sketch on angular relation between thin section surface and grain boundary determining the size of the transition zone (from Hammes & Peternell, 2018).

Dip angle

To determine the dip angle a profile is calculated from the retardation image for each segment. Along the profile retardation changes from one grain over the transition zone to another grain. This change in color in the retardation image is used to detect the two grains and the size of the transition zone. With the known thickness of the thin section and size of the transition zone the dip angle is calculated (Figure 2.12 B).

The difference between these plateaus can be either big or small, depending on the retardation image color difference. Some empiric parameters e1 to e4 were determined (not by me) to decide which decision path is be taken depending on the plateau difference and color variation within the plateau (Figure 2.13).

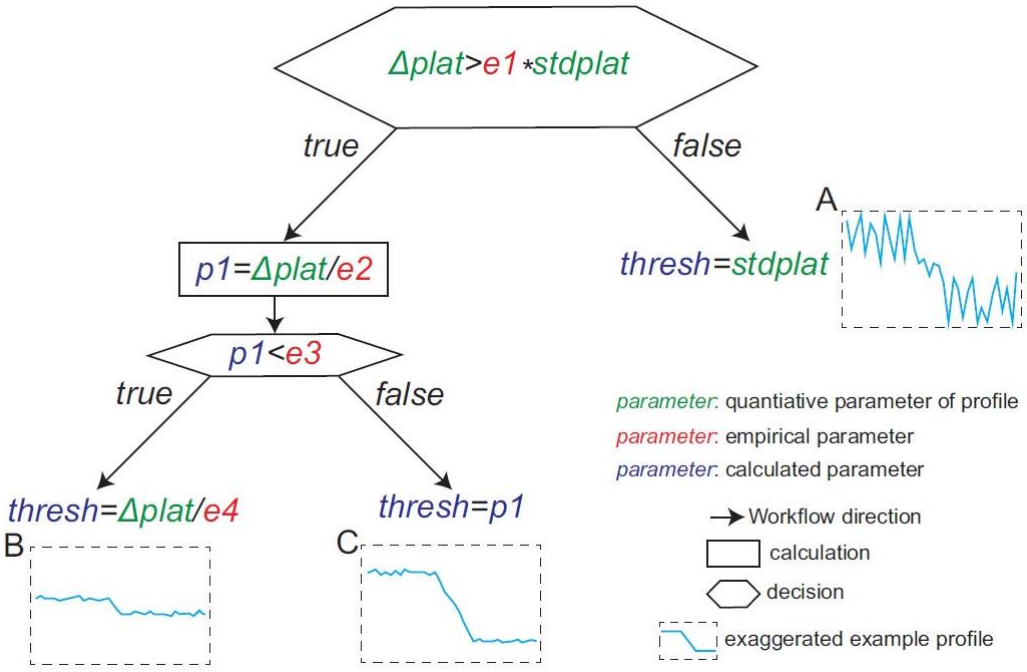

Figure 2.13: Decision path for empirical threshold parameter during grain boundary calculations (from Hammes & Peternell, 2018)).

If the difference of the maximum and minimum measurement of the plateau is smaller than a specified multiplier of the standard deviation the threshold is set equal to the standard derivation. If it is bigger the plateau difference is divided by an empirical parameter e2 and compared to another empirical parameter e3. If the divided difference is smaller than e3 the threshold is set equal to the plateau difference divided by another empirical parameter e4, if it is bigger the threshold is set as plateau difference divided by e2. This covers the tree possible cases shown in Figure 2.13, which are a small difference

in niveau of the two grains (B) a big difference of niveau (C) and a noisy niveau of the grains (Hammes & Peternell, 2018).

Inclination direction

By varying the light origin direction, the size of the transition zone changes. Small angles between light direction and grain boundary lead to smaller transition zones (ΔL') and big angles between light direction and grain boundary lead to bigger transition zones (ΔL), as can be seen in Figure 2.14. Therefore, the inclination direction is towards the light origin producing bigger transition zones.

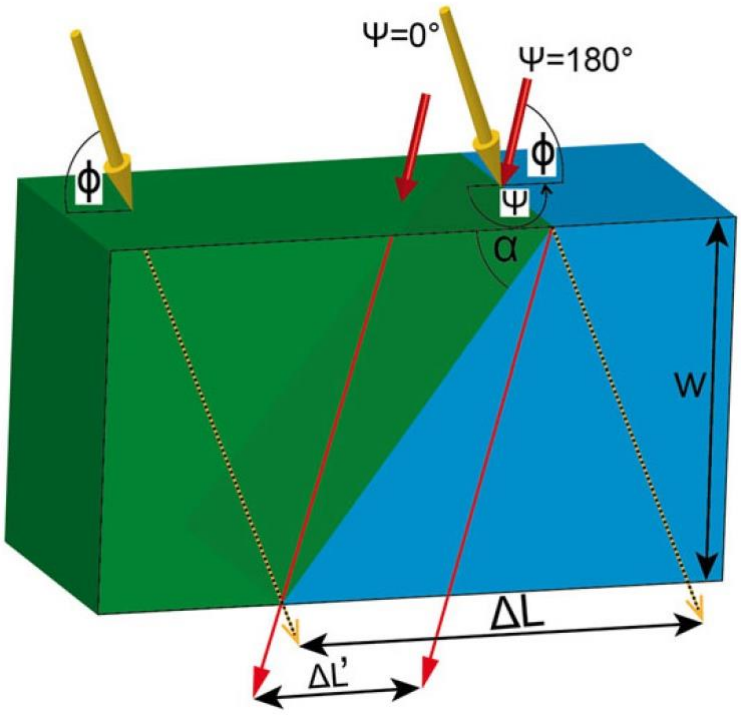

Figure 2.14: Determination of inclination direction by change of origination of light source and resulting difference in size of the transition zone (from Hammes & Peternell, 2018)).

The selected grain boundary section is then parted into segments with a similar azimuth and same inclination direction.

2.7 Investigator software

The investigator software is a tool to read the .cis data files produced by the fabric analyzer and provides an graphical user interface (Figure 2.15) to read the pixel information by clicking on a spot in the picture. The data is shown in a stereonet on the right side and with the slide 'Investigation Data' the information for this pixel is given. This includes the position of the data point, quality values and the orientation with azimuth and latitude. Note that the zero for x- and y- axis is on the bottom left while the zero point for all calculations with Matlab® (including data from FAME) the starting point is on the upper left end. This needs to be considered when using the position information taken from the Investigator software for calculations in Matlab®.

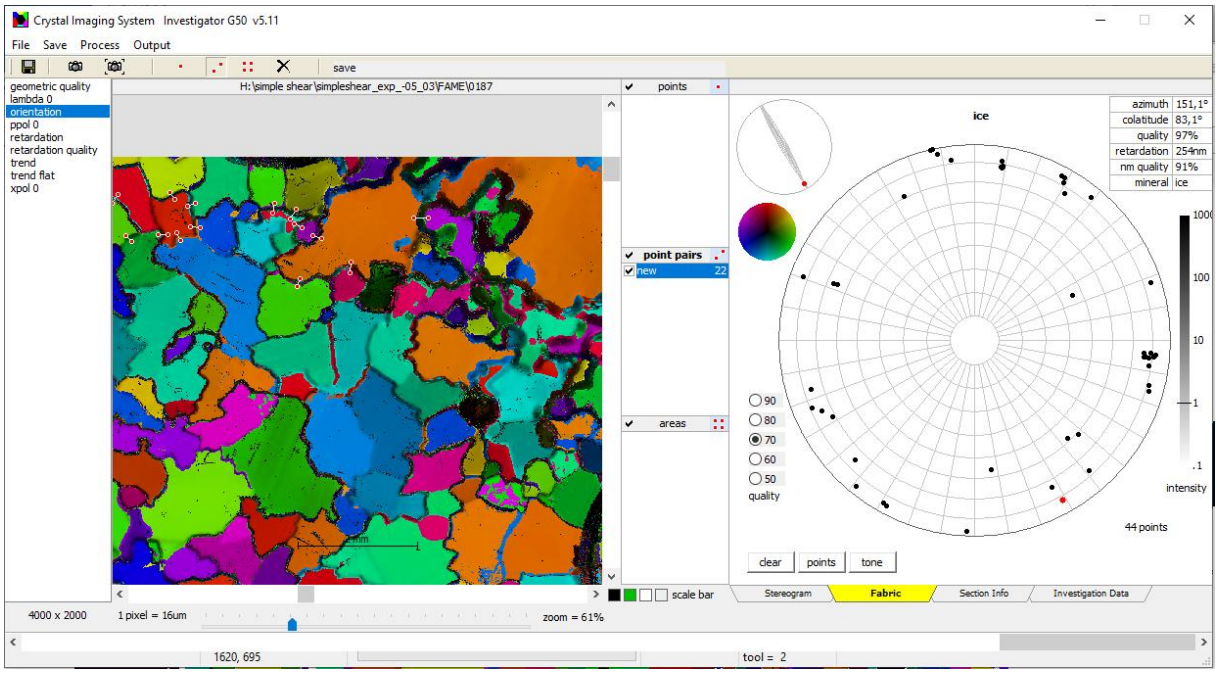

Figure 2.15: GUI of the investigator software with a loaded .cis file set, which contains all taken pictures from the fabric analyser listed on the left. The image and the stereonet with plots of the picked points.

2.8 Further GB analysis

The segments measured with FAGO have been connected to the orientation of the two adjacent grains by using the Investigator software. Therefore the two points, one on the side of the "host" and one on the side of the "neighbor" grain, for each part of the grain boundary were picked and added to the data set from FAGO by using a MATLAB script. Host and neighbor grain in this case is related to the grain picked in FAGO (host) and the grain next to it (neighbor) sharing the same boundary. The orientation was taken from a

central point of the boundary part possibly close to the boundary. With this information connected, a relation between the <c>-axis angle to the grain boundaries was determined. This gives an indication which crystal face is forming the boundary on each side. The distribution of the frequency for the occurring angles between the <c>-axis and the grain boundary pole was then normalized to the total number of data points and corrected with the normal distribution (histogram plots, Figure 2.16). This is necessary as the natural occurrence of, for example a prism plane is higher than for a basal plane. Therefore the frequency of the crystal faces for the normal distribution is described with 1.1111*sin(α), while α is the angle between the <c>-axis and the pole of the grain boundary, and the factor 1.1111 was empirically determined for quartz (Kruhl & Peternell, 2002) and assumed to be similar for ice. This correction was done for the histogram plots as well as for the triangle plots (Figure 2.17) The triangle plots show a density distribution of the angular relations for both sides of the grain boundary combined.

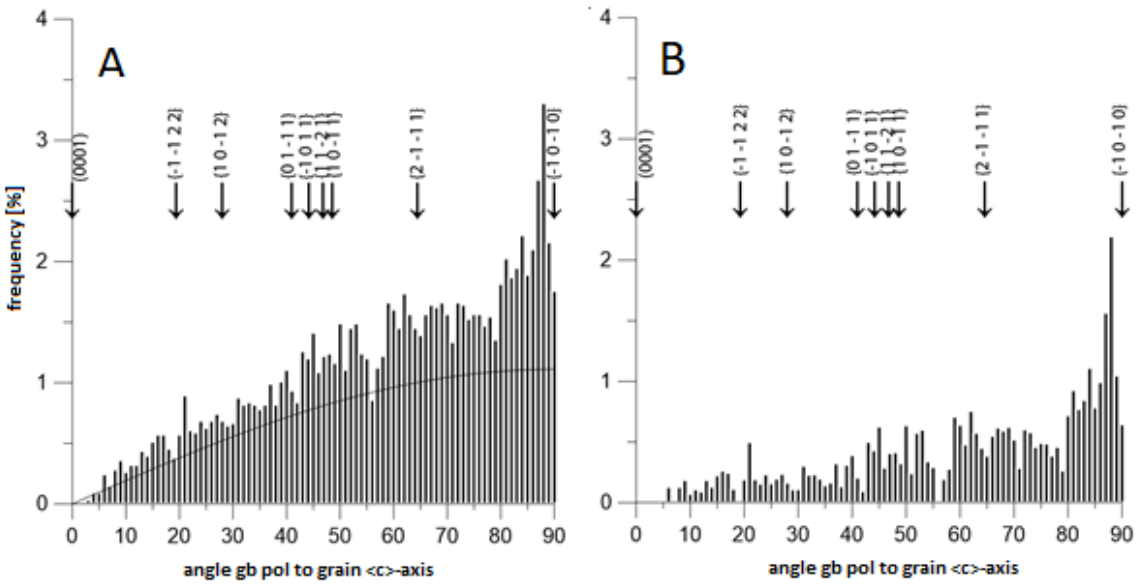

*Figure 2.16: (A) Distribution of occurring angles between grain <c>-axis and grain boundary pole as percentage of the total data points per experiment with bins of 1°. Black line represents the uniform distribution of abundances of different angles for a quartz crystal defined by 1.111*sin(angle grain boundary pole to <c>-axis) while the sinus needed to transfere from a 3D to a 2D uniform distribution. The factor 1.111 is a best fit variable determined for quarz Kruhl & Peternell, 2002), the value is expected to be similar for ice. (B) Distribution after sustraction of the uniform distribution.*

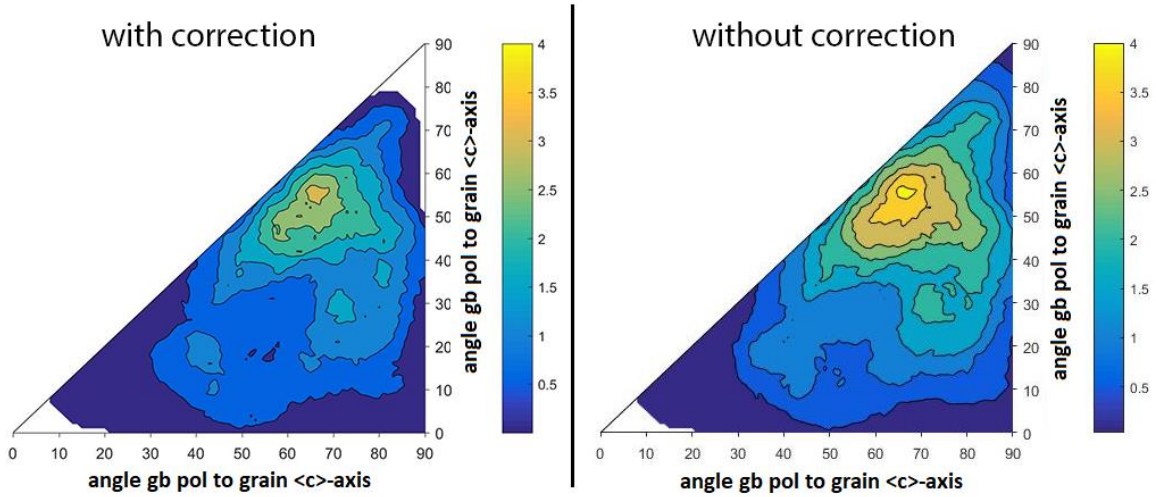

Figure 2.17: Triangle density plot indicating the angular relation between <c>-axes of both neighboring grains towards the pole of the grain boundary between these two grains. Without subtraction of the uniform distribution (right) and with subtraction of the uniform distribution (left).

Fitting plot with the histfit function of MATLAB® with a kernel distribution method were made for the histogram plots and maxima determined.

With the use of MATLAB® more angular relations were calculated such as the angle of the bisector of the two <c>-axis to the main stress direction. All given azimuth orientation is in respect to 'north' being on the top and latitude is oriented from observed layer dipping down.

As the c/a-ratio for ice differs from quartz the angles for the crystal faces pole to the <c>-axis differ from the ones used by Kruhl & Peternell (2002) for quartz. To calculate the equivalent angles for ice the Miller indices for every crystal face, which refer to a hexagonal coordinate system, were transformed to a cartesian coordinate system and angles were determined with vector calculations.

3. Results

Experiments have been performed with two different temperatures (-5 and -10°C), three different strain rates ($2.5x10^{-7}$, $1.25x10^{-6}$, $2.5x10^{-6}$ 1/s) with polycrystalline artificial and single boundary containing natural ice samples. All section had a thickness of 250µm ±20µm. Measurements were done every 30 min with a resolution of 10 µm/pixel, except for -10_02 every 60 min with a resolution of 5 µm/pixel.

A statistical analysis of the orientation relations for <c>-axis, grain boundaries and stress field were made before and after deformation as well as after annealing (if available).

The following chapter will give an overview on the results of these experiments.

The temperature throughout all deformation experiments has been stable (the graphs showing the temperature evolution are attached in the appendix). Graphs showing the observed and analyzed area fraction show a relative constant analyzed area (graphs in the appendix), note that the fraction is calculated for the whole captured image while the analyzed area is way smaller in some experiments. This leads to a small number in area fraction but stays stable throughout the experiment. This shows that the analysis is performed on the same total area throughout all timesteps of the deformation.

Table 3-1: Boundary conditions and parameters for analysis for all analyzed shear deformation experiments. Colors indicate the three strains rates relative slow (1.25x10^{-7} 1/s) green, intermediate (1.25x10^{-6} 1/s) dark blue and relative fast (2.5x10^{-6} 1/s) light blue.

sample name	-10_02	IL_-10_02	IL_-5_01	IL_-10_01	IL_-5_03	-10_08	-5_03	-10_06
strain	0.39	0.76	0.72	0.56	0.38	0.45	0.36	0.62
Strainrate [1/s]	1.25x10^{-7}	1.25x10^{-6}	1.25x10^{-6}	2.5x10^{-6}	2.5x10^{-6}	2.5x10^{-6}	2.5x10^{-6}	2.5x10^{-6}
temperature	-10°C	-10°C	-5°C	-10°C	-5°C	-10°C	-5°C	-10°C
deformation	311 h	69.5h	115 h	71 h	43.5 h	19.5 h	93 h	42 h
annealing	no	13.5h	69h	71.5h	25.5h	no	69h	no
type of ice	poly	natural	natural	natural	natural	poly	poly	poly
measuring frequency	60 min	30 min	30 min	30 min	30 min	30 min	30 min	30 min
parameters FAME								
gq	0	5	45	10	0	0	0	0
rg	0	5	45	10	0	0	0	1
rad min	61.34	115	150	100	80	77	52	38.5
angle start	2.27	3.85	3.53	5.4	2.467	2.33	2.81	2.01
angle end of deformation	2.02	2.66	2.7	2.04	2.6667	3.35	2.889	2.9
angle end of annealing	-	2.26	2.1	2.15	2	-	2.889	-
stepgrowth	13	10	12	15	10	12	7	20
threshold	10	8	8	8	8	10	10	10
				dirty		relative slow	interm ediate	relative fast

Table 3-1 provides an overview on all evaluated experiments with the reached shear strains, strain rates, temperatures, annealing time (if measured), type of ice (natural: icelandic; artificial: polycrystalline), number of grain boundary segments measured and the parameters used for analysis in FAME. Note the natural samples are indicated in their names with “IL”, which relates to their origin Iceland.

Samples have been deformed until the ice section started to rip apart in itself or the fiber was pulled out of the section, leading to different final shear strains between 0.38 and 0.76. All polycrystalline samples were cut from the prepared ice cores along the long axis and from the center of the ice cores. The pressure applied during preparation of the ice

cores therefore is for all sample oriented the same towards the later direction of deformation. The natural samples are considered clean even though they may contain minor impurities in some areas. Air bubbles in the samples were not fully avoidable, although areas with possibly low bubble content were chosen. Sample -10_2 has been deformed using a higher viscous silicon oil compared to the other deformation experiments. As this experiment had a much slower strain rate the higher viscosity is expected to not influence the comparability. Two gears in the connecting part between motor and deformation apparatus had to be exchanged once in-between experiments. The number of cuts in these gears changed from 42 to 43, the resulting change in the transferred motor speed is smaller than the error of the control panels adjustment.

Table 3-2: Overview on differences during deformation for all experiments in respect to occurrence of rotation, added blades, used silicon oil, reason to stop deformation and brief description of features in the samples.

Sample	Rotation	Blades	Silicon oil	Reason to stop	Comment
-10_02	X	-	AK 50 000	-	○ Fiber not under tension from start → starting point set after visible signs of deformation (kinks) ○ Image loss/ interruption of deformation → due to broken electrical socket ○ Polycrystalline pattern with straight boundaries and 120° triple points ○ Curved and irregular grain boundaries, kink bands and uneven shaped grains after deformation ○ Sample thickness increases towards top and bottom → increases error for grain boundary determination
IL_-10_02	X	X	AK 20 000	Several holes along grain boundary	○ Single triple point ○ Shift of camera position to keep track of the observed grain boundaries ○ Short annealing time (13.5h) ○ New grains along former grain boundaries and holes ○ Slight bending of kinks at top and bottom in the right grain

Sample	Rotation	Blades	Silicon oil	Reason to stop	Comment
IL_-5_01	-	X	AK 20 000	Crack from right to left side - of the - section	○ Single elliptical grain (5x9mm) in matrix ○ Camera shift to keep track of grain ○ Massively lobated grain boundary after deformation ○ Kink bands ○ Subgrain boundaries ○ After annealing divided into several grains, matrix as well as former grain
IL_-10_01	-	X	AK 20 000	Ripping on both upper edges of the sample	○ Shallow dipping grain boundaries ○ Subgrain formation to new grains → small new grains along former grain boundary and subgrains ○ Initial shear fractures (not opened) ○ After annealing almost all subgrains are gone and new grains formed
IL_-5_03	-	X	AK 20 000	Cracks open too wide	○ Three air bubbles (enter size) → shape also deforms ○ Crack does not start at bubbles ○ All grains have similar c-axis orientation ○ Two sets of kink bands (perpendicular to each other) → cracks open along grain boundary after development
-10_08	-	X	AK 20 000	Ripping in central area after shear fracture	○ Polycrystalline with bigger grains in central area ○ Grain boundaries mostly straight, 120° triple points not achieved for all ○ shear fracture and initial state of second fracture ○ Irregular grain boundaries and kinkbands after deformation

Sample	Rotation	Blades	Silicon oil	Reason to stop	Comment
-5_03	x	X	AK 20 000	Ripped appart	○ Bubbles ○ Bigger grains at the beginning on the left side (relicts from annealing) → move out of site during deformation (at 0.11 strain) ○ After deformation: irregular and uneven shaped grain boundaries, kinks (especially bottom right corner), irregular shaped grains ○ After annealing kinks on bottom right still more dominant than in other regions ○ After annealing: straightening of grain boundaries, regain 120° triple points → but not really hexagonal grains (middle left some tendencies to)
-10_06	-	X	AK 20 000	Ripped at upper left edge	○ Slightly thicker than other samples (still close to 250µm) ○ "dirty" → small particles and very small air bubbles, preferably along grain boundaries. Some outline older grain boundaries from before annealing during preparation ○ Grain boundary analysis in red area ○ Left and right end bigger grains, center smaller → relict from annealing ○ Somme seemingly grain boundaries are alignment of particles and bubbles along former boundaries

Images in the following section show the analyzed area of the thin sections before and after deformation as well as after annealing. Table 3-2 lists all main general observations, information on the used silicon oil, added blades, occurrence of rotation and the reason the deformation was stopped. For experiments that show rotation of the section (-10_02, IL_-10_02, -5_03, see table 3-2), due to ether the fiber pulled out of the slider or the ice, this rotation is subtracted from the angle used for calculation of the shear strain.

Note that the sections were able to move above or underneath the focus plane during the deformation as it was floating in between the two layers of silicon oil. Therefore, the images sometimes get slightly out of focus with time.

Except for the slow deformed sample -10_02 (cold, slow) all experiments were deformed with fiber attached on the top and bottom as described in part 2.3 and with the less viscous silicon oil AK 20 000 (table 3-2). For the slow deformed sample, the higher viscous silicon oil AK 50 000 was used, and no additional blades were added. The missing blades lead to a slight rotation of the section due to bending of the fiber (see section 2.3). The fabric was not under tension from the moment the sliders began to move, therefore the starting point for the deformation was manually chosen with the first initial signs of deformation visible in the section (e.g. kink bands, outside the analyzed area). During the observation, a few images were lost and a short interruption in deformation occurred due to a broken electrical socket. Exact moment and duration of the interruption is unknown, as the broken socket was not detected immediately. Time frame lies in between 122 h and 136 h of deformation time. The equally polycrystalline pattern of grains with mostly straight grain boundaries and an angle of 120° at the triple points in the starting material (Figure 3.1 A) changes to curved and irregular grain boundaries, kinks and unevenly shaped grains (Figure 3.1 B). Towards the top and bottom end of the sample the thickness slightly increases, the analyzed area in the center in not effected from that. Changes in thickness throughout the sample can increase the chance of breaking the sample. In addition, a constant thickness is favorable for grain boundary measurements, as the error for dip angles remains constant in this case.

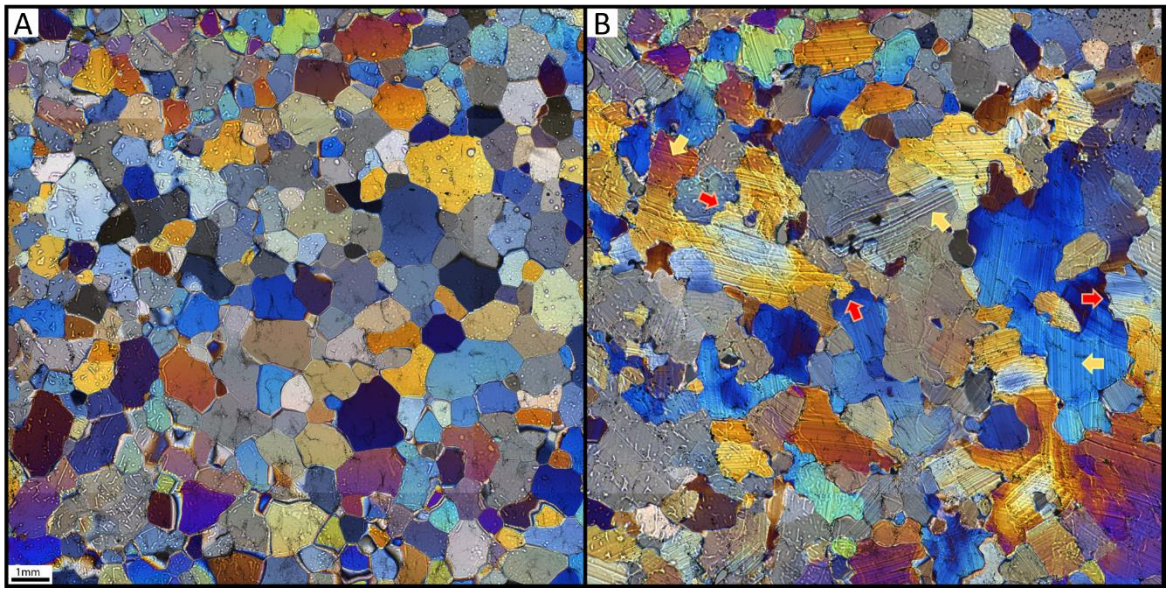

Figure 3.1: Lambda images from experiment -10_02 before (A) and after deformation (B). Yellow arrow: kink bands. Red arrow: lobated grain boundaries. Scale bar equals 1mm.

The thickness of sample -10_08 (cold, fast) lies at the lower end of the thickness range. This leads to a difference in interference colors compared to the other samples. Areas increasing in thickness during deformation (upper left region and inside the shear fracture, Figure 3.2 B) show similar interference colors to the other samples. The polycrystalline pattern in the starting material shows straight grain boundaries, but the 120° triple points are not achieved for all (Figure 3.2 A). A brittle fracture occurred in the central part of the section and another initiation to a fracture is visible in the lower right part. The occurrence of the brittle fracture and the following ripping in the central area mark the end of the deformation. The brittle fracture is immediately filled with small grains. Formerly straight grain boundaries are irregular after the deformation and kink bands are visible in the whole area of the thin section (Figure 3.2 B blue arrows).

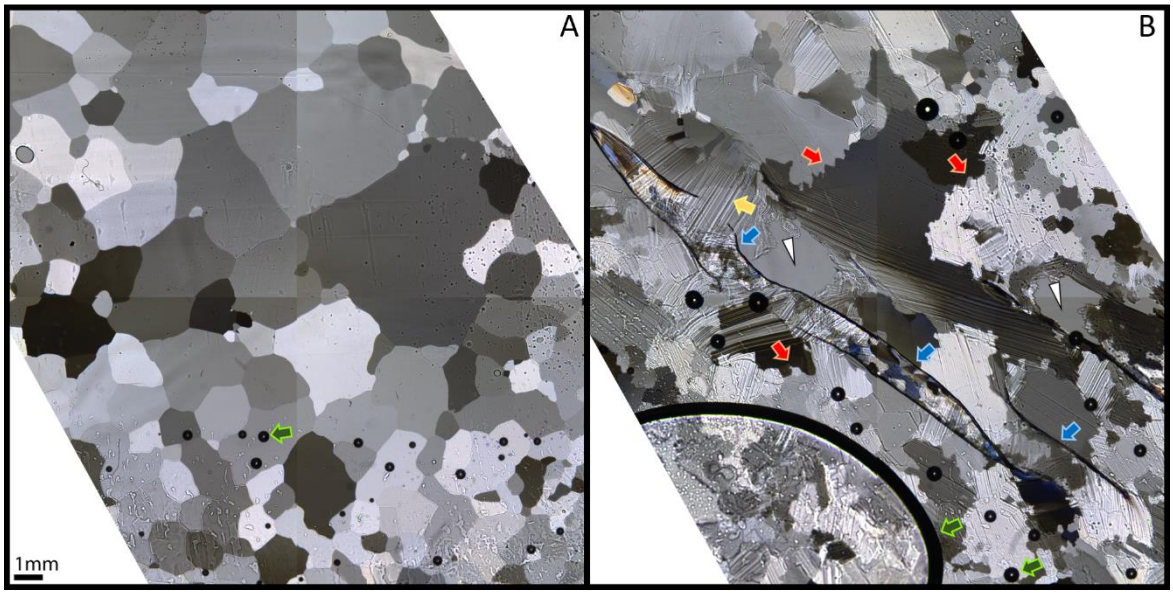

Figure 3.2: Lambda images from experiment -10_08 before (A) and after deformation (B). Dark green arrow: bubbles in silicon oil. Yellow arrow: kink bands. Red arrow: lobated grain boundaries. Dark blue arrow: shear fractures. White triangle: holes in the section. Scale bar equals 1mm.

For sample -5_03 (warm, fast) the upper left region of the thin section was analyzed. The bigger grains on the left (Figure 3.3 A) do not affect the statistics, these are relicts from the annealing during sample preparation. For analysis with FAME only inner grains were picked. Inner grains mean only grains which are completely inside the analyzed area and do not intersect with the outline of the polygon chosen. Also, they move outside the observed are at a strain of 0.11. The kink bands appearing during deformation are especially well developed around the bubble in the bottom right corner (Figure 3.3 B) and stay more visible there after annealing compared to other areas of the sample (Figure 3.3 C). Also, other signs of deformation are visible in Figure 3.3 B such as lobated grain

boundaries and uneven shaped grains. During annealing the grain boundaries straighten again and most of the triple points regain the 120° angle. Still the pattern does not recover fully to a pattern like it was before deformation (Figure 3.3 A).

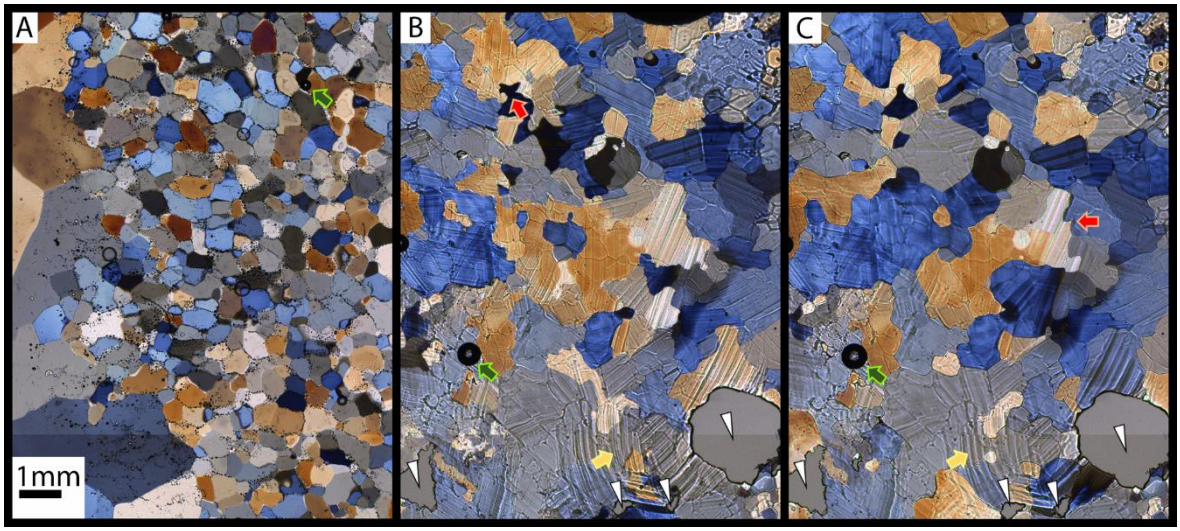

Figure 3.3: Lambda images from experiment -5_03 before (A) and after deformation (B) and after 69h of annealing (C). Dark green arrow: bubbles in silicon oil. Yellow arrow: kink bands. Red arrow: lobated grain boundaries. White triangle: holes in the section. Scale bar equals 1mm.

Sample -10_06 (cold, fast, 'dirty') is described as dirty due to the small number of particles and tiny air bubbles in the sample. The amount is smaller than the particle content in natural glaciers where typical mass fractions of rock particles are between 10^{-6} to 10^{-8} (Cuffey & Paterson, 2010). They mostly align along former grain boundaries in the undeformed sample (Figure 3.4 A pink arrows), and therefore can be misleading. During the annealing process while preparing the artificial ice cores grains grew but particles/bubbles kept their position. FAME analysis was done for the whole area shown in Figure 3.4 A and B. For the grain boundary analysis after the deformation only boundaries inside the red marked area were determined (Figure 3.4 B). This part of the section is the most sheared area.

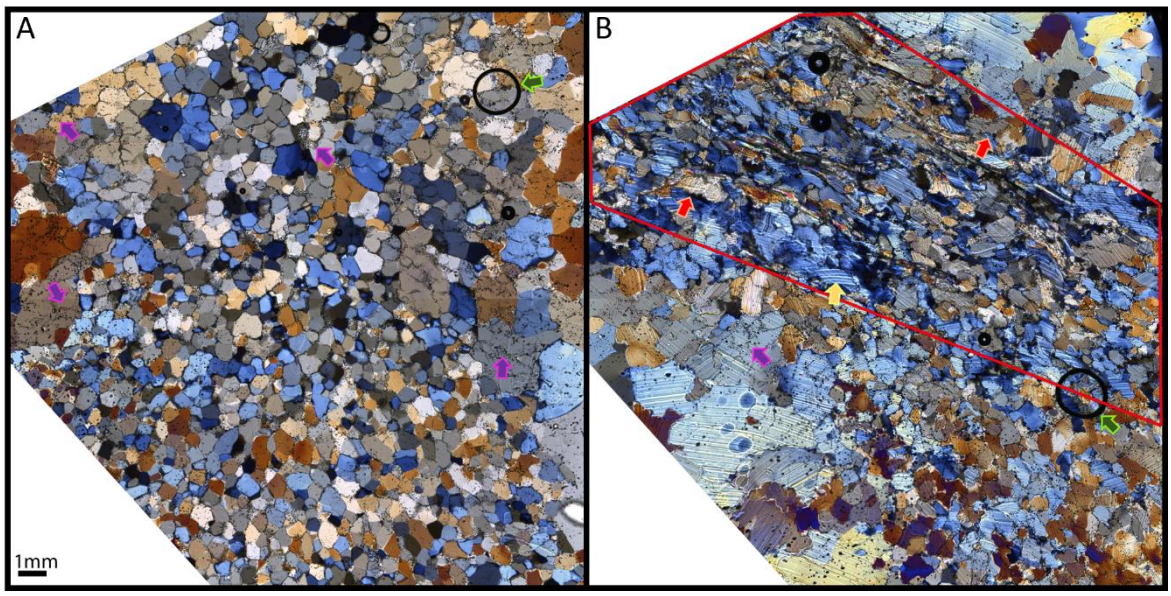

Figure 3.4: Lambda images from experiment -10_06 before (A) and after deformation (B). Dark green arrow: bubbles in silicon oil. Yellow arrow: kink bands. Red arrow: lobated grain boundaries. Pink arrow: particles. White triangle: holes in the section. Scale bar equals 1mm.

Sample IL_-10_01 (cold, fast) shows some shallow dipping grain boundaries at the bottom left side, visible as light gray to white areas in the lambda images (Figure 3.5 A). The single grain from the beginning is divided into several subgrains at the end of the deformation (Figure 3.5 B) and many small new grains have formed along the former boundary and the subgrain boundaries. After annealing almost all subgrain boundaries are gone and new grains have developed (Figure 3.5 C).

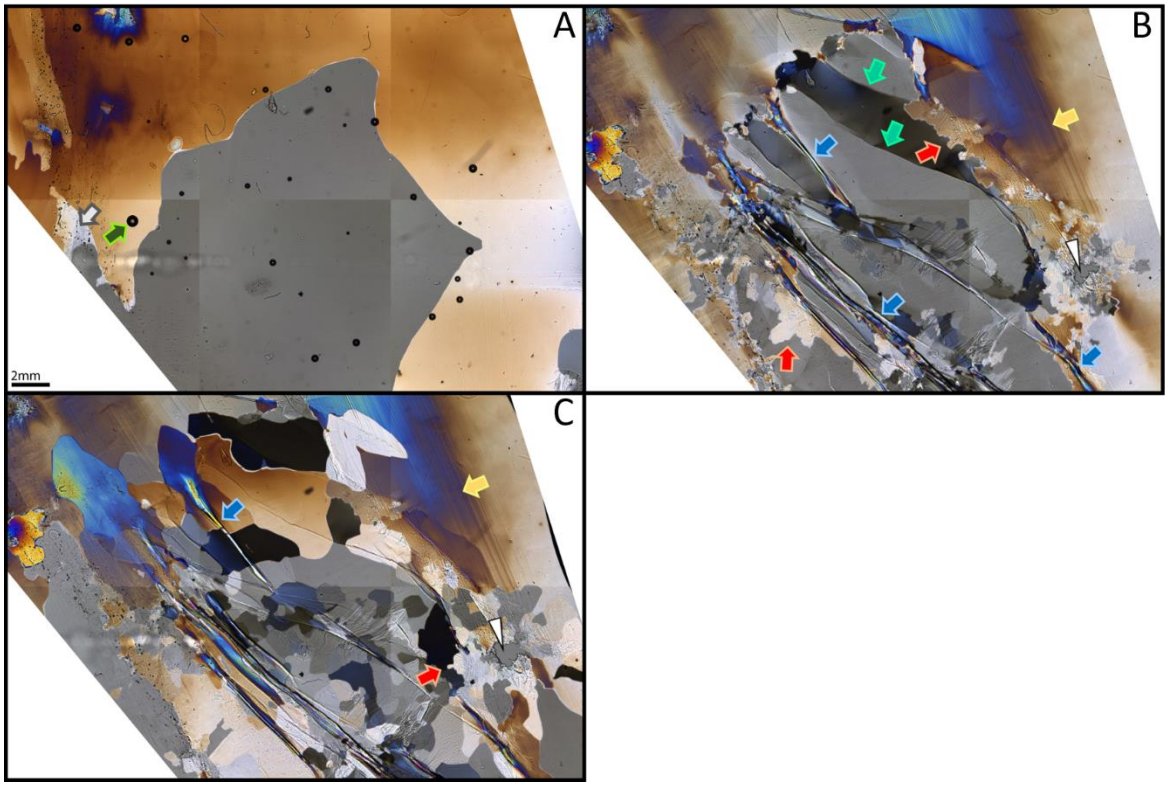

Figure 3.5: Lambda images from experiment IL_-10_01 before (A) and after deformation (B) and after 71.5h of annealing (C). Dark green arrow: bubbles in silicon oil. Yellow arrow: kink bands. Red arrow: lobated grain boundaries. Pink arrow: particles. Dark blue arrow: shear fractures. Turquoise arrow: subgrain boundary. White arrow: shallow dipping grain boundary. White triangle: holes in the section. Scale bar equals 2mm.

Sample IL_-10_02 (cold, intermediate) contains three grains with a triple point at the central bottom part (Figure 3.6 A). During deformation, the observed boundary was about to move out of the scanned area. Therefore, the observed area was adjusted and increased at a strain of 0.49 and a larger area was measured for each following time step. New grains developed during deformation all along the original grain boundaries and around the holes (Figure 3.6 B, red circles). The annealing time of 13.5 h is the shortest within the natural samples. Therefore, grains had less time to grow during that time compared to the other samples.

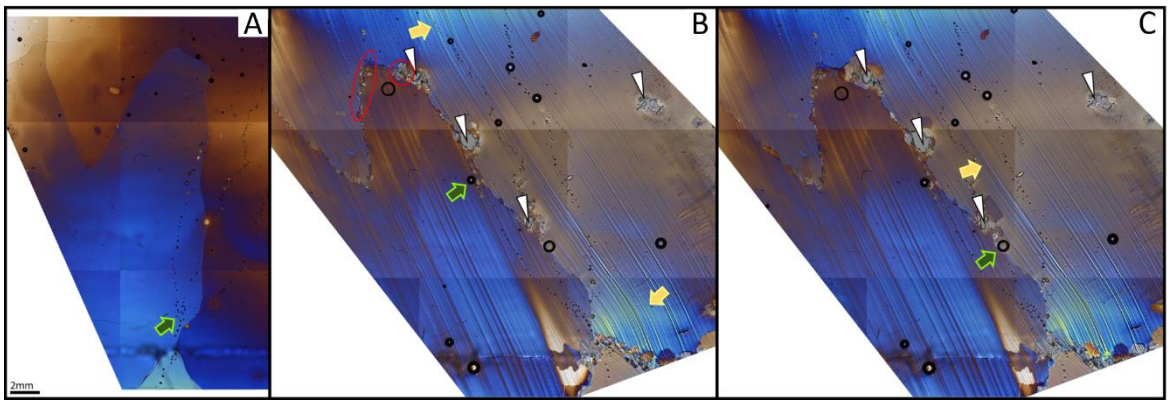

Figure 3.6: Lambda images from experiment IL_-10_02 before (A) and after deformation (B) and after 13.5h of annealing (C). Dark green arrow: bubbles in silicon oil. Yellow arrow: kink bands. White triangle: holes in the section. Red circles: new grains on old boundary. Scale bar equals 2mm.

Sample IL_-5_03 (warm, fast) features three grains, none of them are completely captured in the section. Along the grain boundaries are three air bubbles in different sizes from 1-4mm (Figure 3.7 A). Throughout deformation two sets of kinkbands form (Figure 3.7 B, also in). The first set is equal to the ones in other samples and are due to the glide on the basal plane which is restricted by glass/silicon oil on two sides (see Wilson *et al.*, 1986; Peternell *et al.*, 2019) supplementary). The second set can be seen on the lower right side of the section (Figure 3.7 C, yellow arrow) with a trace approximately perpendicular to the first set of kink bands. The fractures opened after the development of the second set of kink bands along the former grain boundaries. The shape of the bubbles is deformed too. The crack on the lower right part after deformation (Figure 3.7 C) reaches the bubble throughout deformation but does not start there. All three grains have a similar <c>-axis orientation in the beginning.

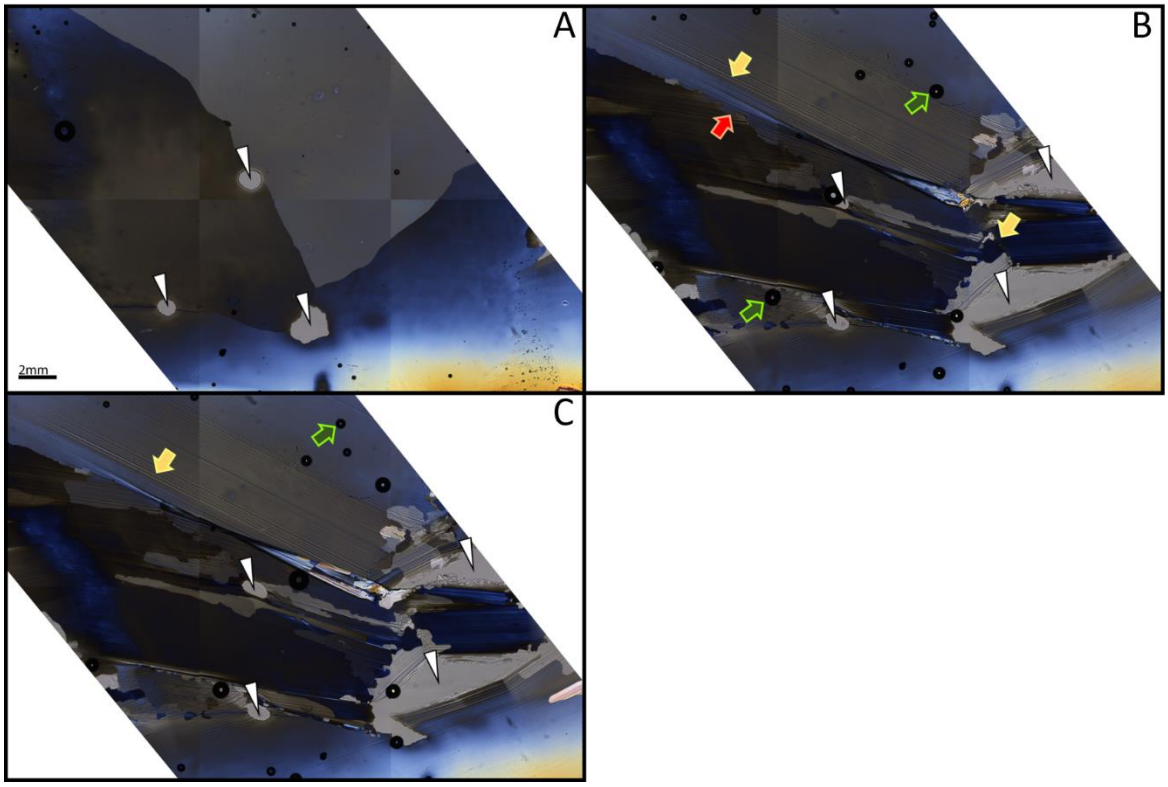

Figure 3.7: Lambda images from experiment IL_-5_03 before (A) and after deformation (B) and after 25.5h of annealing (C). Dark green arrow: bubbles in silicon oil. Yellow arrow: kink bands. Red arrow: lobated grain boundaries. White triangle: holes in the section. Scale bar equals 2mm.

Sample IL_-5_01 (warm, intermediate) consists of a single smaller grain embedded in a matrix consisting of one large grain (Figure 3.8 A). The actual size of the surrounding grain is bigger than the thin section size, the smaller grain has an elliptical shape and a size of about 5x9mm. The position of the camera had to be shifted throughout the deformation to keep the small grain in the center of attention at a strain of 0.26. The boundaries change to an irregular shape during deformation (fig 3.8 B) and straightened again during annealing (fig 3.8 C). Kink bands are visible after deformation and stay visible during the 69 hours of annealing. The original small grain is still detectable after deformation, after annealing the small grain and the matrix split in several individual grains.

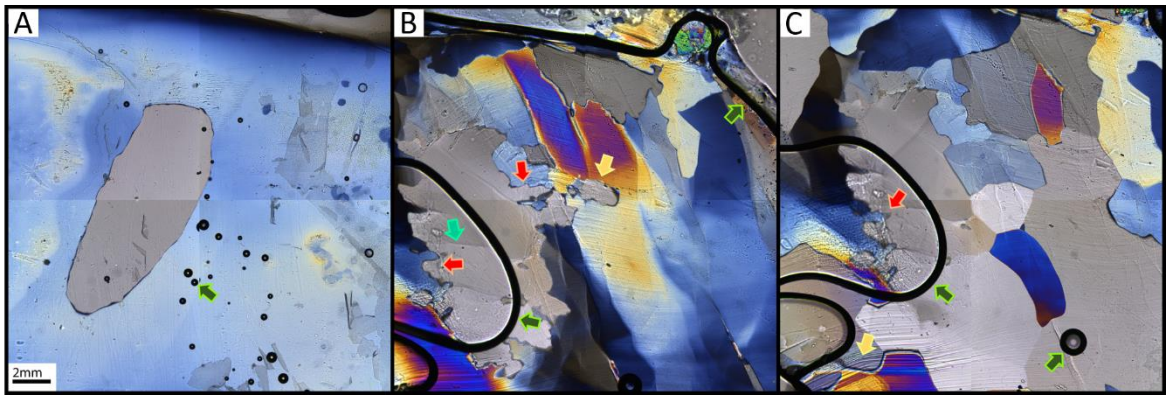

Figure 3.8: Lambda images from experiment IL_-5_01 before (A) and after deformation (B) and after 69h of annealing (C). Dark green arrow: bubbles in silicon oil. Yellow arrow: kink bands. Red arrow: lobated grain boundaries. Turquoise arrow: subgrain boundary. White triangle: holes in the section. Scale bar equals 2mm.

3.1 Grain size

The mean grain size evolution throughout the experiments measured as equal area diameter are shown in Figure 3.9. Note that the total strain in the different experiments is not the same, the values for each experiment are listed in table 3-1. For experiments were annealing was measured the graphs are marked in green for the time of annealing.

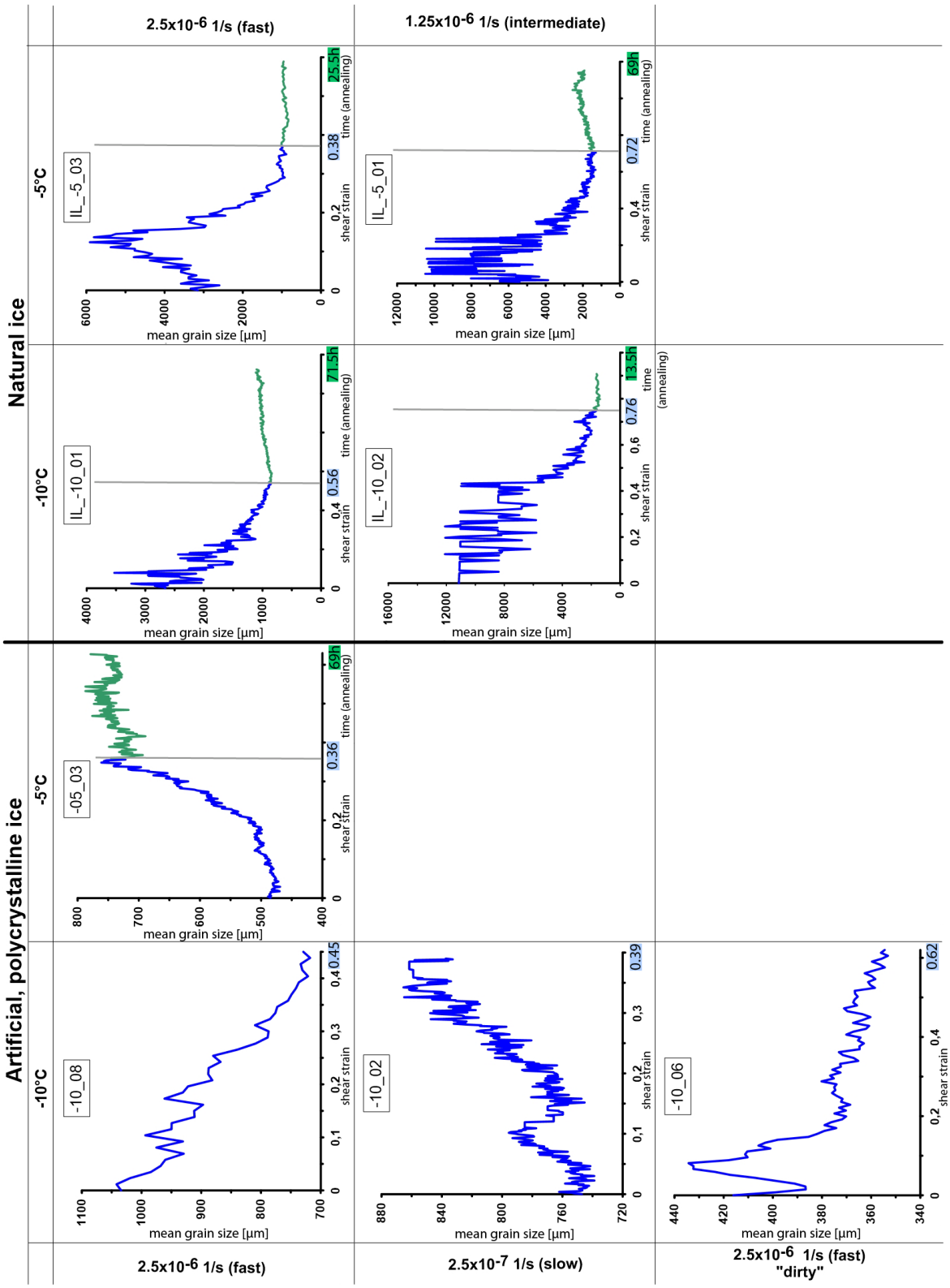

Figure 3.9: The Figure shows the mean grain size evolution in µm (y-axes) against the shear strain/annealing time (x-axis). On the left the results for the polycrystalline samples are shown and on the right for the natural ice samples. Blue numbers indicate shear strain at the end of deformation and green numbers show the time of annealing. Note that the slower experiments for the natural ice samples is about one magnitude faster compared to the artificial samples.

"Fast" experiments

The grain size evolution in the sample -10_08 shows a negative trend throughout the whole experiment with minor variations. With a starting mean grain size of about 1040µm it decreases to about 730µm at the end of the experiment with a shear strain of 0.45.

The sample deformed at the same strain rate of $2.5x10^{-6}$ 1/s but at -5°C (-5_03) starts with a mean grain size of about 480µm slightly increases to 500µm up to a strain of 0.2 before grains are growing faster to a mean size of 740µm at the end of the experiment with a shear strain of 0.38. During the annealing afterwards the grain size is slightly increasing.

The "dirty" sample -10_06 shows a decrease in grain size starting at a strain of 0.1. The initial increase visible in the graph is an artificial effect occurring during grain detection. As for sample IL_-5_03 a compromise was made to get the overall best results.

The natural ice sample IL-10_01 starts with a mean grain size of 2750µm, note that only parts of grains are visible and the real grain sizes in the original material are much greater. During deformation, the grain size decreases continuously to 1000µm at the end with a shear strain of 0.56. During the following annealing time, the grain size slightly increases.

Deformation performed with the same strain rate but at -5°C (IL_-5_03) starts at 3000µm and increases up to 5000µm at a strain of 0.12 followed by a strong decrease until strain of 0.29 to a size of 1000µm. The initial increase in grain size is an artificial effect of the analysis, as during the grain labeling process small grains are detected which do not exist in reality. This effect could be minimized by increasing the minimum grain size for the analysis, but the smaller grains growing during the later phase of the deformation would then not be detected. After the initial phase which should be more or less stable (it is not due to the artificial effect during the grain detection). After the decrease in grain size it stays stable until the deformation is stopped at a strain of 0.38. During annealing the grain size slightly increases. The decrease in size is mostly initiated through the growth of new grains along the grain boundaries.

"slow/intermediate" experiments

Both natural samples deformed at the slower strain rate ($1.25x10^{-6}$ 1/s) show an initial stable phase up to 0.2 shear strain at -5°C and 0.4 at -10°C, followed by an decrease in grain size to around 2000µm. The reached mean grain size after deformation is similar for

both even though their reached final shear strains are very different with 0.76 for the slower (IL_-10_02) and 0.36 for the faster (IL_-5_03) deformation.

For the polycrystalline samples only one deformation with a slower strain rate was done (-10_02). The mean grain size before deformation lays at 750µm and stays stable in the range from 740-760µm up to a shear strain of 0.05. Followed by an increase up to 790µm at a shear strain of 0.1 and decreases again to 760µm until a shear strain of 0.15. To finally increase until the end of the experiment to reach a mean grain size of about 830-850µm at a final shear strain of 0.39. The initiation of the grain size decrease between 0.1 and 0.15 matches the time when the electrical plug broke and the deformation was stopped for a while.

The slower deformed samples tend to higher grain sizes compared to the faster ones. As not all samples were deformed until they reached a stable mean grain size caution is needed for comparison.

3.2 Fabric (<c>-axis orientation)

Orientations were measured with the top of the page representing a 'north' direction. The density plots (Figure 3.10 and 3.11) showing the crystallographic-preferred orientation (CPO) have color coding from white (low density) over blue, green, yellow to red (high density). For each plot, the minimum and maximum density value is displayed, and the color bar is set to be between 0 (white) to maximum density (red). These plots give information on the distribution before and after deformation and after annealing when measured.

To follow the pattern development throughout the deformation a ternary path diagram is shown in Figure 3.12. The corners of the ternary diagram indicate different patterns for the <c>-axis orientation, and the position of the data point represents the amount on how strong this pattern is represented in the distribution for each step. These patterns are point (P), girdle (G) and random (R). The diagrams (Figure 3.12) show the path from the starting pattern (black circle) during deformation (black lines) and annealing (red lines) to the end of the experiment (red triangle). Changes in pattern can be observed throughout deformation progress.

A more visual impression on the <c>-axis orientation is given by the hard/soft images (images in chapter 3.2.3). Here the colors indicate the orientation in terms of an easy glide position in relation to the deformation direction. Images for all experiments before deformation, after deformation, and after annealing are attached in the appendix.

3.2.1 Density plots

All polycrystalline samples (Figure 3.10) show a random distribution of the <c>-axis orientation before the deformation. All maximum density values are small.

After deformation all the artificial samples develop a trend towards 45° to the deformation direction. Only the “dirty” sample -10_06 shows a greater angle compared to the others. This trend can be seen even though shear strains are low, between 0.36 for -5_03 to 0.62 for -10_06. Also, for -10_08 the effect is less strongly developed even though it has a shear strain of 0.45 and therefore was more deformed than -10_02 and -5_03.

For the natural ice samples (Figure 3.11), a seemingly strong fabric weakens and shows a slight trend towards an 45° angle to the deformation direction. Keep in mind that in these sections only 2-3 grains exist in the beginning and therefore the strong maxima at certain orientations can be misleading.

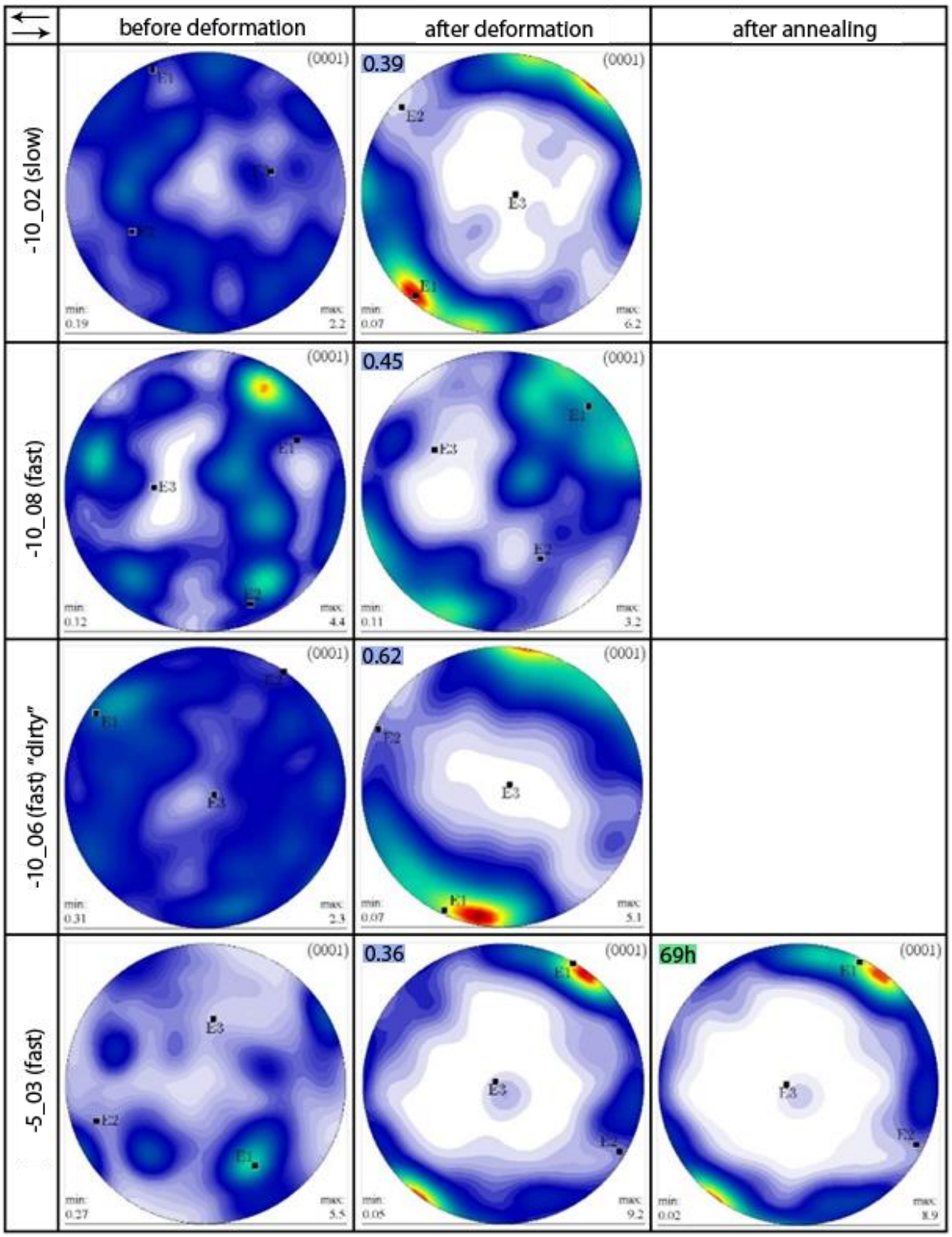

Figure 3.10: Density plots for the c axis orientation for the polycrystalline ice samples before and after deformation and for -5_03 also after annealing. Shear sense is indicated by arrows in the upper left corner. Blue numbers: final shear strain. Green number: annealing time.

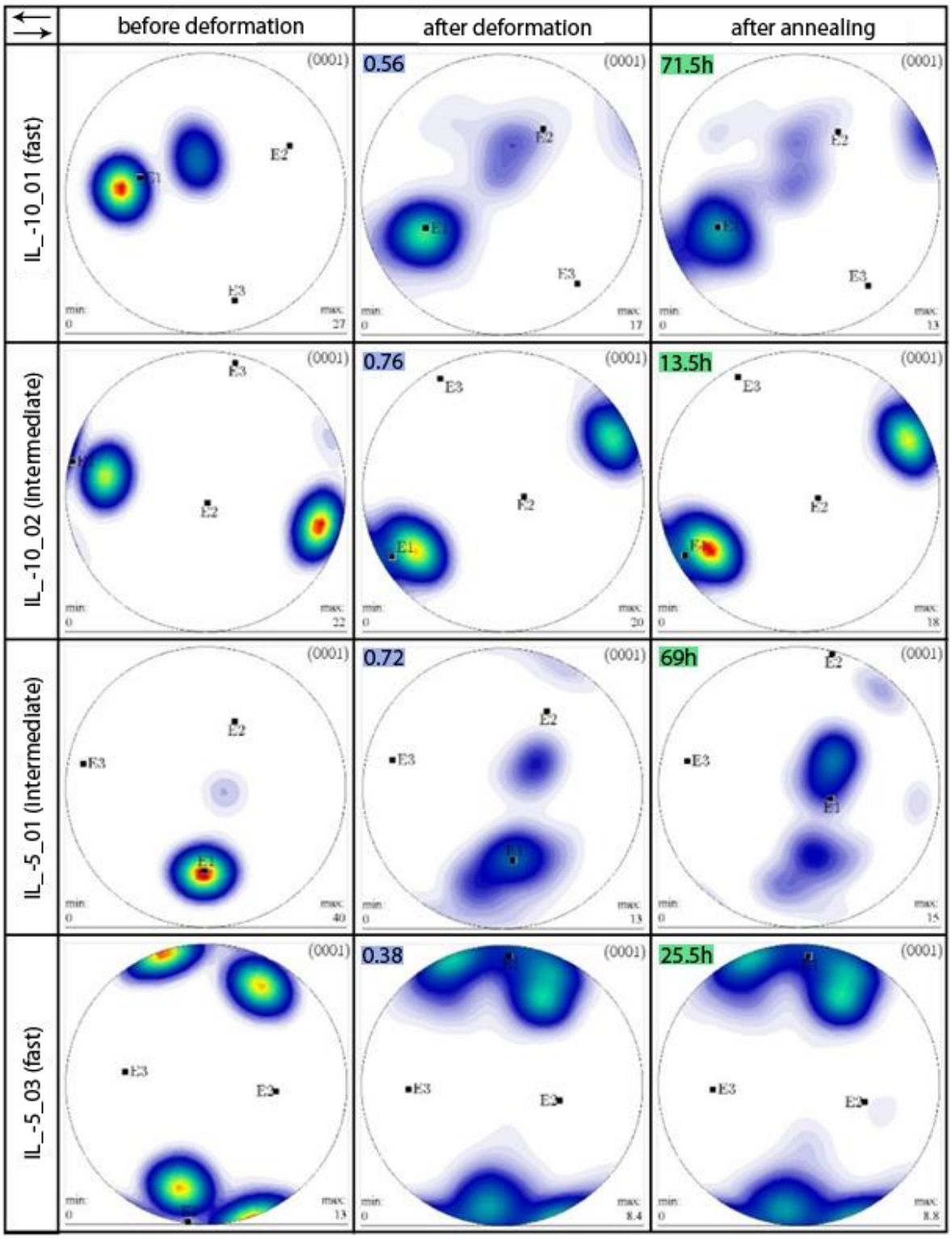

Figure 3.11: Density plots for the <c>-axis orientation for the natural ice samples before and after deformation as well as after annealing. Shear sense is indicated by arrows in the upper left corner. Blue numbers: final shear strain. Green numbers: annealing time.

3.2.2 Ternary path plots

All artificial samples (Figure 3.12) start in with a mostly random fabric and tend to evolve towards a more point pattern. Sample -10_02 (-10°C, slow) and -5_03 (-5°C, fast) both have an initial trend towards a girdle distribution before they turn towards a more point fabric.

The natural samples (Figure 3.12) all start in the point fabric corner, as they represent thin sections with few grains all measured orientations are in the same direction. IL_-5_03 (-5°C, fast) and IL_-10_02 (-10°C, intermediate) show almost no change in fabric pattern during deformation. The other two natural samples IL_-10_01 (-10°C, fast) and IL_-5_01 (-5°C, intermediate) show a path away from the point distribution towards a girdle distribution.

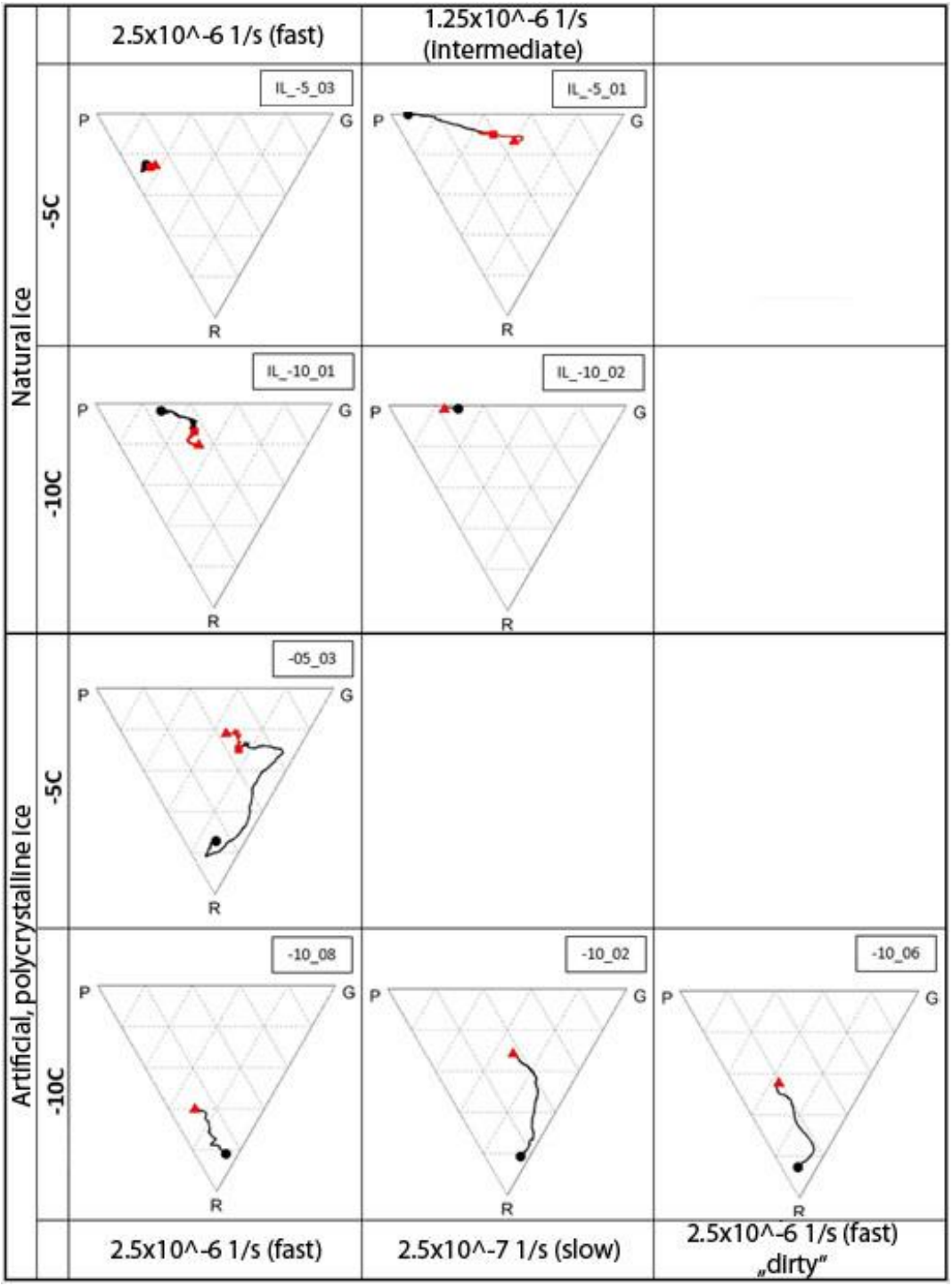

Figure 3.12: Ternary path for the <c>-axis distribution pattern showing the changes during deformation and annealing. The two rows on the top show the pathways for the natural ice samples with two temperatures and two strain rates (fast: 2.5x10^{-6}, intermediate: 1.25x10^{-6} 1/s). The two rows on the bottom show the data for the artificial ice samples at -10 °C and -5°C with the fast (2.5x10^{-6} 1/s) and slow (2.5x10^{-7} 1/s) strain rate as well as the "dirty" sample. Black: during deformation. Red: during annealing.

3.2.3 Hard/soft and orientation images

The har/soft images represent an easy way to see if the material is in favorable position to deform in respect to the orientation of the crystal lattice towards the deformation direction. Dislocation movement, which is a main factor for deformation, is energetically favored along the basal plane compared to any other direction in the lattice. A favorable position therefore would be an orientation in which the resolved shear stress goes along the basal plane.

The images presented here follow a color coding from blue (soft grains) over green, yellow, orange, red to black (hard grains). The color represents an index between 0 and 1 calculated based on the Schmidt's factor. This graphical presentation provides a tool to easily detect a general weakening/hardening in the sample or formation of weak or hard areas.

The random orientation of the <c>-axis of sample -5_03 can be seen in the density plot (Figure 3.10) and ternary diagram (Figure 3.12) and is also equally distributed throughout the thin section. No clusters of hard or soft grains are visible (see Figure 3.13). After deformation, the majority of grains are in a soft position with few hard grains in the central area. During annealing time grains in a hard position grow more than grains in soft position. For example, in the bottom center of the section a small hard grain is visible which grows during annealing to a multiple of its original size (Figure 3.13 B and C). Patches of hard and soft grains show a weak pattern of alignment along the axis of maximum extension.

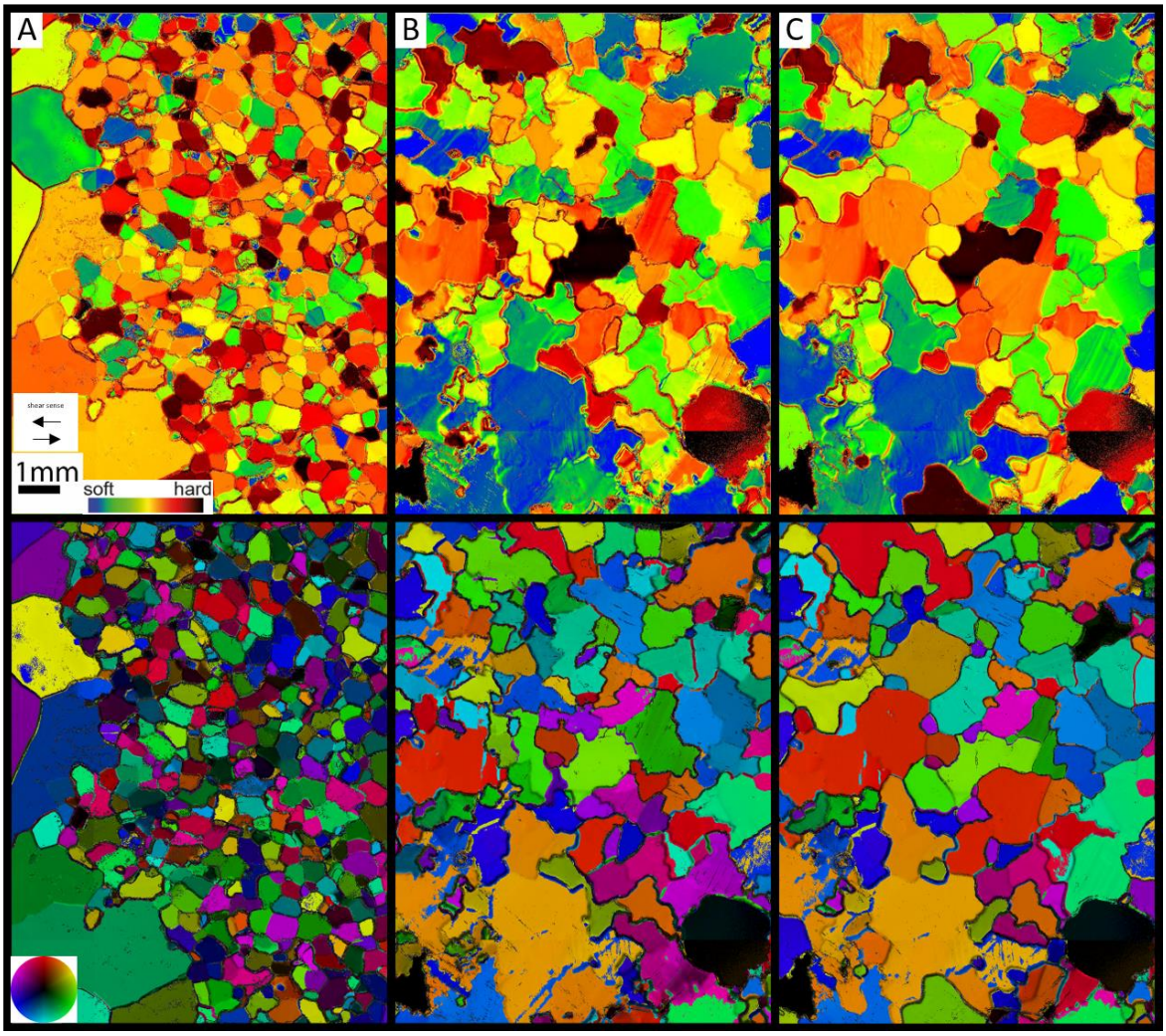

Figure 3.13: Sample -5_03 (fast). Arrows indicate shear sense. Top row: Indications of grains in easy and hard glide position depending on the orientation of the <c>-axis towards the deformation direction. Color ranges from blue (soft) over green, yellow, orange red to black (hard). The round red/black area on the bottom right is a hole and not a grain. Bottom row: <c>-axis orientation before deformation (A), after deformation (B) and after annealing time (C) representing the orientations based on which the hard/soft criteria for the top row pictures were calculated.

As can be seen in the density plots (Figure 3.10) and ternary diagram (Figure 3.12), sample -10_02 (Figure 3.14) features a random <c>-axis orientation overall in the starting material. The distribution of orientations throughout the sample is not fully random as it contains patches with intermediate grains, in relation to their hard/soft criteria, especially on the left side. And several patches of soft grains. After deformation, the area fraction of soft grains has increased by spreading from the original patches. A weak developed elongation of the hard and soft patches towards the maximum extension direction can be seen.

Individual grains are separated into several sections with hard and soft areas. Sectioning is mostly north south oriented.

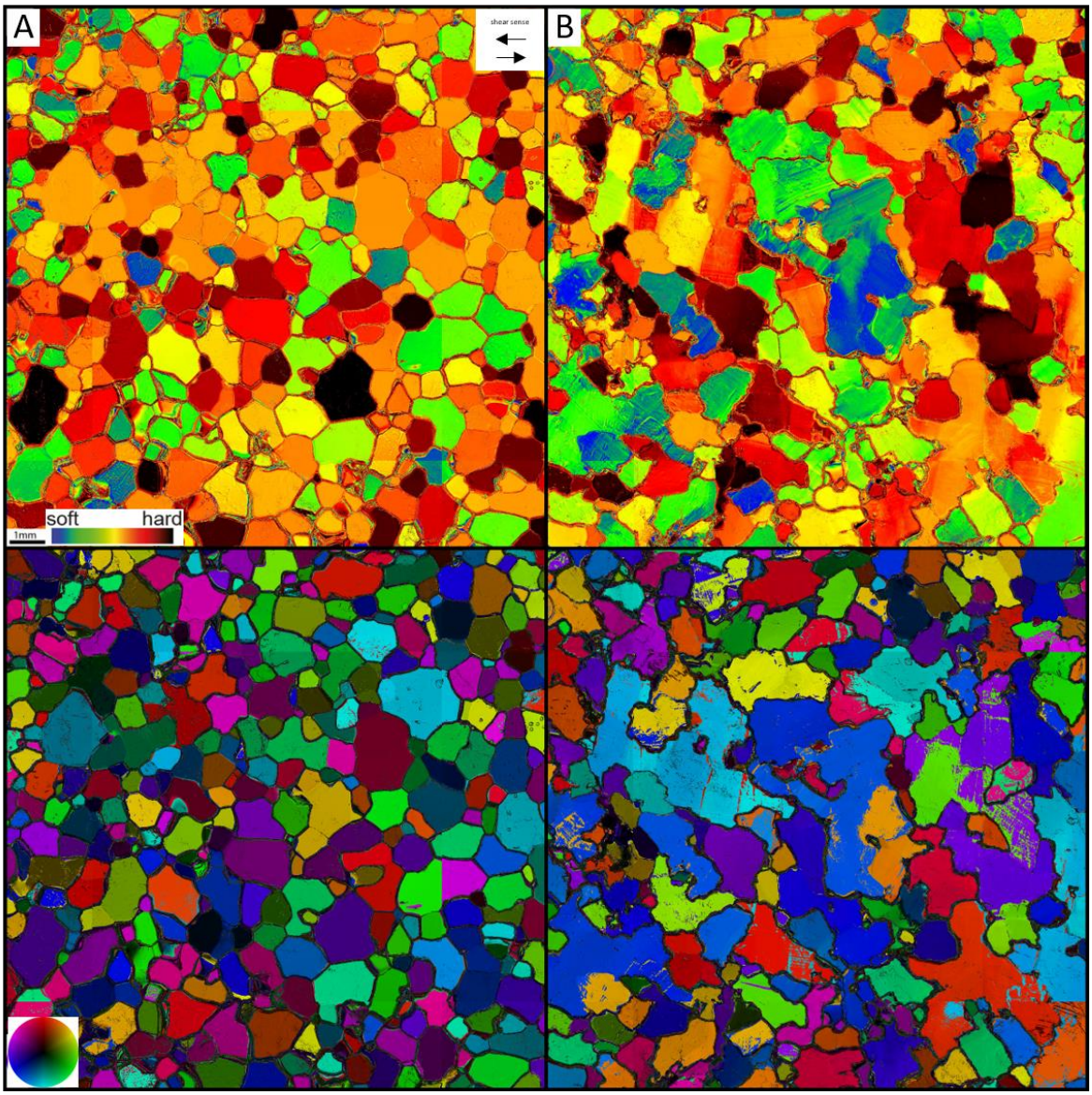

Figure *3.14: Sample -10_02 (slow). Arrows indicate shear sense. Top row shows visualization of the hard/soft criteria with a color bar from blue (soft, easy glide) over green, yellow, orange, red to black (hard, hard glide) before (A) and after (B) deformation. Calculation of the criteria is based on the orientation of the <c>-axis towards deformation direction. <c>-axis orientation of the area is shown in the bottom row.*

Sample -10_06 (Figure 3.15) features an overall random distribution of the <c>-axis orientation in terms of equal occurrence of all directions and special distribution in the

sample. An influence of the small amount of particle content is not visible in the starting material.

After deformation areas with hard grains are dominant in the most sheared area with small soft grains in between. Patches are weakly elongated towards the maximum extension direction.

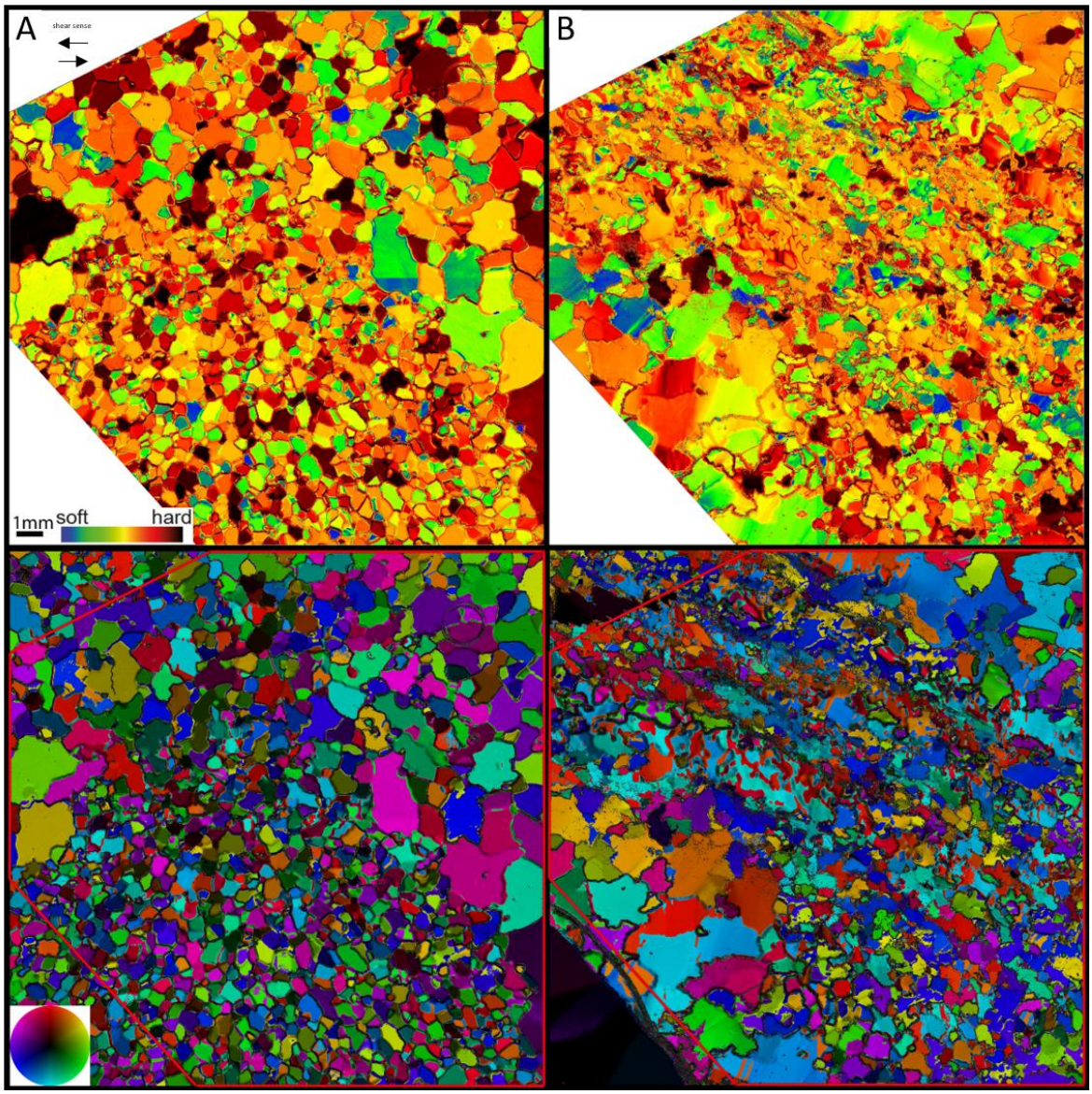

F*igure 3.15: Sample -10_06 (fast, "dirty"). Arrows indicate shear sense. Top row shows visualization of the hard/soft criteria with a color bar from blue (soft, easy glide) over green, yellow, orange, red to black (hard, hard glide) before (A) and after (B) deformation. Calculation of the criteria is based on the orientation of the <c>-axis towards deformation direction. <c>-axis orientation of the area is shown in the bottom row. Red outline marks analyzed area.*

The starting material of sample -10_08 (Figure 3.16 A) shows a random distribution of <c>-axis orientation but the special distribution is not fully random. In the upper part of the section is an area with bigger soft grains surrounding few hard grains. Areas with new grains grown during deformation are preferably soft (Figure 3.16 B). Patches of hard and soft grains are elongated along the maximum extension direction. Small new grains grown in the brittle fractures are preferably soft.

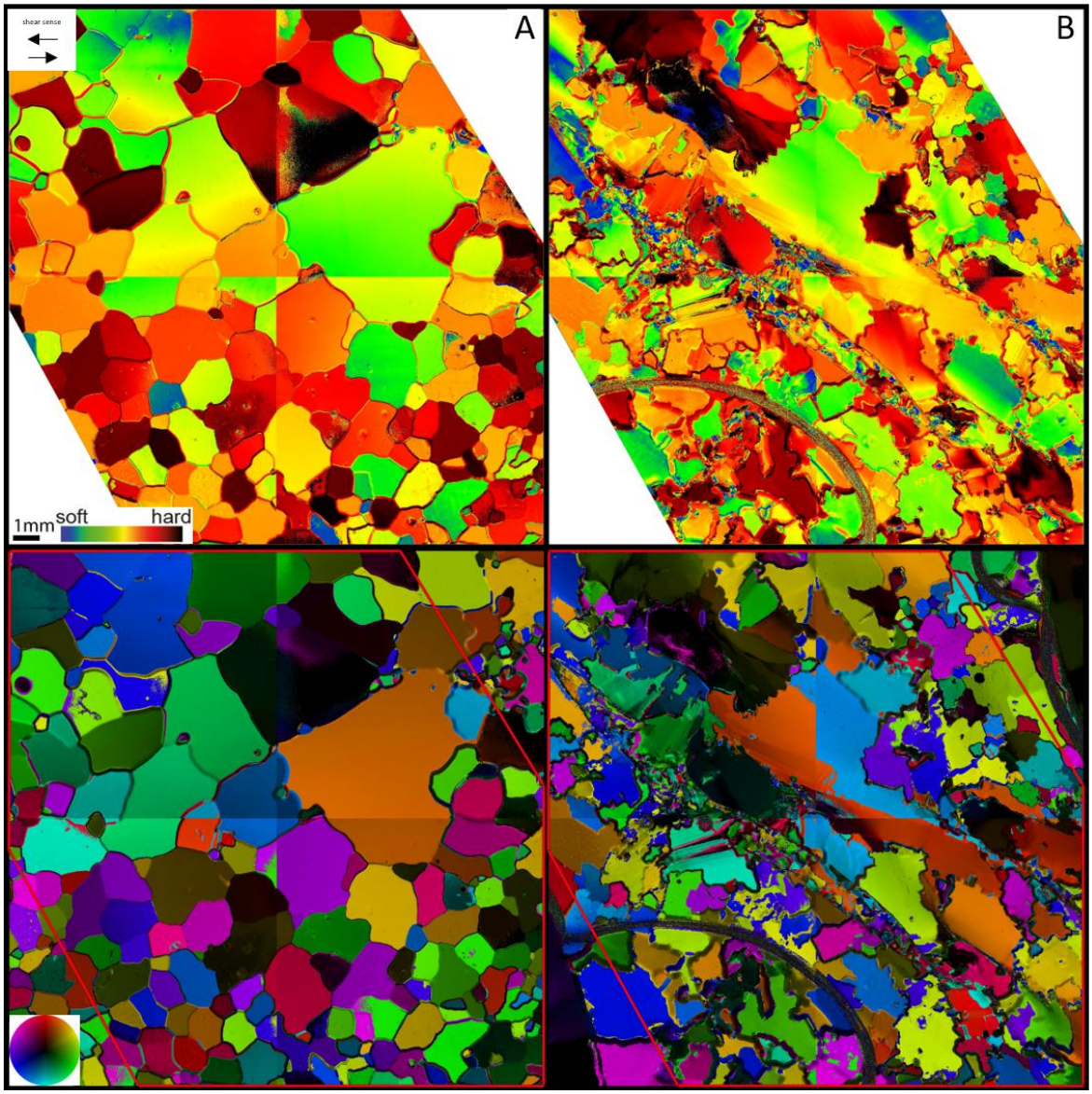

Figure 3.16: Sample -10_08 (fast). Arrows indicate shear sense. Top row shows visualization of the hard/soft criteria with a color bar from blue (soft, easy glide) over green, yellow, orange, red to black (hard, hard glide) before (A) and after (B) deformation. Calculation of the criteria is based on the orientation of the <c>-axis towards deformation direction. <c>-axis orientation of the area is shown in the bottom row. Red outline marks analyzed area.

The starting conditions of sample IL_-5_01 are a single hard grain embedded within a bigger grain with an intermediate orientation in relation to the hard/soft criteria (Figure 3.17). The smaller grain weakens during deformation but is still in a hard glide position. The surrounding big grain segregates in softer zones mainly in the upper part of the section with an elongation of about 5° towards west from the north south direction. New grains grown during annealing in the area of the old big grain tend to have a steep dipping <c>-axis and are mainly harder than the original surrounding grain.

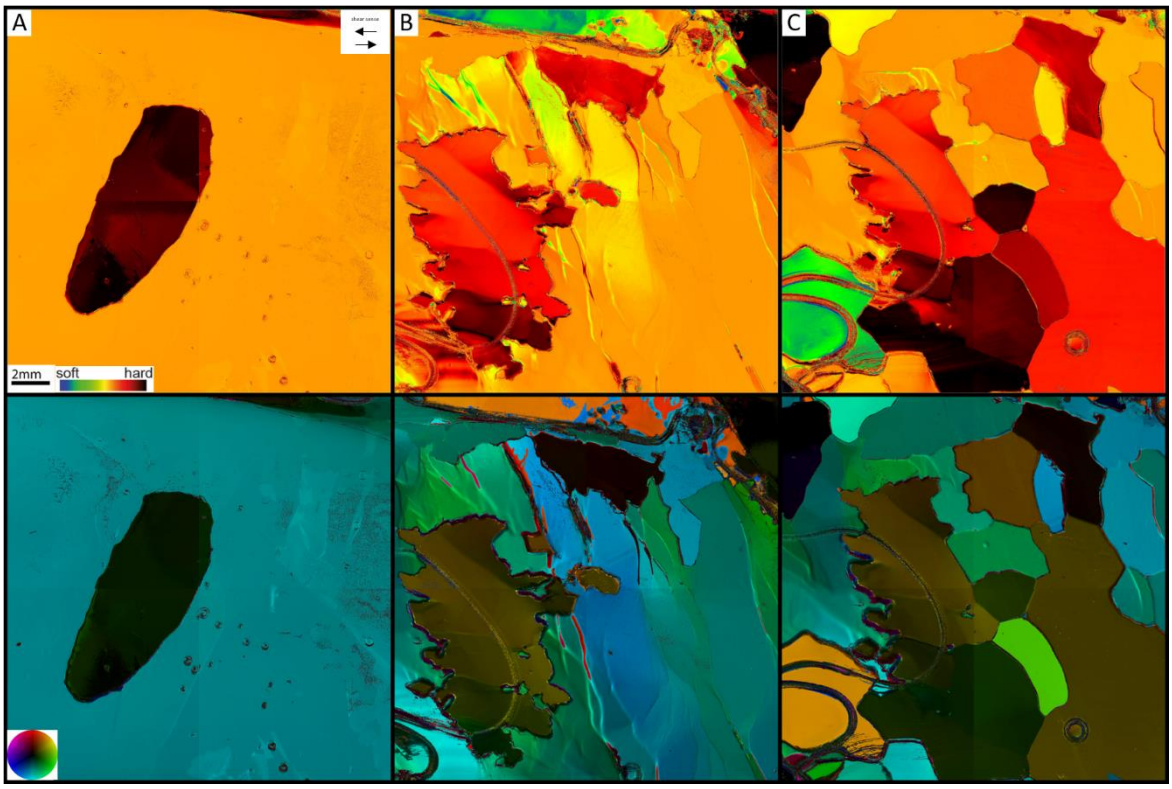

Figure 3.17: Sample IL_-5_01 (intermediate). Arrows indicate shear sense. Top row shows visualization of the hard/soft criteria with a color bar from blue (soft, easy glide) over green, yellow, orange, red to black (hard, hard glide) before (A) and after (B) deformation as well as after annealing (C). Calculation of the criteria is based on the orientation of the <c>-axis towards deformation direction. <c>-axis orientation of the area is shown in the bottom row.

The three grains in the section of sample IL_-5_03 start with similar orientations of the <c>-axis with two grains in a soft position and one in an intermediate position (Figure 3.18 A). During deformation elongated areas develop with elongation towards the maximum extension direction. The developed areas tend to be harder than the original grain (Figure 3.18 B). The borders can be sharp but still are not necessary a grain boundary. New grown small grains tend to have an orientation with a softer criterion.

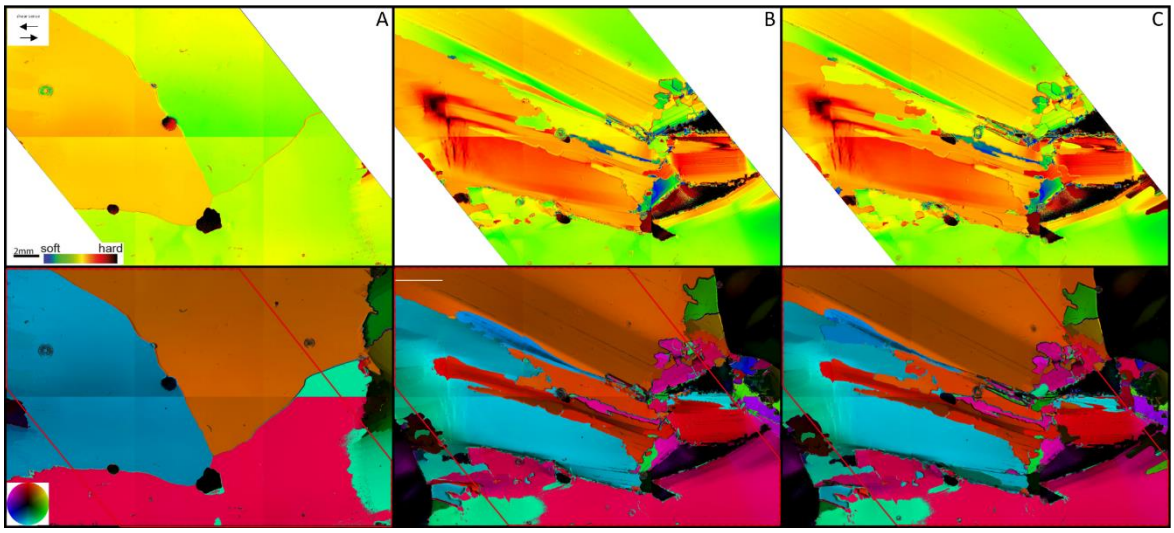

Figure 3.18: Sample IL_-5_03 (fast). Arrows indicate shear sense. Top row shows visualization of the hard/soft criteria with a color bar from blue (soft, easy glide) over green, yellow, orange, red to black (hard, hard glide)) before (A) and after (B) deformation as well as after annealing (C). Calculation of the criteria is based on the orientation of the <c>-axis towards deformation direction. <c>-axis orientation of the area is shown in the bottom row. Red outline marks analyzed area.

The starting conditions in IL_-10_01 are an intermediate to hard grain imbedded in a hard surrounding grain (Figure 3.19). New grains grown along grain and subgrain boundaries during deformation are mainly soft leading to elongated areas of t small soft grains between areas of intermediate to hard grains (Figure 3.19 B). During annealing soft grains grow bigger mainly on areas were the original grain boundary was (Figure 3.19 C).

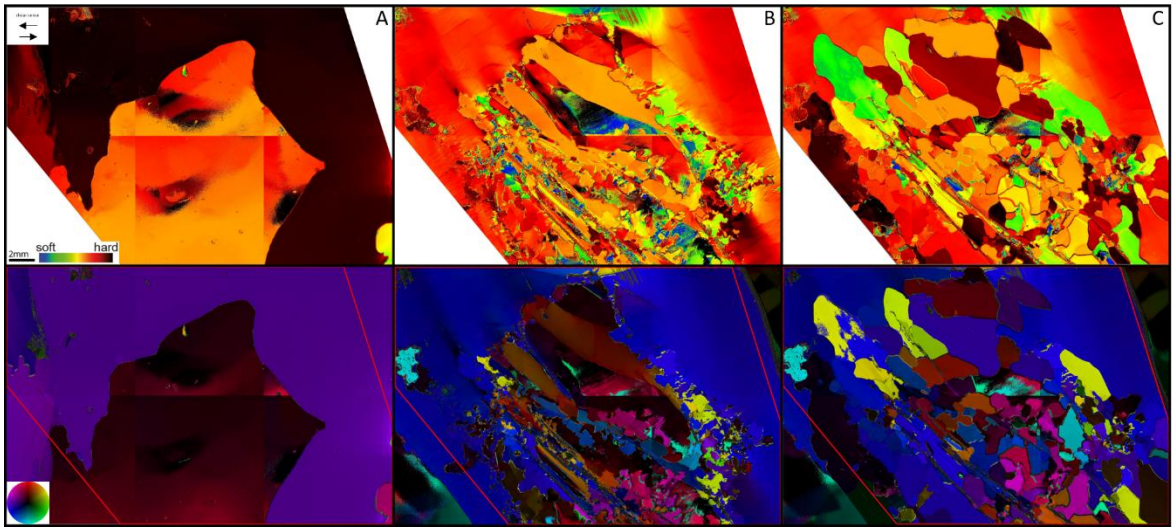

Figure 3.19: Sample IL_-10_01 (fast). Arrows indicate shear sense. Top row shows visualization of the hard/soft criteria with a color bar from blue (soft, easy glide) over green, yellow, orange, red to black (hard, hard glide) before (A) and after (B) deformation as well as after annealing (C). Calculation of the criteria is based on the orientation of the <c>-axis towards deformation direction. <c>-axis orientation of the area is shown in the bottom row. Red outline marks analyzed area.

The two intermediate to hard grains in the starting material of sample IL_-10_02 (Figure 3.20 A) rotate during deformation resulting in big areas in a soft position (Figure 3.20 B). Still there are patches of hard areas diagonally throughout the section with a stripy pattern related to the developed kinkbands.

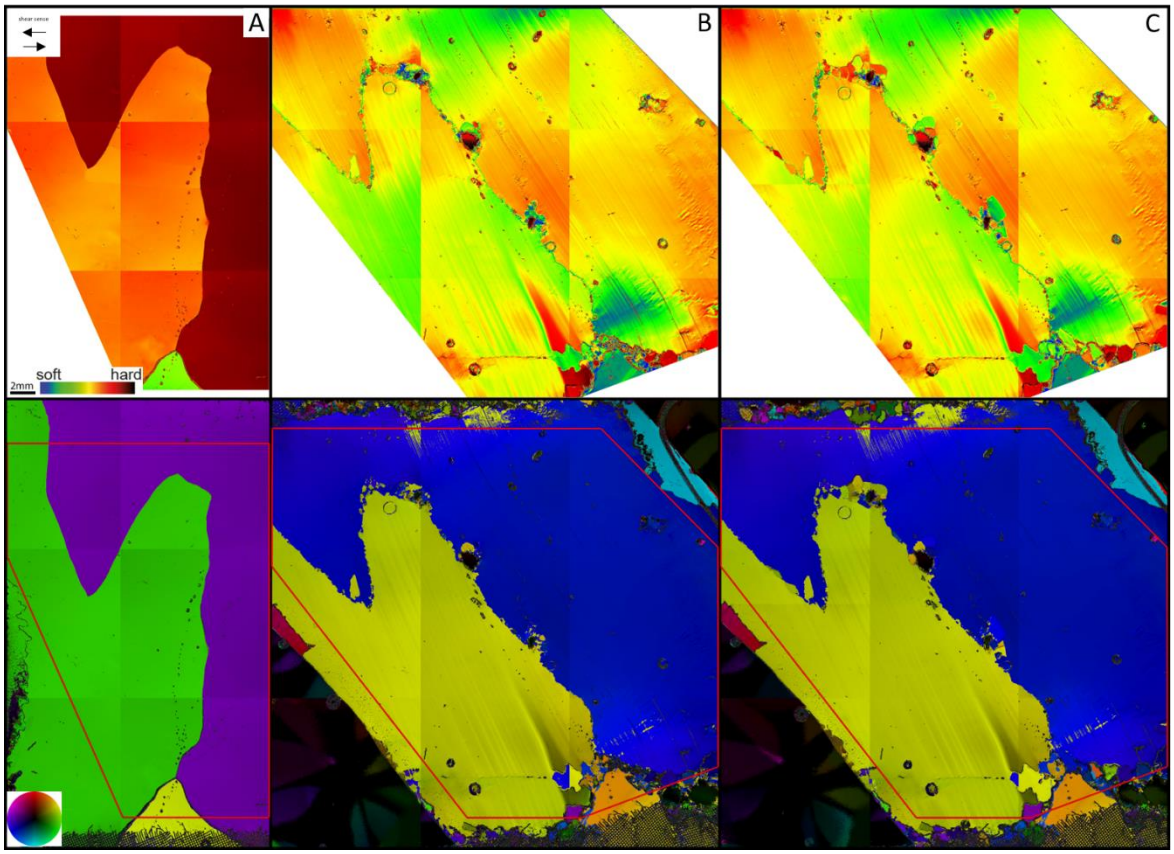

Figure 3.20: Sample IL_-10_02 (intermediate). Arrows indicate shear sense. Top row shows visualization of the hard/soft criteria with a color bar from blue (soft, easy glide) over green, yellow, orange, red to black (hard, hard glide) before (A) and after (B) deformation as well as after annealing (C). Calculation of the criteria is based on the orientation of the <c>-axis towards deformation direction. <c>-axis orientation of the area is shown in the bottom row. Red outline marks analyzed area.

3.3 Shape-preferred orientation (SPO)

The shape-preferred orientation provides information on the elongation direction of the grain shapes. The evolution of the SPO for all experiments is shown in Figure 3.21. Annealing is marked in green. The data points in the diagrams represent a mean orientation of the grain elongation for each deformation step. The angle represents the main elongation direction of the grain shape starting with north as 0° and opening clockwise. For these plots (Figure 3.21) FAME software calculates an ellipse for each grain to determine the elongation orientation for each grain and then plots a mean value over all grains in the section for each time step. If there is no strong preference in shape elongation towards a specific direction the mean values will scatter a lot.

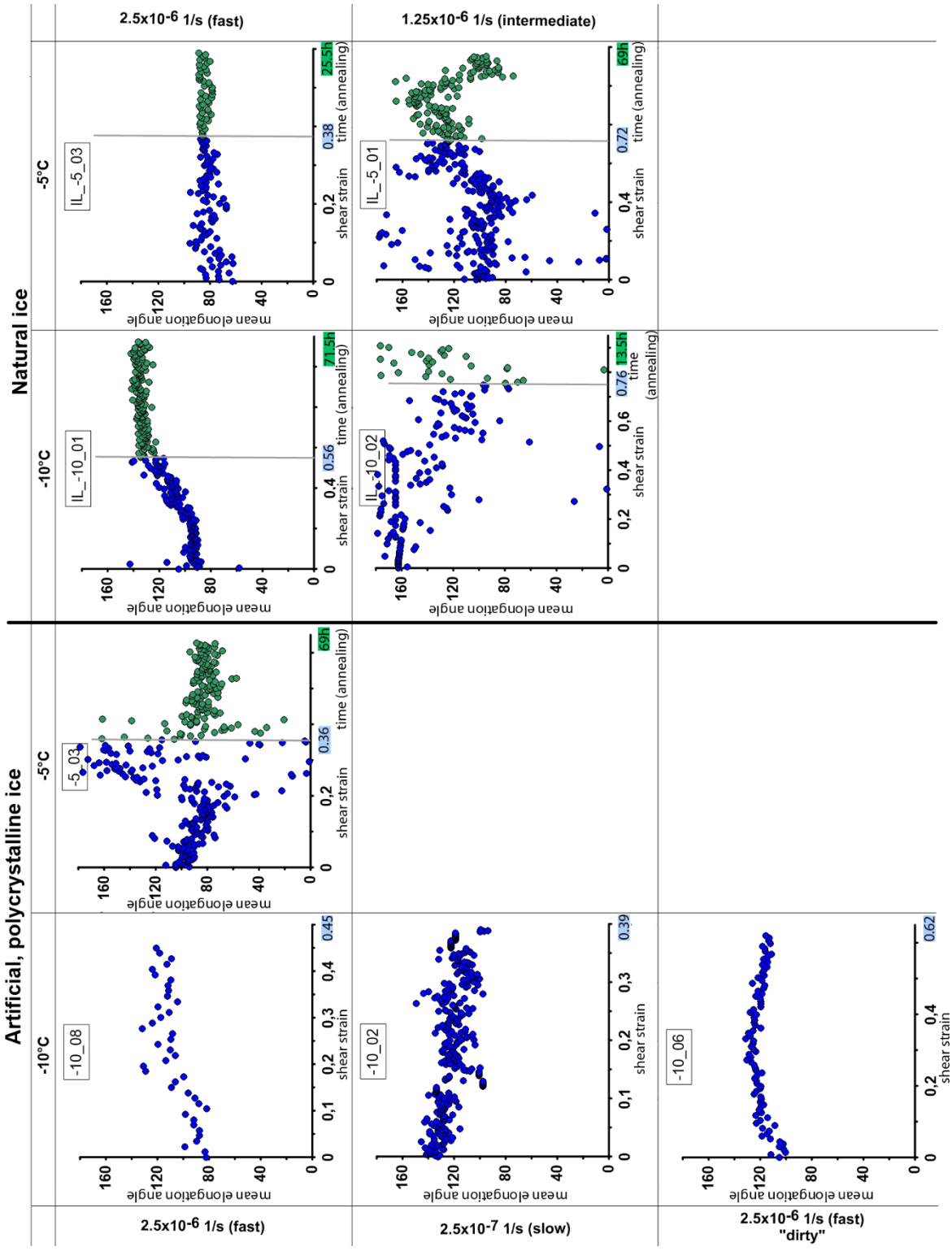

Figure 3.21: Shape-preferred orientation throughout deformation for the artificial ice samples (top) and the natural samples (bottom). Deformation progress indicated as shear strain is drawn on the x-axis and the mean elongation direction is indicated on the y-axis as angle opening clockwise from the north direction. Blue numbers indicate shear strain after deformation and green numbers time of annealing.

All experiments develop towards an elongation of the grains within an angle range of 80-140° in respect to the 'north' direction opening clockwise. A weak preferred orientation is represented by a wide scattering of the data points as small changes in grain detection between the individual deformation steps easily change it. In contrary, the better the grain detection works throughout the individual steps the closer the data points are together. Therefore, the overall trend is the relevant information coming from these diagrams.

The faster deformed natural samples (IL_-10_01 and IL_-5_03) both have a small variation in relation to neighboring data points. While the colder samples show a shift in shape-preferred orientation from 90° to 130° the warmer one sticks with the starting orientation with no significant change. The slower deformed natural samples (IL_-10_02 and IL_-5_01) start with a wider scattered preferred orientation. The colder sample shows a weak trend from about 160° towards 120°. The warmer one stars with a mean around 90° and shifts towards 120° at the end of deformation but goes back to around 90° after the annealing process.

All artificial samples deformed at -10°C have a tendency towards 120° after deformation. The one deformed at -5°C has a wide scattering towards the end of the deformation representing the fact that there is no clear elongation direction of the grains.

3.4 Grain boundaries

The calculated angles between grain <c>-axis and pole of the crystal face, listed in table 3-3, are used to link the measured angles to specific oriented planes within the crystal lattice. For every orientation only one representative is displayed. There exist six prism planes with different Miller indices, but they all have the same angle to the <c>-axis. As it is not distinguished between these faces only one representative is chosen for simplicity.

Table 3-3: Calculated angles between <c>-axis and pole of crystal faces. Miller indices for crystal face orientations occurring in ice taken from Hondoh, 2000; Faria et al., 2014; Wilson et al., 2014).

crystal face		angle <c>-axis to face pole
(0001)	basal plane	0
$\{\bar{1}\bar{1}22\}$	secondary pyramidal	19.33
$\{10\bar{1}2\}$		28
$\{01\bar{1}1\}$	(-) rhomb	41
$\{\bar{1}011\}$	pyramidal	44.16
$\{11\bar{2}1\}$	trig dipyramidal	46.8
$\{10\bar{1}1\}$	(+) rhomb	48.6
$\{2\bar{1}\bar{1}1\}$	trig dipyramidal	64.5
$\{\bar{1}0\bar{1}0\}$	prism plane	90

3.4.1 Grain boundary relationship to both neighboring grains

The grain boundaries are presented as the angle of their pole to the <c>-axis of the two neighboring grains. The bigger angle is plotted on the x axis and the smaller on the y axis leading to a triangular shaped diagram. The diagonal line represents the options when both grains share the same angle and therefore, the same type of crystal face as a boundary. The plots are corrected to take the normal distribution of the possible angles into account as described in section 2.8. Note that the scale of the color bar is not normalized throughout different experiments and therefore changes. For experiments where maxima differ a lot throughout the experiments the color bar is not equal for all plots, this is the case for IL_-10_02 and IL_-5_03.

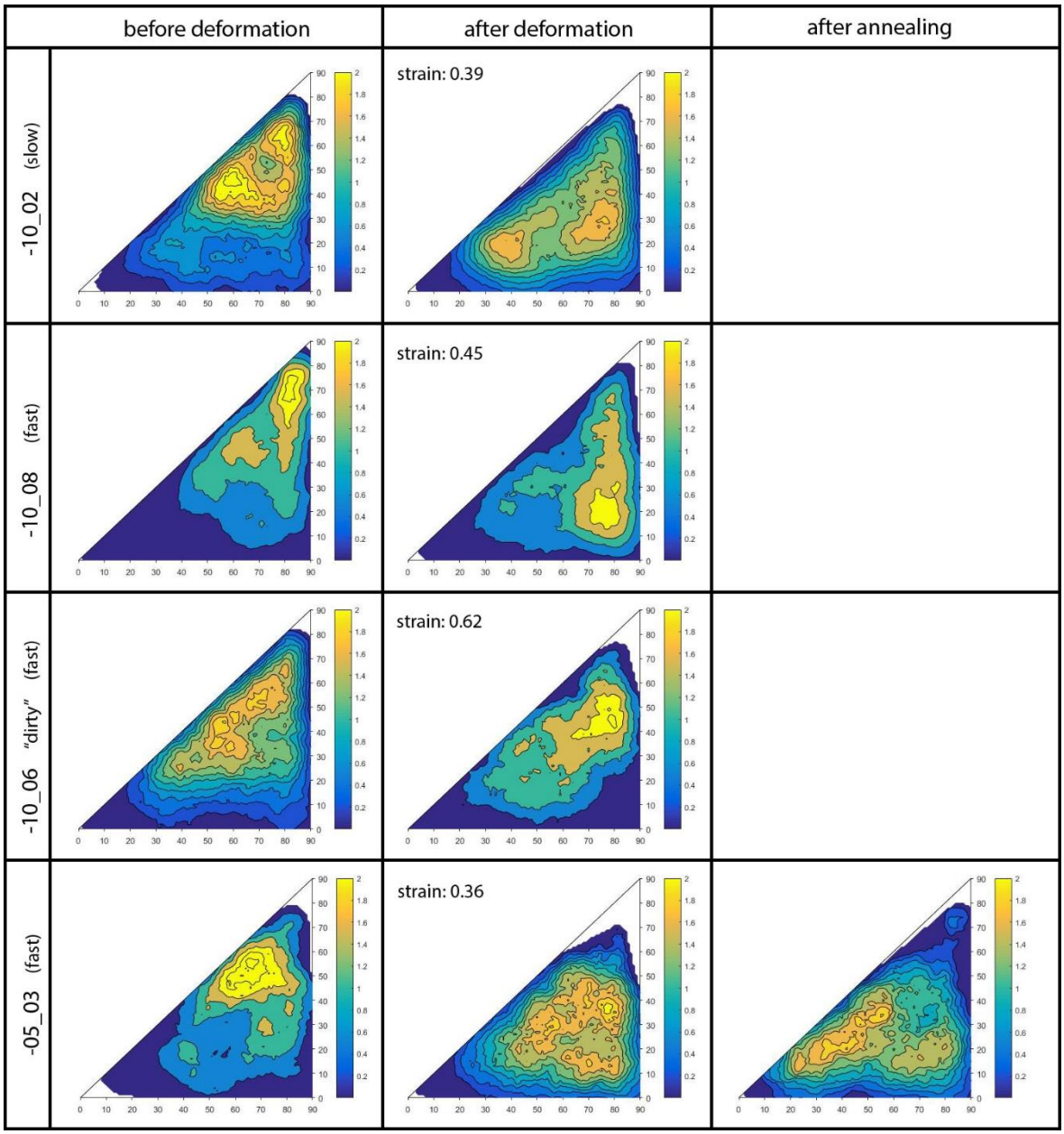

Figure 3.22: Triangle density plots representing the angular relation of the <c>-axis to the grain boundarie pole for both neighbouring grains for the artificial, polycrystalline ice samples. Distribution is shown before and after deformation as well as after annealing for -5_03. The reached shear strains are displayed within the images after deformation.

The triangle plots if Figure 3.22 show the distribution of the angle combinations for the <c>-axis of both neighbouring grains to the pole of the <c>-axis for the deformation experiments with artificial ice samples before and after deformation as well as after annealing for experiment -5_03. Reached shear stresses for each experiment are displayed next to the plot represeinting the distribution after deformation.

For all experiments with artificial ice samples a general trend to a wider distribution over different angle combinations can be seen after deformation (Figure 3.22). In all cases at least one of the angles is close to 90°, this trend is much weaker in -5_03 deformed at -5°C. During annealing time the expected preference for angles close to 90° is not seen as the maximum moves closer to smaller angles for both neighbors. Rangein from 15-40° on one side and 30-60° on the other side. Note an angle of 90° in this case represents prism and halfprism faces.

Note for -10_02 (slow) the starting point for the experiment was determined by first appearance of visible kinkbands. Therefore the initial distribution might already show some changes to the actual starting material. In addition this experiment was first started with the motor running in the wrong direction leading to a small amount of dextral shear strain before the later analyzed experiment with the wanted sinistral shear sense was started. This might have slightly changed the initial pattern.

The starting pattern of -10_06 (“dirty”) already shows a wider distribution compared to the other artificial samples. After deformation the trend to have a 90° to at least one neighbour is less strong developed.

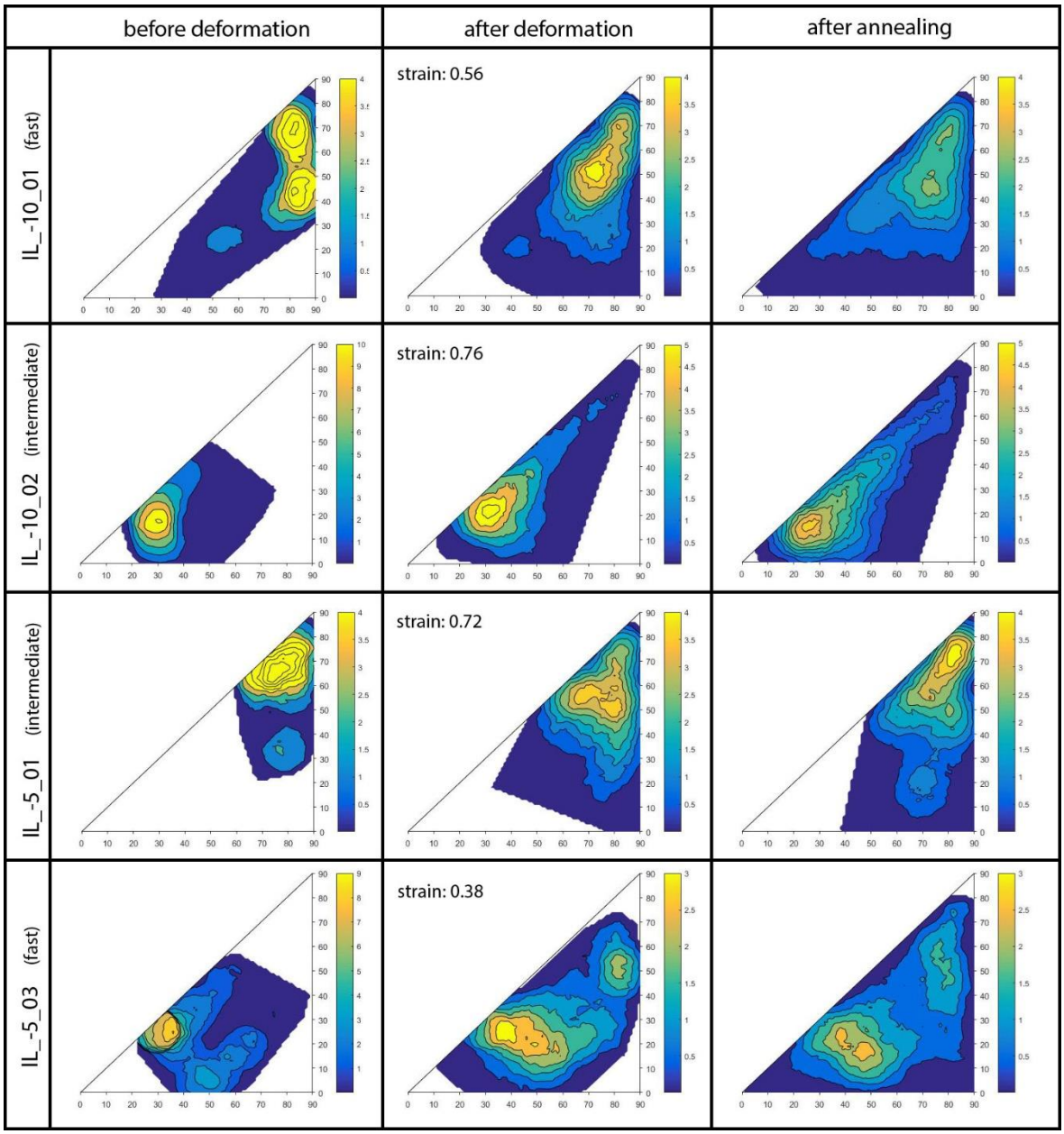

Figure 3.23: Triangle density plots for the angles of the pole of the grain boundaries to the c axes of the grains on both sides for the natural ice samples. Data before and after deformation as well es after annealing is shown. The small inlets show the data for newly grown grain boundaries while the bigger Figures show the bulk behavior.

As there are fewer grains in the natural ice samples compared to the artificial samples, the number of segments is smaller, especially in the starting material. Ranging from 352 segments in IL_-5_01 to 941 segments in IL_-10_01. The number of segments may be smaller than the minimum of about 1500 segments to be statistically significant, which has been tested empirically (by myself), therefore all measurable boundaries in the sections were measured. Test for significance was done with experiment -10_08 by measuring grain boundaries random distributed over the thin section and comparing the

outcoming triangle plots. As a minimum number of segments needed to see no relevant changes in the triangle-density plots a threshold of 1500 was set. This is 200 segments above the point no changes were seen anymore.

The unstressed samples in Figure 3.23 (left row) show only one or two combinations of crystal faces represented by single maxima in the area of specific combinations of angles connected to certain crystal faces. IL_-10_01 shows tendency from a two-point distribution to a single-point distribution throughout deformation and the pattern weakens during annealing. Even though reached shear strain in IL_-10_02 was higher the patterns before and after deformation show less change in comparison. Only the strength of the maximum weakens but no significant change in position. The comparable experiment at -5°C with the same strain rate and similar reached shear stress (IL_-5_01) shows a similarly strong weakening of the maximum and additionally a visible change in position. Note that the main difference for both experiments in addition to the temperature is the starting position in respect of the crystal faces represented at the grain boundary.

3.4.2 Single grain boundaries vs. polycrystalline systems

The individual starting condition, with respect to the angle between the boundary pole and the <c>-axes of both grains, represented in the natural samples are compared with grains with equivalent conditions in the artificial samples and plotted in triangle-density plots equal to the ones above including the correction for the mean distribution abundance of the different possible angles (Figure 3.24 and 3.25). To determine the validity of the use of the natural samples as representatives for specific situations that can be found as one of many in polycrystalline samples as well. Therefore, the starting situation was determined in the natural samples. The same combinations within a small range of variety were filtered from the polycrystalline sample -10_08. Only boundaries that could be followed throughout the deformation were taken into account for comparison of the behavior of these specific angle combinations within the polycrystalline system. This leads to very few data points (<50) and is therefore only an indication showing a trend. Between 40-50° several angles related to certain crystal faces are close together. All of them are followed and compared with the equivalent angle combinations ins ample -10_08.

Note not all combinations found in the natural samples are compared as in some cases the few boundaries which were found in sample -10_08 at the beginning could not be followed until the end of deformation. Either they were outside the observed area or completely overgrown by other grains after deformation.

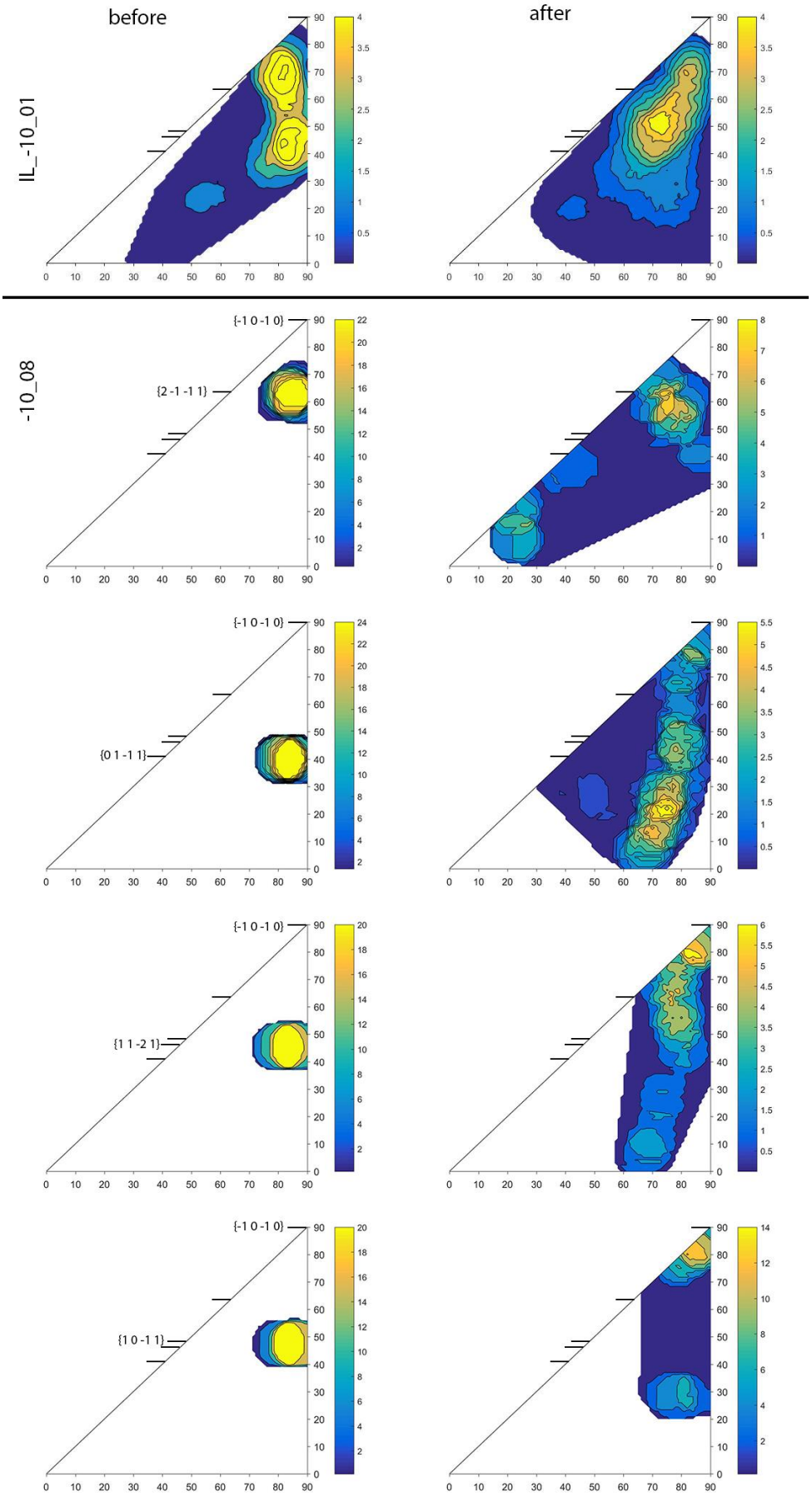
before
after
IL_-10_01
-10_08
{-1 0 -1 0}
{2 -1 -1 1}
{-1 0 -1 0}
{0 1 -1 1}
{-1 0 -1 0}
{1 1 -2 1}
{-1 0 -1 0}
{1 0 -1 1}

Figure 3.24: Bulk distribution of the grain boundary angle distribution in sample IL_-10_01 before and after deformation (top). Individual peak points from IL_-10_01 selected from sample -10_08 (bottom) for boundaries which could be followed throughout the deformation.

In Figure 3.24 the possibilities in sample IL_-10_01 are split into the individual combinations. In all cases one of the crystal faces is represented by a prism or half prism plane (both 90°) combined with $\{2\bar{1}\bar{1}1\}$ representing the upper maximum in IL_-10_01 and $\{01\bar{1}1\}$,$\{11\bar{2}1\}$ or $\{10\bar{1}1\}$ representing the possibilities of the lower maxima in IL_-10_01 as three possible crystal faces are close together in this area. Note strain rate is the same for both deformations and the reached shear strain is within a comparable range with 0.45 and 0.56.

The combination with $\{2\bar{1}\bar{1}1\}$ in the filtered data from -10_08 shows little change throughout deformation except for a few points in the range of about 20° angles for both neighboring grains. Two of the positions in the range between 40° to 50° given by $\{01\bar{1}1\}$ and $\{11\bar{2}1\}$ spread over a wide range of angles on one side of the boundary but stay with high angles on the other side. The behavior of the angles represented by a the $\{10\bar{1}1\}$ face is similar as one side remains close to 90° and the other shows a wider variety, but in this case two main spots are present. A weak maximum at around 30° and a stronger one between 80° and 90°.

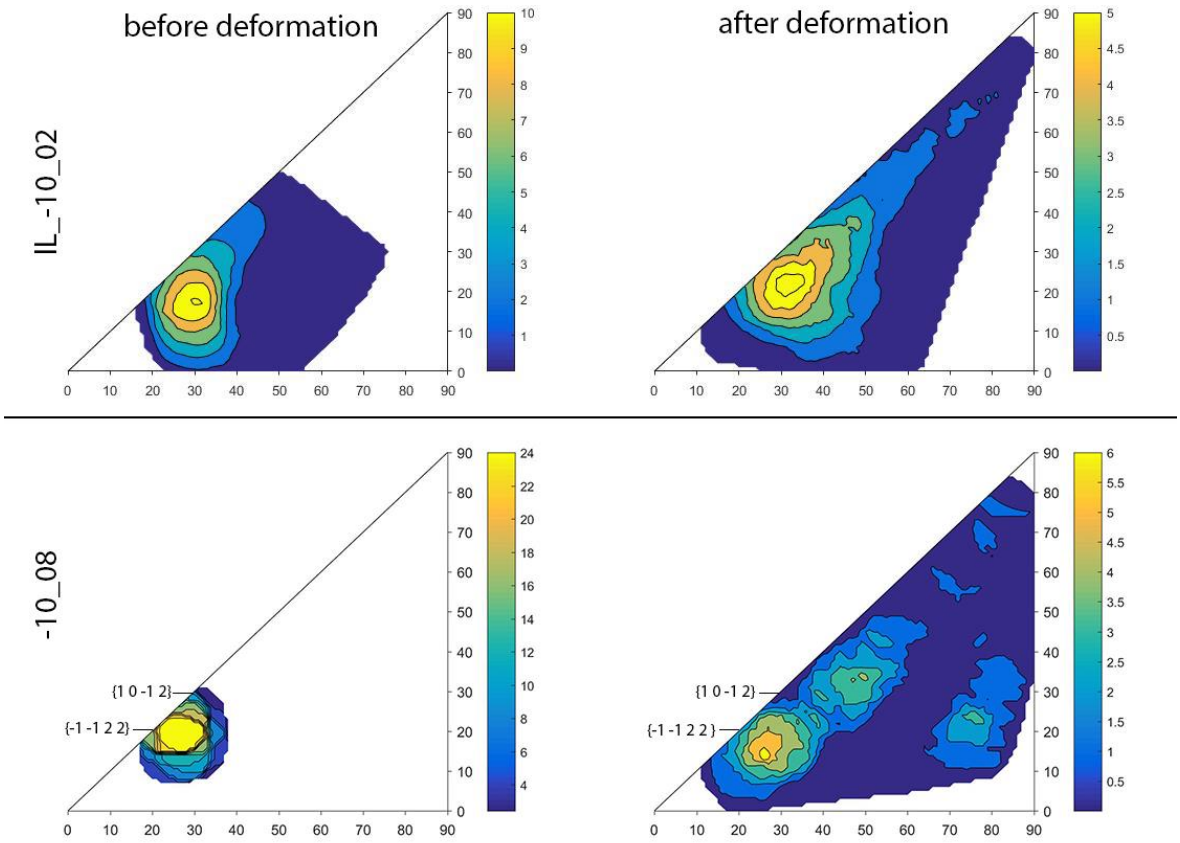

Figure 3.25: Bulk distribution of the grain boundarie angle distribution in sample IL_-10_02 before and after deformation (top). Comparabale points selected from sample -10_08 for boundaries which could be followed throughout the deformation (bottom).

A second comparison was made with the situation in IL_-10_02 represented by a combination of the $\{\bar{1}\bar{1}22\}$ and $\{10\bar{1}2\}$ crystal faces (Figure 3.25). In this case only one distinct situation was present in the natural sample and therefore only one situation was filtered from tha data from sample -10_08. Both show a similar pattern after the deformation with the maximum approximately at the same spot as before the deformation with aditional data points ranging towards higher anlges. A second weak maximum appears for the compared boundaries in -10_08 with both sides close to an angle of 20° (representing the secondary pyramidal crystal face $\{\bar{1}\bar{1}22\}$). Note the deformation temparature is the same for both experiments but the strain rate is double in the artificial sample compared to the natural. Also shear strain in the natural sample is higher (0.76) than in the artificial (0.45).

3.4.3 Grain boundary relation to one neighbour / crystal faces

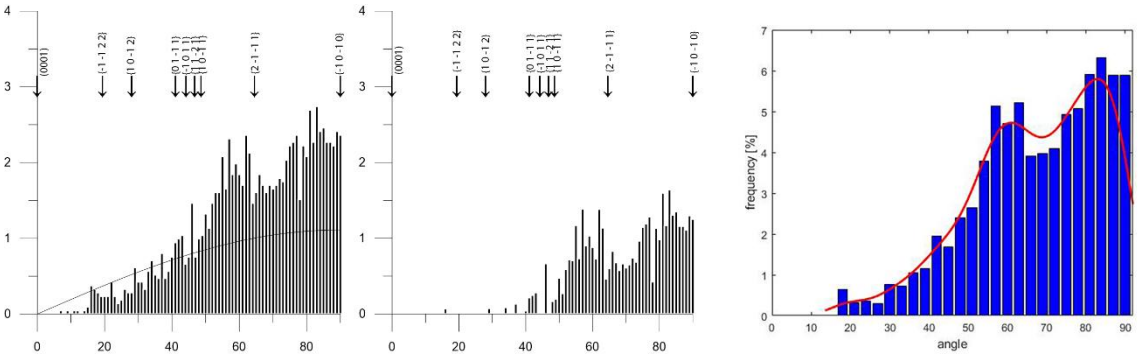

*Figure 3.26: Example from IL_-5_01 afdef showing the distribution of angles beween the grain boundary pole and grain <c>-axis. Left: Distribution of angles between grain boundary pole and <c>-axis from the measured segments with bins of 1°. Positions for distinct crystal faces are indicated with arows, note only one Miller Indice describing a face with this angle is indicated. The solid line represents the uniform distribution for the total abundance of the different angles. The uniform distribution is defined as 1.111*sin(angle grain boundary pole to <c>-axis), while the sinus needed to transfere from a 3D to a 2D uniform distribution. The factor 1.111 is a best fit variable determined for quarz Kruhl & Peternell, 2002), the value is expected to be similar for ice. Middle: Distribution of angles between grain boundary pole and <c>-axis with bins of 1° after substraction of the uniform distribution. Right: Distribution after substraction of the uniform distribution with bins of 3° and a fitted plot curve with derived with the kernel fitting method.*

A distribution of the angle between <c>-axis of the grain and pole of the grain boundary with steps of 1° is shown in Figure 3.26 on the left. The solid line represents the uniform distribution and is substracted leading to the secons plot in Figure 3.26 (middle) as described in section 2.8. To claryfie the picture, bins with a width of 3° were join a fitting curve added (Figure 3.26, right). All histogram plots are attached in the appendix.

The experiments can be distinguished into 3 groups related to the reached shear stains. Low shear strain up to 0.39 (green/blue colors), intermediate shear strains >0.39 and up to 0.62 (black/gray colors) and high shear strains between 0.72 and 0.76 (orange colors). Note the “dirty” experiment lies in the intermediate filed and is shown in brown and high shear strains only referes to the highes reached ones in the performed experiments. This color code is continuous for all following plots.

The position of the maxima of the fitted plots before and after deformation as well as after annealing are displayed in Figure 3.27. Every maxima is related to a specific orientation fitting colse to the orientation of certain crystal faces (see table 3-3).

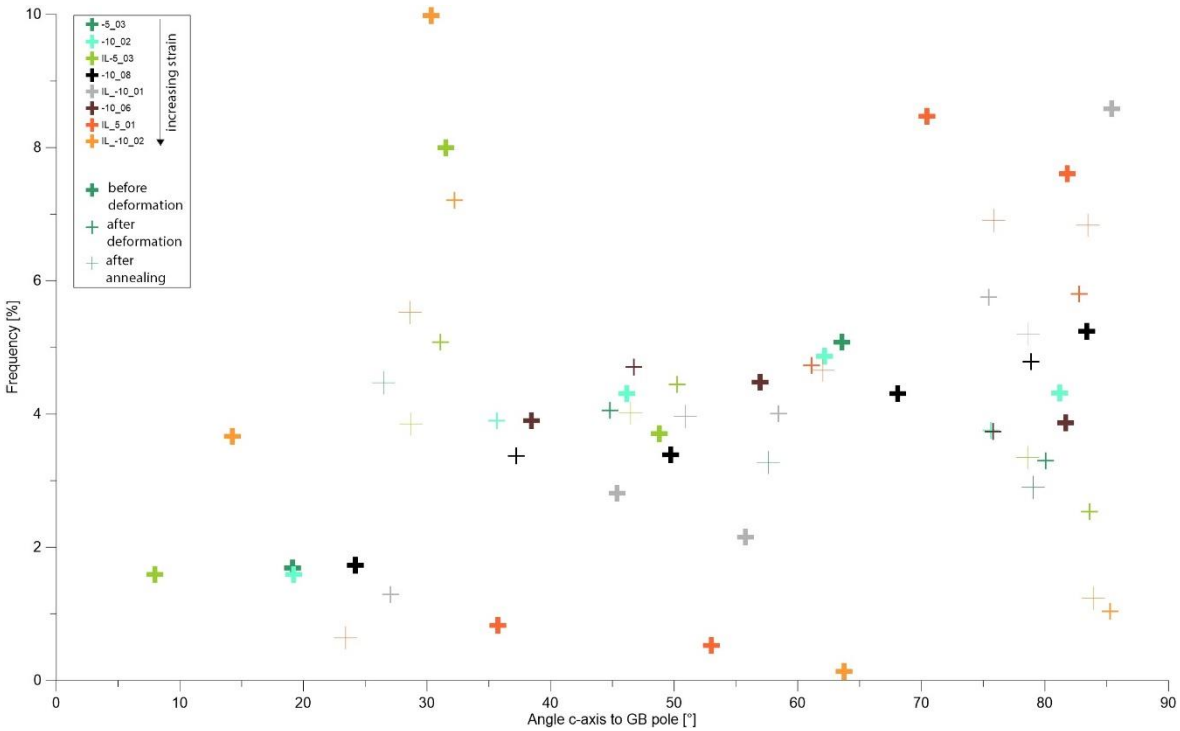

Figure 3.27: The relative abundance of angles between <c>-axis and grain boundary pole for each maximum of the fitted plots.

Highest frequencies are only reached before deformation, a general trend towards more and weaker maxima after deformation can be observed.

A mean value for occurring angles between <c>-axis and grain boundary pole was determined to observe general changes during the deformation (Figure 3.28). Solid and dashes lines indicate the strain rates, color of the lines the deformation temperature and symbols represent the mean angles before and after deformation and after annealing if available. The mean for all experiments tends towards angles between 45-55°. No trend in respect of temperature, strain rate or strain is detected.

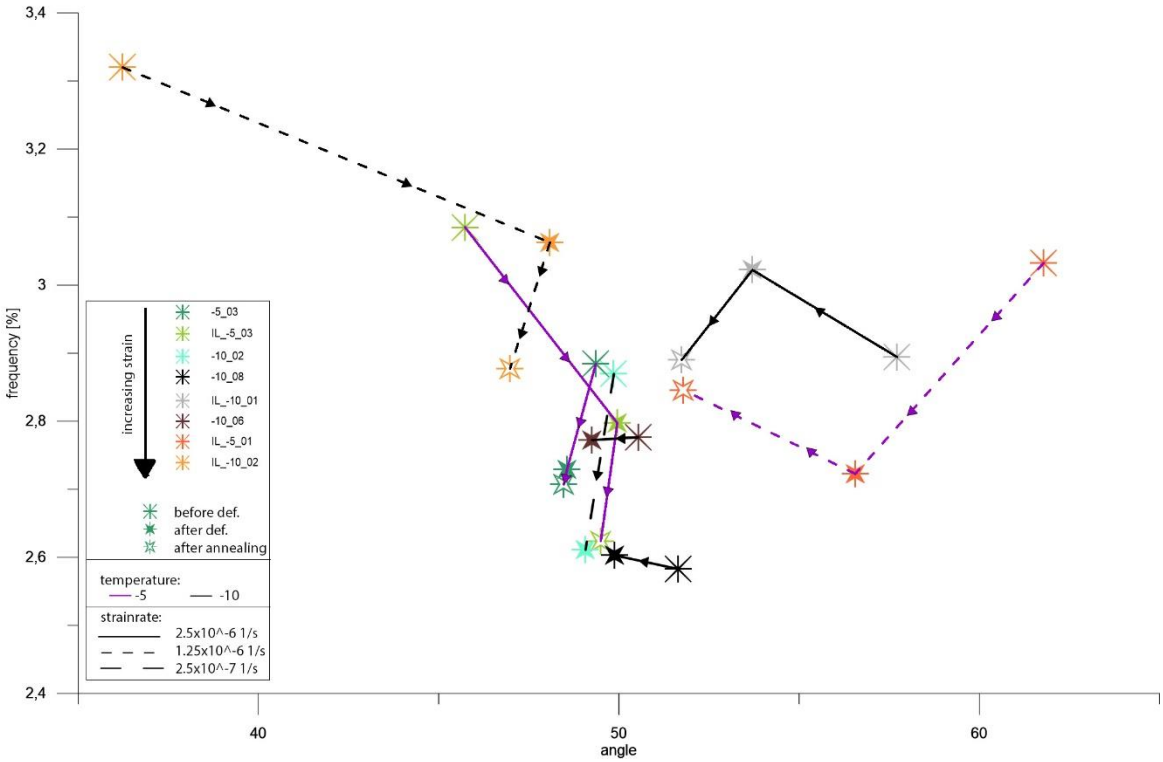

Figure 3.28: Frequency of the mean angles between grain boundary pole and ice <c>-axis for all experiments before and after deformation and after annealing if available. Lines connect data point from one experiment indicating strain rate and deformation temperature by pattern and color.

3.4.4 GB dip angles

Dip angles of the grain boundaries have been determined before and after deformation and are shown in Figure 3.29 as a cumulative plot. In the starting material dip angles are mainly steep with around 90% being above 70°, only IL_-10_01 shows much shallower dip angles in the beginning with only 75% of the angles above 70°. The situation after deformation is relative uniform for all experiments and shows around 80% of the angles being above 70°. A shift towards shallower dip angles can be observed.

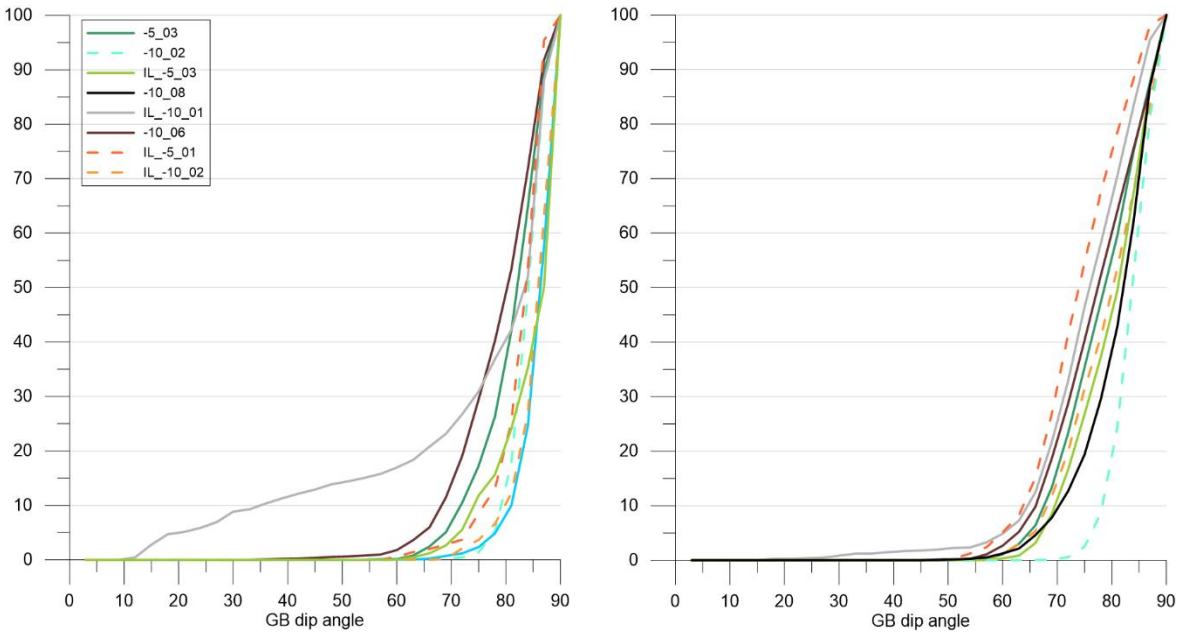

Figure 3.29: Cumulative plot of dip angles of grain boundaries before (left) and after (right) deformation. Dipping relative to the plane of observation equal to thin section plane and going downwards. Legend is sorted by increasing shear strain from top to bottom. Solid lines represent strain rates of $2.5x10^{-6}$1/s, dashed lines refer to slower strain rates of $1.25x10^{-6}$1/s and $2.5x10^{-7}$1/s for sample -10_02.

3.5 Shear fractures and step-like grain boundary traces

Some experiments feature some special observations such as brittle fractures or grain boundaries in a stepping pattern. Both features can be seen in sample -10_08. Figure 3.30 where the retardation images are shown on the left and for comparison the lambda images at the same shear strains are displayed next to it. While the initiation of the fracture is barely visible in the lambda image it can be clearly seen in the retardation image. The change in color indicates a thickening at this specific point in the thin section which can be explained by folding of the section above and below the observed image plane finally leading to a fracture. The fracture spreads with an 45° angle to the deformation direction while the tips slightly bend towards the boundaries of the initiated sheared area. A second initiation point develops close to the first one (Figure 3.30 second picture) and they join before the fracture opens. As soon as the fracture opened small grains start growing in the area. Three more occur parallel to the first set.

Grain boundaries shaped like steps occur in the same sample but can only be seen within small range of the orientation of the grain boundary, between 68-72°. These patterns can also be detected in other experiments at boundaries with similar strike directions (e.g. IL_-5_01, IL_-10_01). Not all boundaries oriented in that way show this pattern, another factor needs to be relevant for the possibility of developing this feature.

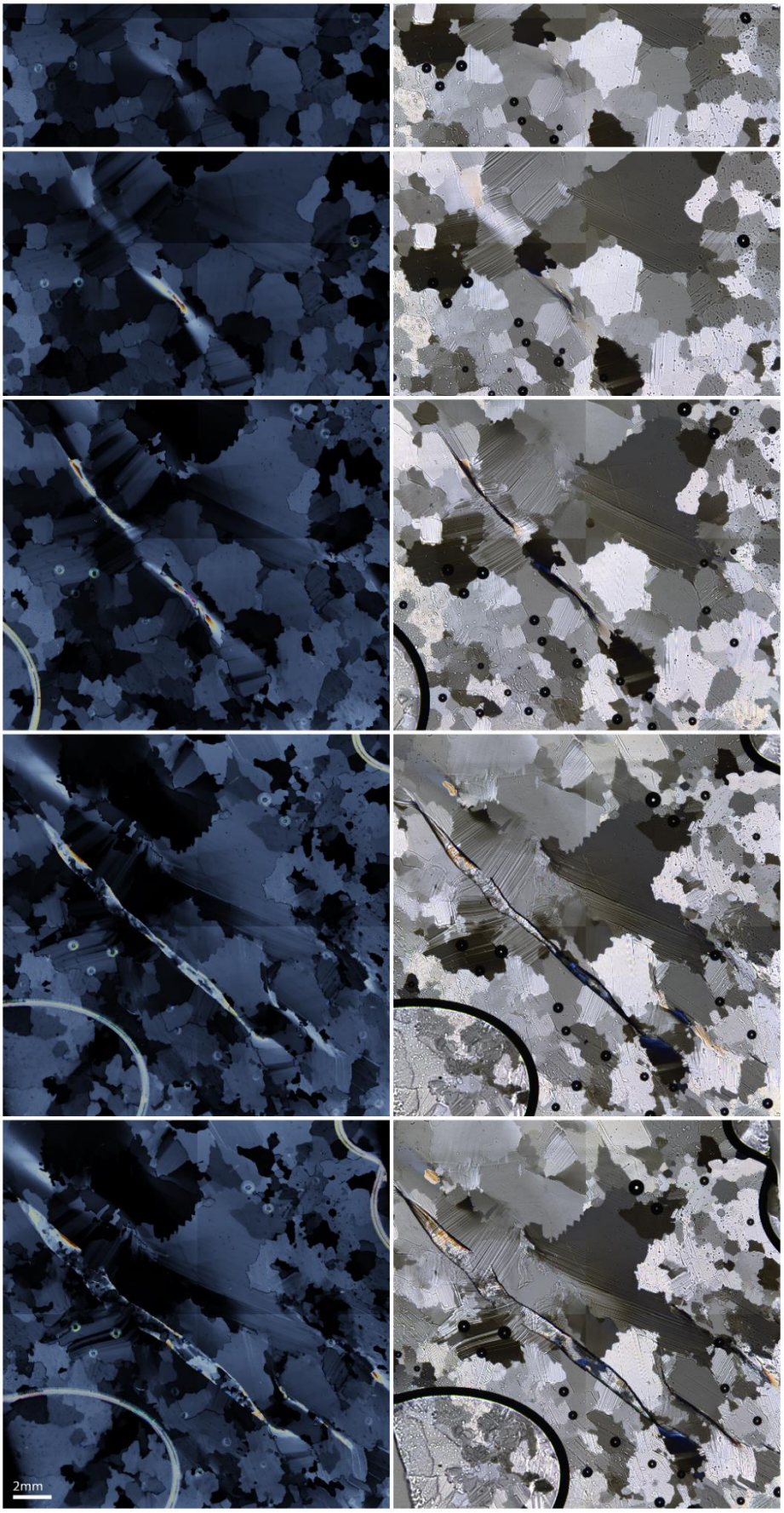

Figure 3.30: Retardation image (left) and lambda image (right) of sample -10_08 at shear strains of 0.13, 0.16, 0.22, 0.33, 0.39 from top to bottom. The development of the brittle fractur and the refill with smaller grains as well as the step like shaped grain boundaries are displayed at different shear strains. The scale for all pictures is the same, only the shown area changes.

4. Discussion

To compare the experiments the different parameters are discussed separately and connections between them are drawn. Three of the polycrystalline samples are linked with the same strain rate and vary in temperature (-05_03) or contain a small amount of a second phase (-10_06). The additional polycrystalline sample was deformed with a strain rate one magnitude smaller (-10_02) but with a slightly different technique for the attachment of the fiber.

The natural ice samples are either linked with the same strain rate (IL_-10_01 to IL_-5_03; IL_-10_02 to IL_-5_01) or the same temperature (as seen in the sample name). The two fast-deformed natural samples experienced the same strain rate as the fast polycrystalline samples.

The deformation apparatus used does not require any pure shear component as in many other experimental setups. Such as 2D experiments with blades pushing from the sides. Or in the 3D case where ice samples are pushed with diagonal cur pistons or sheared in torsion. A variety of possibilities to induce shear deformation are described in many studies. For all of them the findings on the behavior microstructures are conform. To validate the method used in this study the results are compared to a selection of other studies.

4.1 General observations

General observations like lobated grain boundaries, kinks and sub-grain structures were observed in all experiments. All of them indicate deformation and are described in other studies using simple shear deformation (e.g. Wilson & Zhang, 1994; Qi *et al.*, 2019; Fan *et al.*, 2020).

A connection between temperature and manifestation of lobated grain boundaries is described for example by Qi *et al.* (2019) or Fan *et al.* (2020). Higher temperatures lead to more and more strongly lobated grain boundaries due to the higher mobility rate of the grain boundaries (Nasello *et al.*, 2005). This behavior is also described in Wilson & Zhang, 1994) and explained by extensive grain-boundary migration in addition to the intracrystalline slip. This bulging of the boundaries follows high dislocation densities (Wusatowska-Sarnek *et al.*, 2002; Steinbach *et al.*, 2017).

The temperature relation for lobated grain boundaries can also be seen in the experiments from this study. For the natural ice samples as well as for the polycrystalline samples. Grain boundaries in the warm experiments (-5_03, IL_05_01 and IL_-5_03, Figure 3.1) tend to migrate and form lobate boundaries while in the cold experiments (-

10_06, -10_08, IL_-10_01, IL_-10_02, Figure 3.1) this mechanism is less dominant. There, a higher number of smaller grains develop, especially along the former grain boundaries, instead of grain boundary migration. The cold and slow deformed sample -10_02 also shows more lobated grain boundaries instead of small newly grown grains, indicating that the lobation of the boundaries is a function of strain rate in addition to temperature.

Deformation features in grains such as kinks and sub-grain formation are seen best in the natural samples (Figure 3.1). Here dislocations cannot 'escape' towards a grain boundary as easy as in smaller grains. This leads to a cumulation of dislocations forming a plane in the lattice with a high dislocation density, which is referred to a subgrain boundary. A dependence on the <c>-axes orientation for formation of these features can be observed in the polycrystalline samples. Depending on their <c>-axis orientation kinks and sub-grains develop earlier or later during deformation. The two sets of kink bands seen in the samples represent two different mechanisms. The first set, which can be seen in all experiments is due to the dislocation movement in the basal plane leading to a shift of these planes relative to each other. The kinks we see there are always perpendicular to the grain c-axis. The second set forms with increasing shear deformation due to buckling of the planes and occurs in grains oblique to the main shortening direction (Wilson *et al.*, 1986; Wang *et al.*, 2019).

Both features, lobated grain boundaries and kink bands, are also described for experiments done by e.g. Wilson & Zhang (1994) or Qi *et al.* (2019) in 3D experiments.

4.1.1 Grain size

The final grain size is expected to depend only on the strain rate (Passchier & Trouw, 2014). Following this all fast experiments (-10_08, -5_03, IL-10_01, IL_-5_03) should reach the same final grain size. Both fast deformed natural samples end at the same mean grain size, sample IL_-5_03 even reaches a stable grain size at a shear strain of around 0.29 (final shear strain 0.38). The natural sample deformed fast at -10° (IL_-10_01) did not reach a stable grain size at the end of deformation but reached a higher final shear strain (0.56). This is due to the lower mobility rate of the dislocations at colder temperatures (Duval *et al.*, 1983; Noguchi *et al.*, 2016) leading to a longer response time to reach the same state as the warmer deformed sample. In the polycrystalline fast deformed samples final grain sizes are smaller, but in both cases (-10_08, -5_03) no stable grain size was reached at the end of the deformation. It is therefore expected that grains in -5_03 would grow further during continuation of the deformation. The decrease in grain size for sample -10_08 can be explained by the shear fractures that appear in an early stage of deformation an immediately are filled with small grains. The "dirty" sample needs to be seen separately because particles/small air bubbles decrease the growth rate of the grains resulting in smaller grain sizes. This observation fits with modeled data from

Roessiger *et al.* (2014) that shows the limiting effects for boundary migration. Also strain localization along particles/bubbles increases fabric changes locally (Steinbach *et al.*, 2016) leading to visible shear bands, which can be seen in Figure 3.4 B inside the red marked area. Even though the amount of impurities in this sample is much smaller than the natural mass fraction of 10-6-10-8 (Cuffey & Paterson, 2010) effects are clear to see.

The initial stable phase for the mean grain sizes can be seen in all experiments (Figure 3.2) except for -10_08. This stable phase is longer in the in slower deformed samples and even more prominent to see in the natural samples. This longer response time before mechanisms start to change the mean grain size is due to the minimum amount of energy needed to activate deformation.

The mean grain size decrease of 40µm in sample -10_02 between strains of 0.1 and 0.15 aligns with the time the electrical socket broke and therefore the sliders did not move. While the sliders stopped, an initiation of annealing would be expected, but for this time only few images are available. The missing timesteps were filled with copies of the images before and after the lost ones. By comparing the images before and after the image loss (appendix), no significant changes are visible. Therefore, the decrease must be a result of the adjustment of the captured area after the restart bringing the smaller grains into the field of view.

4.1.2 Fabric

The polycrystalline samples all show a random <c>-axis distribution in the beginning and a clear change towards an angle of about 45° from the deformation direction. This pattern is clearly seen even though only relatively small shear strains were achieved. Similar results can be seen in experiments with layered ice samples by Wilson *et al.* (2003) leading to a dominant maximum about 5° from the pole of the bulk shear plane and a second maximum at 45°. This change in fabric in managed by a dynamic recrystallization process. Driven by the initiation of a second slip system along the pyramidal planes with increasing stress (Wilson *et al.*, 2003).

Both orientations can be found in the experiments run for this study (Figure 3.17 and 3.4), even though comparable shear strains of at least 0.7 were only reached for two deformations (IL_-5_01 and IL_-10_02). But the maximum at 45° dominates throughout the experiments, only -10_06 and IL_-5_03 show a maximum close to 5° from north.

The natural ice samples show two or three main spots at the beginning representing the few visible grains (Figure 3.11). This dominant feature weakens during deformation and all samples show a change in CPO to one of the expected maxima orientations. And therefore, orienting the grains preferably in an easier to deform position.

Same findings in relation to the position of <c>-axis orientation maxima are for example described in Bouchez & Duval (1982), Llorens *et al.* (2016), Journaux *et al.* (2019) or Qi *et al.* (2019). A list of further studies for comparison is provided in Qi *et al.* (2019).

Strength of the developed CPO is decreasing with temperature. This can be clearly seen by comparing -10_08 to -5_03 (Figure 3.17). Even though shear strain in -10_08 is a little higher than in -5_03 the maxima are clearer developed. The same observation is described in Qi *et al.* (2019). The pattern is preserved during annealing time but gets more diffuse. This is the same behavior as described in Journaux *et al.* (2019).

4.1.3 Ternary path

The ternary path diagrams (Figure 3.12) show the main pattern of the <c>-axis orientation distribution. For the Polycrystalline samples it shows a random distribution at the beginning and changes to a more girdle and late point structure during deformation. This gives a clear indication that the <c>-axis orientation is aligning towards a preferred pattern.

Similar development is predicted in models by Llorens *et al.* (2016). They expect with a trend towards a mixed girdle/point pattern and with higher strains a strong development towards a point distribution. This evolution is related to the dynamic recrystallisation processes involved in the change of CPO.

As the natural samples contain only a small amount of grains and therefore have a clear oriented preference in their <c>-axis orientation they already start with a strong point pattern. As the pattern referring to a point, gridle or random distribution describes a polycrystalline system the findings are not applicable in this case. Trends in the evolution of the pattern for the natural samples therefore are directly linked to the <c>-axis orientation of new grown grains.

For experiments IL_-10_02 and IL_-5_03 almost no changes are seen. In both cases the grains start with shallow dipping <c>-axis and no big changes are needed as they reach a favored orientation. Also, only few grains grow during deformation, all of them along the former grain boundaries. The other two experiments (IL_-10_01 and IL_-5_01) with natural ice start with steep dipping <c>-axis in the grains and have a much bigger amount of new grains by splitting the big start grains.

4.1.4 Shape-preferred orientation (SPO)

The weak developed Shape-preferred orientation that is seen in sample -5_03 (Figure 3.14) is also described by Qi *et al.* (2019) for samples deformed at -5°C with shear strain

rates of $7.98x10^{-5}$ to $17.8x10^{-5}$ 1/s. While Journaux *et al.* (2019) describes a strong elongated grain-shape fabric towards the extension direction for deformation experiment at -7°C with shear strain rates between $1.6x10^{-7}$ to $2.1x10^{-6}$ 1/s. Shear strain rates for the here presented study are faster and deformation temperature is colder (-10°C), still the development of an SPO in the colder samples is slightly stronger with a tendency towards 120°. Both studies reached comparable shear strain rates to this study. A stronger SPO developed in the dirty sample -10_06 due to the shear bands (Figure 3.4 B, red marked area).

The wide scattering of the data points for sample -5_03 (Figure 3.14) shows that no clear SPO developed during deformation. This pattern occurs as the grain detection from FAME software can vary a few pixels between the timesteps, as it determines grains by their <c>-axes measurement for each pixel. Therefore, the exact shape of the detected grain can vary in each direction within 1-2 pixels. For grains with no or weak SPO this variation leads to a change in the elongation direction of the ellipse fitted by FAME, as these ellipses are close to a circle. With no clear preference in elongation the calculated mean shows a wide distribution.

Natural samples contain only 2-3 grains in the beginning and the visible area of the grain often is elongated along a specific direction. New grains impact the development of the SPO as the mean is calculated by taking one orientation per grain. For IL_-10_01 many subgrain boundaries formed parallel to the main extension direction leading to elongated grains at the end of deformation. In sample IL_-5_03 elongated grains develop along the former grain boundaries also subgrain boundaries develop. Both natural samples deformed with an intermediate strain rate (IL_-10_02, IL_-5_01) show a wider scattering between data points for neighboring timesteps. This is due to the growth of small grains with no SPO along the former grain boundaries in IL_-10_02. The strong lobated grain boundary in IL_-5_01 in addition to new grains with no clear trend in SPO lead to a less dominant trend throughout deformation.

4.2 Grain boundaries

To discuss the behavior of grain boundaries during deformation the angular relations between <c>-axis and grains boundary are discussed individually and as combination of the angular relation for both neighboring grains to the grain boundary pole. As the planes are described by the normal vector of the plane it is more comfortable to use the angle to the grain boundary pole for descriptions. All angles used for further description are between grain <c>-axis and grain boundary pole if not mentioned otherwise.

4.2.1 Single grain boundaries (natural ice) vs. polycrystalline systems

The natural ice samples contain only few grain boundaries. They can therefore be described as a specific combinations of boundary conditions which could be found along with others in the polycrystalline ice. To follow this idea the specific combinations of angles between <c>-axis and grain boundary pole found in IL_-10_01 and IL_-10_02 were determined and same angle relations were picked from sample -10_08 to compare the behavior in a polycrystalline system. For IL_-10_01 two areas are given by a first maxima in the triangle density plots with angles between 80-90° on one side and 62-66° on the other and a second maxima with 80-90° on one side and angles between 40-50° on the other side of the boundary (Figure 3.24). In the range between 40-50° four possible crystal faces can be found but only three of them were possible to trace in the sample -10_08 for comparison. These three faces are $\{01\bar{1}1\}$,$\{11\bar{2}1\}$ and $\{10\bar{1}1\}$ with angles between grain <c>-axis and grain boundary pole of 41°, 46.8° and 48.6°. Individual segments connected to the two maxima in IL_-10_01 could not be followed separately throughout the deformation. Therefore, the selected segments from -10_08 are compared as a bulk behavior from all picked segments to the bulk behavior of IL_-10_01. A comparison with all selected segments in -10_08 for both maxima areas from IL_-10_01 is shown in Figure 3.17. In both cases it seems to be preferable to have at least one of the angles close to 90° while the other angle is distributed over the whole possible range. Looking in detail at the behavior for each angle combination selected in -10_08 (Figure 3.18), the combination $\{10\bar{1}1\} - \{\bar{1}0\bar{1}0\}$ (48.6° to 90°) shows the most difference to the bulk behavior of IL_-10_01. Without segments selected by this angle combination, the bulk behavior for the angle combinations picked from -10_08 shows a comparable pattern after deformation (Figure 4.1).

As the three chosen angle combinations in the range between 40-50° for one side of the grain boundary were dependent on the position of the maxima in the starting distribution of IL_-10_01, the possibility that one of these options is less strong in the natural sample must be taken into account. Also segments in IL_-10_01 that were not within the angle range that used to select the boundaries from -10_08 were not sorted out. Because these areas could not be followed during deformation with enough certainty. Therefore, it can be assumed that the bulk behavior of the angle combinations determined by IL_-10_01 is the same for comparable situations in a polycrystalline sample.

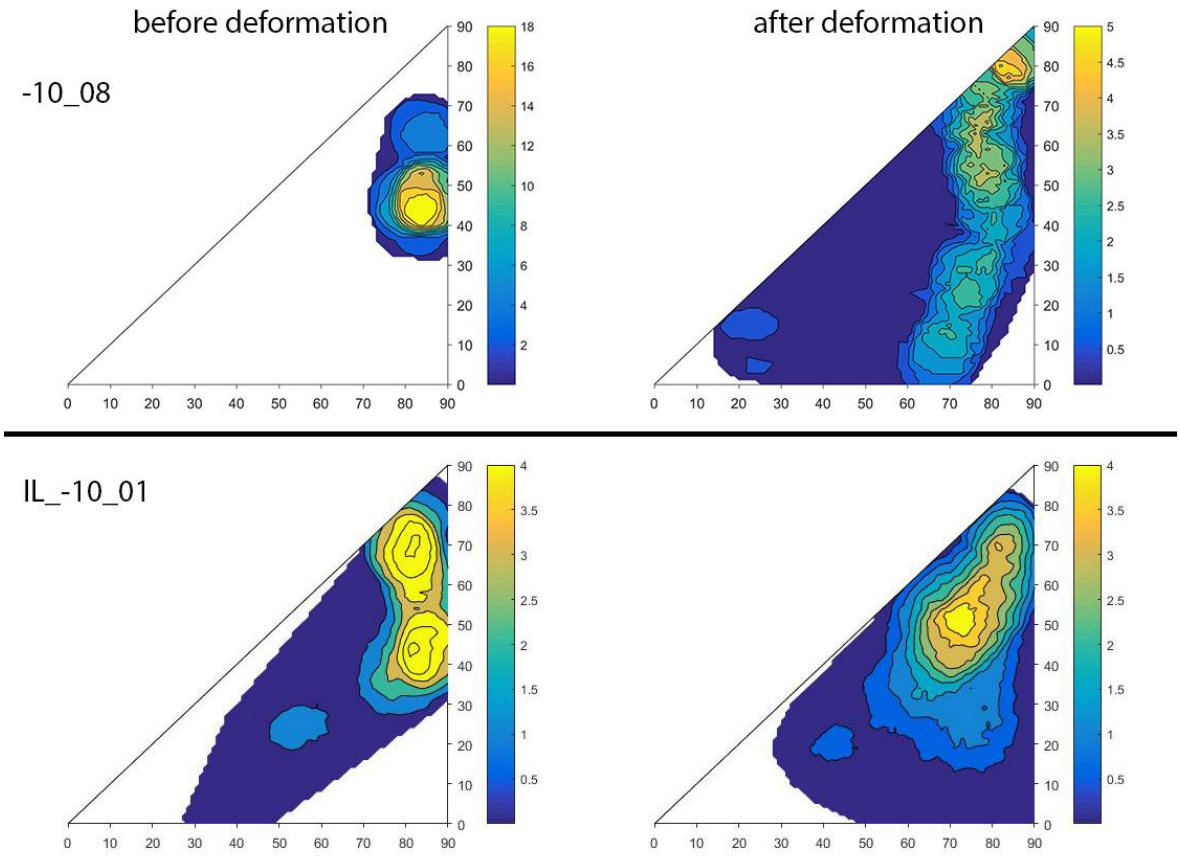

Figure 4.1: Comparison of the bulk behavior of angle combinations between grain <c>-axis and grain boundary pole for IL_-10_01 (bottom) with all selected segments within the comparable range from -10_08 (top).

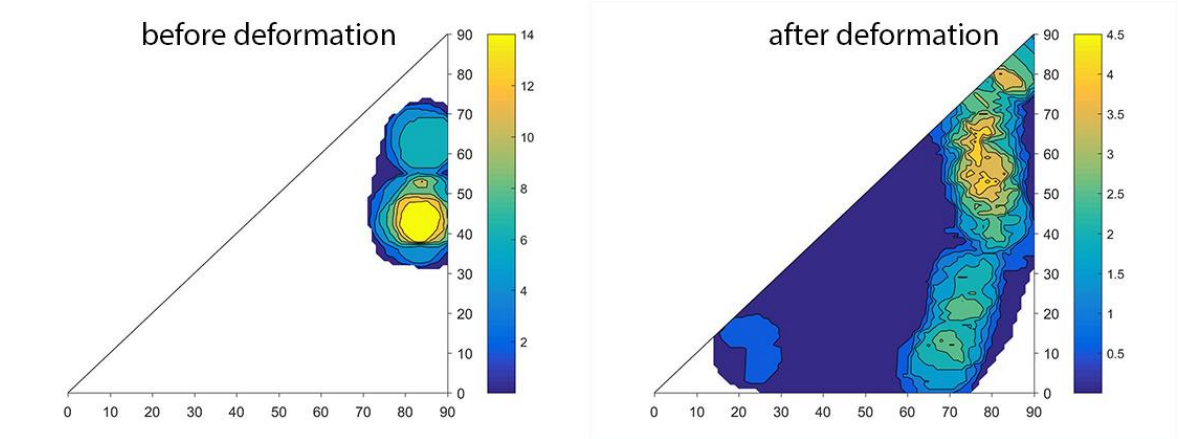

Figure 4.2: Bulk behavior of angle combinations between grain <c>-axis and grain boundary pole for selected segments from -10_08 without $\{10\bar{1}1\} - \{\bar{1}0\bar{1}0\}$ *combination.*

The comparison between IL_-10_02 and the suitable grain boundary segments from -10_08 contains one angle combination suitable for the crystal faces $\{\bar{1}\bar{1}22\}$ and $\{10\bar{1}2\}$ related to angles 19.3° and 28° between grain <c>-axis and grain boundary pole. For comparison, segments with angles in the range of 15-25° for one side and 25-31° for the other side of the grain boundary were selected from -10_08. Comparing the behaviour of the angular relations in IL_-10_02 and the selected segments from -10_08, the plots look similar (see Figure 3.18). The similar behaviour of the grain boundaries indicates, like for the comparison from IL_-10_01 with -10_08, that the natural samples can be seen as 'close-up pictures' showing specific starting situations and same behaviour during deforamtion as in poleycrystaline systems. In contrast to IL_-10_01 only one angle combination is present in IL_-10_02. Therefore the amount and range of segments outside the picked angle ranges is smaller as in IL_-10_01. This leads to a more similar looking behaviour in the plots.

Still this assumption to have the natural samples as close up pictures needs to be considered carefully. The number of segments that could be detected before and after deformation with certainty is low, in general less than 50 data points for each combination. The given comparison therefore indicates that the situation found in the natural samples can be seen as close up pictures which shows the same behavior in a polycrystalline sample. This gives the opportunity to study different starting situations in detail, but to strengthen the statistics more experiments are needed.

4.2.2 Grain boundary relation to both neighboring grains

As the angle between <c>-axis and grain boundary is directly linked to the crystal face represented by that angle, the combination of the angular relations of both neighboring grains to the boundary gives an indication of the crystal face combination that forms the boundary. Looking at the triangle density plots preferred orientation combinations are represented by maxima. The artificial samples with their polycrystalline pattern show a wide range of angle combinations in the beginning. The maximum densities are small, and therefore areas with a maximum are only slightly above average. Keep in mind that the shown density distributions are corrected with the normal distribution and therefore peaks represent the amount above the normal distribution. The statistical higher change to have a prism plane (90°), as there are six in a perfect crystal, is considered due to the correction by subtracting the normal distribution as explained earlier. Areas close to all three boundaries of the diagram suffer from a boundary effect, as areas close to these edges get less dense the closer they are to the edge. This effect derives from the way density plots are calculated and can be misleading as maxima will never reach the outlines (0°, 90° on one side, same angle on both sides).

Samples deformed at -10°C show a wide distribution of angle combinations after deformation. A slight trend to keeping at least one side close to an angle of 90° can be seen. While the other side tends towards smaller angles in the range of 20-30°. The very slow deformed sample -10_02 also develops a second maximum for an angle combination of around 20° to 40°. All the maxima develop around the angles related to certain crystal faces (see table 3-3).

At a temperature of -5°C and the same strain rate as -10_08 of $2.5x10^{-6}$ 1/s, the distribution after deformation shows wide distribution over a large range of angle combinations without a main preference. Even though the maxima are very weak three angle combination ranges can be distinguished. These are around 40° and 80°, 10° and 70-80°, and 30° and 50°. The tendency to have at least one side close to 90° is less strong developed here. During annealing the distribution even changes towards smaller angles with a tendency to have similar angles on both sides of the boundary. These angle ranges appear in the very slow (-10_02, strain rate of $2.5x10^{-7}$ 1/s) or warm (-5_03, -5°C) deformed sample. This indicates a possible correlation between the development of grain boundaries with pole angles around 20-30° (faces $\{\bar{1}\bar{1}22\}$ and $\{10\bar{1}2\}$) and warm and/or slow deformation. Looking at the natural samples, this trend can be seen in IL_-10_02 (slow deformed) and IL_-5_03 (warm deformed). In both cases the starting position is already close to the range of 20-30° for both sides of the grain boundary and stays there during deformation. This range of angle combinations seems to be quite stable and probably has a deep energetic sink at this position. In addition, as it seems this area is preferably reached during warm and/or slow deformation. The higher mobility of water molecules and dislocations in a warm setting can help to rearrange the molecules at the grain surface. And during a slow deformation the crystal lattice has more time to react to the applied stress and to adjust. The increased time to respond offers more possibilities for dislocation movement in the lattice.
However, the only sample deformed warm and slow IL_-5_01 (-5°C, $2.5x10^{-6}$ 1/s), and therefore combining the two factors possibly relevant to reach the faces $\{\bar{1}\bar{1}22\}$ and $\{10\bar{1}2\}$ for both sides of the boundary, does not show a clear development in this direction. The starting position has angles of 80-90° on one side and 60-70° on the other. A possible explanation is the orientation of the grain <c>-axis towards the deformation direction. The <c>-axis of the grain in IL_-5_01 (see Figure 3.11: smaller grain is the small spot in the center) is dipping steep while in IL_-10_02 and IL_-5_03 it is dipping shallower. As the <c>-axis is perpendicular to the three a-axis and located in the basal plane, the orientation of the <c>-axis gives also the orientation of the basal plane. For a steep dipping <c>-axis the basal plane is subparallel to the thin section plane. And therefore, the deformation direction is subparallel to the basal plane. With this starting setup a rearrangement of the crystal lattice that leads to a reorientation of the <c>-axis is hard to achieve (enhanced due to glass dependent slip). To reorientate the <c>-axis a tilt of the basal planes is necessary. The dislocation glide on the basal plane is energetically favored compared to any other glide direction. This energetic favored glide on the basal plane and its orientation relative to the deformation direction favors dislocation movement in the basal planes. But movement of dislocations across basal planes is necessary to tilt the basal plane. Thus, the steeply dipping <c>-axis of the grain in IL_-5_01 might be the reason that the lattice is more or less stuck in the starting position. The shallower angles

in IL_-10_02 and IL_-5_03 lead to a bigger angle between the basal plane of the grain deformation direction. This geometrical setup improves the possibility for dislocation movement across basal planes and therefore an easier setup to reorient the <c>-axis.

For sample -10_06, which contains a small number of particles, the starting conditions are slightly different. The distribution of angle combinations already shows a wide distribution with a weak main region in the range of 30-60° on one side and 50-80 on the other side. The distribution differs from the expected for a fully random starting material, but this can be explained by pinning effects. These disturb the rearrangement of grain boundaries during the annealing time in the sample preparation process. The effect is also visible in the lambda images (Figure 3.4 A) as the boundary traces are more irregular compared to the other polycrystalline samples. Annealing time and temperature during the sample preparation process were the same for all polycrystalline samples.

The pattern for the angle combination distribution after deformation follows the trend that can be seen in -10_08, which was deformed with same temperature and strain rate. The grain boundaries tend towards an angle combination with at least one side close to 90°. The other side of the boundary arranges mostly between 40-50°. To verify a general trend for the effect of impurities more experiments are needed.

Combinations with both angles towards 90° are underneath the normal distribution in all experiments. This combination seems to be less profitable or hard to archive during deformation.

To summarize, the development of the combined angle relation seems to depend on temperature, strain rate and possibly orientation of the <c>-axis towards the stress direction. As the natural samples show a close-up picture this is a chance to see in detail on how these three dependencies are related. But more experiments with variation of each of them independently are necessary. Especially the effect of the orientation vanishes in the bulk distribution of the polycrystalline samples, it seems to have the least strong influence of the three factors. Picking boundaries from the polycrystalline samples while taking all three into account leads to datasets with one or no segment. More deformations in polycrystalline samples are necessary to get a valid dataset out of it.

No dependence on the reached final shear strain was detected. The comparison between IL_-10_02 and -10_08 (Figure 3.18) has same temperature and strain rate but with 0.76 and 0.45 different shar strains, still they show the same behavior for the combined angle development.

4.2.3 Grain boundary relation to one neighbour / crystal faces

Looking on the distribution of angles between grain <c>-axes and grain boundary poles as single data points, without the combination to the angle on the other side of the

boundary, information is visualised in histogram plots. These were corrected with the normal distribution for the abundace of angles in a perfect crystal.

A general trend can be seen in the plots with the mean values for angle and frequency (Figure 3.21). For the angle and the related frequency the mean value of the overall dirstribution was taken. The decrease in frequency indicates a wider distribution of the angles as the data for plotting the histograms is normalized to the number of datapoints for each experiment and thereore reflects a percentage of grain bounaries with this anlge. There is no preference towards a specific angle in relation to temperature, strain rate or shear strain. This reflects what was seen in the triangle density plots, where at least one side of the boundary was distributed over the whole range of angles in the polycrystalline samples. Even though the natural samples start with a narrow distribution, reflected by the higher frequencies, the distribution after deformation is spread over a wider range of angles. All deformation experiments show the same trend towards a wider distribution of angles after deformation compared to before. No relation to temperature, strain or strain rate can be drawn.

Therefore it is necessary to have a closer look on individual changes in relation to preferred angles between the grain boundary pole and <c>-axis. In an attempt to create a way for easy comparison of different experiments by showing all data in one figure, all maxima for a fitted curve to the distribution of angle were determined. As the maxima are taken from a fitted plot, the position does not perfectly match with the angles for specific crystal faces. This effect gets bigger on both ends of the angle range, towards 0° and 90°, due to the fitting method. Also maxima close to each other shift the postion of the maxima towards the maximum with a higher frequency. Still the best results were gained form the kernel-fit method used.

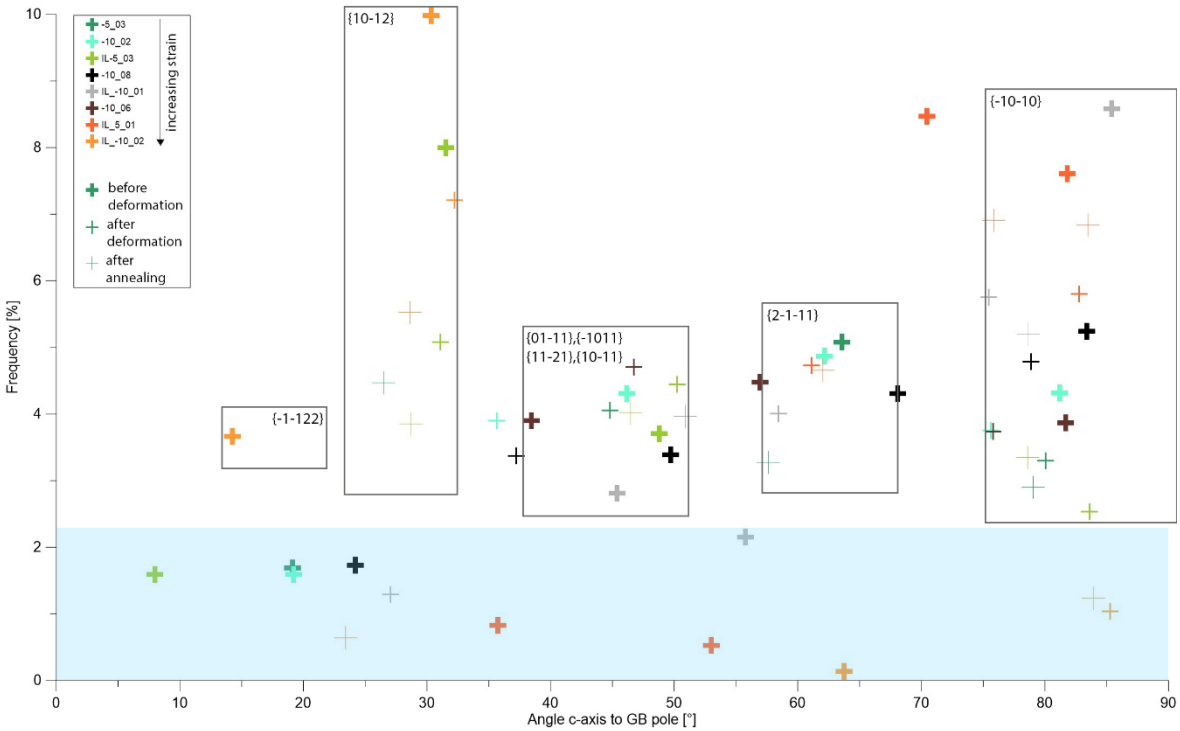

Figure 4.3: The relative abundance of angles between <c>-axis and grain boundary pole for each maximum of the fitted plots. Squares indicating to which crystal faces data points are related. Data points in the blue area are underneath minimum frequency for relevance.

Low frequency maxima (Figure 4.3) are less significant and mainly related to minor variations in regions with less data points. The minimum frequency for consideration is set to 2.2. These maxima can be mathematically derived from the fit curve but are not significantly higher than their surrounding and are weak in the overall comparison.

The two points for -10_02 and -10_08 after deformation (Figure 4.3), close to 35°, are an example for the shift that can happen due to the fitting method. Both of them are closer to the $\{10\bar{1}2\}$ field when looking at the histogramm plots (appendix). Point related to artificial samples plot at similar heights. This means the peaks are all equal and no preferred angles are visible in the starting material. Other for the natural samples as the high frequencies of the maxima represent the prefered orientation in these close up images of grain boundaries.

The remaining maxima can be sorted into five clusters, all of which are related to specific crystal faces. Grey rectangles in Figure 4.3 indicate to which crystal face the maxima are related to. The four crystal faces with angles ranging between 40-50° are grouped together as they are too close to be sorted separately. A sixth group would be close to 0° but no significant maximum was derived for this region within the measured data.

The maximum in IL_-5_01 at 70° stands out, as it does not fit into one of the specified fields around angles related to crystal faces. As it is a natural ice sample with an unknown

history, possible reasons are hard to determine. But nonetheless during deformation the main peaks of angles arranges within a field related to a crystal face. Although all angles between grain <c>-axis and grain boundary pole are possible, they arrange mainly towards angles related to crystal faces. During deformation, the maxima either stay in one field or change to the closest one. Large changes in the angular relation are detected. Thus, to describe the behavior of individual grain boundaries additional to temperature, strain rate and orientation, as discussed earlier, the starting angle between <c>-axis and grain boundary is relevant.

4.2.4 Grain boundary dip angles

Dip angles of the grain boundaries in the starting material are mainly steep. The arrangement cannot be influenced and is taken as given. Independent of temperature, strain or strain rate, all grain boundaries in this study develop towards a similar dip angle. Not only for polycrystalline bulk behavior but also individual grain boundaries like in the natural samples follow this trend.

The <c>-axis orients towards 45° to the stress direction. Grain boundaries tend to get shallower. This information looked at from a pure geometrical point of few would lead eventually to only grain boundaries parallel to the <c>-axis. Therefore, only prism faces would be left. But we see a trend towards the other end of the angle range especially for warm and/or slow deformations.

Orientations of crystal faces are related to the crystal lattice as they are planes in the lattice with the most stable arrangements of molecules. The surface energy for each plane is different and related to many factors mostly influences by the pattern of the molecules on the plane. The pattern for the oxygen arrangement is repetitive within a plane. But the distribution of the hydrogen is random (Pauling, 1935). Therefore, on a crystal surface the distribution of bonded hydrogens and free electron pairs from the oxygens pointing out of the surface have no repetitive pattern. This is the reason for the uneven electron density distribution on the surface. As each crystal face is related to an energetic sink, the uneven distribution of electron density may lead to local variations within the sink. Adding any type of dislocation on these surfaces can increase these variations. Each crystal face is related to a certain energy level. Transition between them needs activation in form of energy in some kind. The local variations on the crystal face might increase or decrease the needed amount.

This energy distribution stabilizing certain arrangements in the lattice has probably more influence on the final situation than pure geometry.

4.3 Shear fractures and step-like grain boundary traces

Some samples feature a brittle fracture opening along the extensional region. These can be seen in an early stage in the retardation images as they thicken before they break. The most interesting part is that after they break up, both sides of the fracture overlap and immediately smaller grains grow inside (see Figure 3.23). This type of fracturing was only found in the polycrystalline samples. Although it was best observed in -10_08, the initiation was also observed in the slower deformed sample -10_02. To clarify if there is a temperature relation after which these fractures do not occur, further experiments are needed to make sure not only higher stresses would have been necessary.

The step-like grain boundary traces need a combination of two conditions to develop. First the strike of the grain boundary needs to be within the range of 68-72°. Second difference in the hard/soft criteria between the two grains on both sides of the boundary needs to be high (>0.4). The second condition includes a shallow dipping <c>-axis. This specific geometrical relation of grain boundary, <c>-axis and stress direction might be an indication for reconstruction of deformation directions in unknown samples. To verify the possibility of this method bigger data sets are necessary and an additional examination for application in 3D samples.

5. Conclusion

Several simple shear deformations were done with varying temperature and strain rate. The material used were artificial polycrystalline samples and natural ice with large grains and few grain boundaries.

1. General validity of deformation apparatus

It is shown that the method used to induce a simple shear deformation on ice thin sections leads to results comparable to other used methods in 2D with blades or 3D with friction or torsion. The results for the general behavior in grain size, shape and fabric represent the expected behavior for a simple shear deformation. The apparatus therefore is a valid method to induce shear deformation and observe microstructures in situ.

2. Close up pictures on grain boundaries in natural samples

The natural ice samples contain only few grain boundaries and represent individual starting conditions in terms of the orientation of the grains, the grain boundary and type of the boundary plane for each of the neighboring grains. As those specific situations can also be found in the polycrystalline samples and the behavior of the grain boundaries is the same, these samples provide us with a tool to individually study specific arrangements.

3. Preferred angle combinations and their stability

Angle combinations with at least one side close to 90° after deformation occur often. For warm and/or slow deformation a combination of $\{\bar{1}\bar{1}22\}$ and $\{10\bar{1}2\}$ is favored.

4. Change in total occurrence of certain angles

Although all angles between grain <c>-axis and grain boundary pole are possible, they arrange mainly towards angles related to crystal faces.

5. Relation between angles of grain boundary pole to <c>-axis, deformation direction and dip angle

The type of crystal face that forms the grain boundary and their geometrical relation toward the deformation direction have the largest influence on the boundary development during deformation. For certain faces, such as $\{\bar{1}\bar{1}22\}$ and $\{10\bar{1}2\}$, energetic stabilization overprints geometrical favoritism.

6. Brittle fractures and regrowth of small grains

The occurrence of brittle fracture within the applied strain rates might be temperature dependent, as these were only observed in samples deformed at -10°C but not depending on the strain rate.

Outlook

To deeper investigate the findings of this thesis more deformation experiments with natural ice samples as well as with artificial polycrystalline samples are needed. Completing the set especially for the polycrystalline samples with intermediate strain rates for both temperatures would be appreciated. As well as a wider variety in temperatures and strain rates can help to clear the picture.

The influence of particles needs further investigation, and to try different shapes of particles might be interesting. Dirty natural samples with largen grains would provide a good opportunity to study the effects in detail.

In all cases several repetitions of the deformations are needed to strengthen the statistics and secure the suggested interpretation.

Another field of interest can be to better understand and follow the heat transport pattern in shear zones. Transport paths are influenced by dislocations and disturbed by grain boundaries. The changes in the crystal lattice and the change in orientation and type of grain boundaries during the shear deformation probably influences heat transport. Induced heat in the system can lead to changes in behavior such as weaken the material in located areas and thus making deformation in these areas easier.

The steplike grain boundary pattern showed a strong dependency on the orientation of the deformation direction to the strike of the grain boundary and the <c>-axis

orientation. This information might be used to reconstruct former stress directions. Therefore, a deeper investigation of this structure is needed to make the step from the 2D observation to a 3D picture and observe the changes during annealing after a deformation.

Acknowledgement

I want to say a big thank you to my supervisor Mark Peternell for always listening and helping with all difficulties during this time, for giving support whenever needed, for making working on this thesis real fun and for coming up with the idea to do my thesis work during an exchange in the first place. I am thankful for all the experiences I was able to make.

A thank you goes to Eric Sturkell for picking a really nice piece of ice from the Vatnajökull glacier and the really interesting story about how to get it to Göteborg.

I also want to say thank you to Sofia Böhme for increasing my productivity during the writing process, managing my time plan, and making sure to stick to it. Also, for encouraging me when needed and cheering me up whenever necessary.

List of figures

List of tables

References

Alley, R.B., Perepezko, J.H., and Bentley, C.R., 1986, Grain growth in polar ice: I. Theory: Journal of Glaciology, v. 32, no. 112, p. 415–424.

Alley, R.B., Perepezko, J.H., and Bentley, C.R., 1986, Grain growth in polar ice: II. Application: Journal of Glaciology, v. 32, no. 112, p. 425–433.

Alley, R.B., and Woods, G.A., 1996, Impurity influence on normal grain growth in the GISP2 ice core - Greenland: Journal of Glaciology, v. 42, no. 141, p. 255–260.

Ashby, M.F., and Duval, P., 1985, The creep of polycrystalline ice: Cold Regions Science and Technology, v. 11, no. 3, p. 285–300, doi: 10.1016/0165-232X(85)90052-7.

Bernal, J.D., and Fowler, R.H., 1933, A Theory of Water and Ionic Solution, with Particular Reference to Hydrogen and Hydroxyl Ions: The Journal of chemical physics, v. 1, no. 8, p. 515–548, doi: 10.1063/1.1749327.

Binnewies, M., Finze, M., Jäckel, M., Schmidt, P., Willner, H., and Rayner-Canham, G., 2016, Allgemeine und anorganische Chemie, 3., vollständig überarbeitete Auflage: Berlin, Springer Spektrum, Lehrbuch, 965 p.

Bons, P.D., Jansen, D., Mundel, F., Bauer, C.C., Binder, T., Eisen, O., Jessell, M.W., Llorens, M.-G., Steinbach, F., Steinhage, D., and Weikusat, I., 2016, Converging flow and anisotropy cause large-scale folding in Greenland's ice sheet: Nature communications, v. 7, p. 11427, doi: 10.1038/ncomms11427.

Bouchez, J.L., and Duval, P., 1982, The fabric of polycrystalline ice deformed in simple shear: experiments in torsion, natural deformation and gemetrical interpretation: Texture, Stress, and Microstructure, v. 5, no. 3, p. 171–190.

Bramwell, S.T., and Harris, M.J., 2020, The history of spin ice: Journal of Physics: Condensed Matter, v. 32, no. 37, p. 374010, doi: 10.1088/1361-648X/ab8423.

Bresser, J. de, Ter Heege, J., and Spiers, C., 2001, Grain size reduction by dynamic recrystallization: can it result in major rheological weakening?: International Journal of Earth Sciences, v. 90, no. 1, p. 28–45, doi: 10.1007/s005310000149.

Bresser, J.H.P. de, Peach, C.J., Reijs, J.P.J., and Spiers, C.J., On dynamic recrystallization during solid state flow: Effects of stress and temperature.

Chauve, T., Montagnat, M., Piazolo, S., Journaux, B., Wheeler, J., Barou, F., Mainprice, D., and Tommasi, A., 2017, Non-basal dislocations should be accounted for in simulating ice mass flow: Earth and Planetary Science Letters, v. 473, p. 247–255, doi: 10.1016/j.epsl.2017.06.020.

Chauve, T., Montagnat, M., and Vacher, P., 2015, Strain field evolution during dynamic recrystallization nucleation; A case study on ice: Acta Materialia, v. 101, p. 116–124, doi: 10.1016/j.actamat.2015.08.033.

Cheftel, J.C., Lévy, J., and Dumay, E., 2000, Pressure-assisted freezing and thawing: Principles and potential applications: Food Reviews International, v. 16, no. 4, p. 453–483, doi: 10.1081/FRI-100102319.

Cole, D.M., 1987, Strain-rate and grain-size effects in ice: Journal of Glaciology, v. 33, no. 115, p. 274–280.

Cottrell, A.H., 1953, Theory of dislocations: Progress in metal physics, v. 4, p. 205–264, doi: 10.1016/0502-8205(53)90018-5.

Craw, L., Qi, C., Prior, D.J., Goldsby, D.L., and Kim, D., 2018, Mechanics and microstructure of deformed natural anisotropic ice: Journal of Structural Geology, v. 115, p. 152–166, doi: 10.1016/j.jsg.2018.07.014.

Cuffey, K., and Paterson, W.S.B., 2010, The physics of glaciers, 4th ed.: Burlington MA, Butterworth-Heinemann/Elsevier, xii, 693.

Cyprych, D., Piazolo, S., Wilson, C.J.L., Luzin, V., and Prior, D.J., 2016, Rheology, microstructure and crystallographic preferred orientation of matrix containing a dispersed second phase: Insight from experimentally deformed ice: Earth and Planetary Science Letters, v. 449, p. 272–281, doi: 10.1016/j.epsl.2016.06.010.

Doherty, R.D., Hughes, D.A., Humphreys, F.J., Jonas, J.J., Jensen, D.J., Kassner, M.E., King, W.E., McNelley, T.R., McQueen, H.J., and Rollett, A.D., 1998, Current issues in recrystallization: A review: Materials Today, v. 1, no. 2, p. 14–15.

Durand, G., Weiss, J., Lipenkov, V., Barnola, J.M., Krinner, G., Parrenin, F., Delmonte, B., Ritz, C., Duval, P., Röthlisberger, R., and Bigler, M., 2006, Effect of impurities on grain growth in cold ice sheets: Journal of Geophysical Research, v. 111, F1, p. 597, doi: 10.1029/2005JF000320.

Duval, P., Ashby, M.F., and Anderman, I., 1983, Rate-controlling processes in the creep of polycrystalline ice: The Journal of Physical Chemistry, v. 87, no. 21, p. 4066–4074, doi: 10.1021/j100244a014.

Eichler, J., Kleitz, I., Bayer-Giraldi, M., Jansen, D., Kipfstuhl, S., Shigeyama, W., Weikusat, C., and Weikusat, I., 2017, Location and distribution of micro-inclusions in the EDML and NEEM ice cores using optical microscopy and in situ Raman spectroscopy: The Cryosphere, v. 11, no. 3, p. 1075–1090, doi: 10.5194/tc-11-1075-2017.

Fan, S., Hager, T., Prior, D.J., Cross, A.J., Goldsby, D.L., Qi, C., Negrini, M., and Wheeler, J., 2020, Temperature and strain controls on ice deformation mechanisms: insights from the microstructures of samples deformed to progressively higher strains at −10, −20 and −30 °C.

Faria, S.H., Weikusat, I., and Azuma, N., 2014, The microstructure of polar ice. Part I: Highlights from ice core research: Journal of Structural Geology, v. 61, p. 2–20, doi: 10.1016/j.jsg.2013.09.010.

Faria, S.H., Weikusat, I., and Azuma, N., 2014, The microstructure of polar ice. Part II: State of the art: Journal of Structural Geology, v. 61, p. 21–49, doi: 10.1016/j.jsg.2013.11.003.

Fennell, T., Deen, P.P., Wildes, A.R., Schmalzl, K., Prabhakaran, D., Boothroyd, A.T., Aldus, R.J., McMorrow, D.F., and Bramwell, S.T., 2009, Magnetic Coulomb Phase in the Spin Ice Ho2Ti2O7: Science, v. 326, no. 5951, p. 415–417, doi: 10.1126/science.1177582.

Fisher, D.A., and Koerner, R.M., 1986, On the special rheologiecal properties of ancient microparticle-laden northern hemisphere ice as derived from bore-hole and core measurements: Journal of Glaciology, v. 32, no. 112, p. 501–510.

Fossen, H., 2016, Structural geology, Second edition: Cambridge, Cambridge University Press, 510 p.

Goldsby, D.L., and Kohlstedt, D.L., 2001, Superplastic deformation of ice: Experimental observations: Journal of Geophysical Research, v. 106, B6, p. 11017–11030, doi: 10.1029/2000JB900336.

Grennerat, F., Montagnat, M., Castelnau, O., Vacher, P., Moulinec, H., Suquet, P., and Duval, P., 2012, Experimental characterization of the intragranular strain field in columnar ice during transient creep: Acta Materialia, v. 60, no. 8, p. 3655–3666, doi: 10.1016/j.actamat.2012.03.025.

Hammes, D.M., and Peternell, M., 2016, FAME: Software for analysing rock microstructures: Computers & Geosciences, v. 90, p. 24–33, doi: 10.1016/j.cageo.2016.02.010.

Hammes, D.M., and Peternell, M., 2018, Reconstruction of 3D grain boundaries from rock thin sections, using an advanced polarised-light microscopy method: Journal of microscopy, v. 269, no. 1, p. 23–35, doi: 10.1111/jmi.12605.

Harris, M.J., Bramwell, S.T., McMorrow, D.F., Zeiske, T., and Godfrey, K.W., 1997, Geometrical Frustration in the Ferromagnetic Pyrochlore Ho2Ti2O7: Physical review letters, v. 79, no. 13, p. 2554–2557, doi: 10.1103/PhysRevLett.79.2554.

Haseloff, M., Hewitt, I.J., and Katz, R.F., 2019, Englacial Pore Water Localizes Shear in Temperate Ice Stream Margins: Journal of Geophysical Research: Earth Surface, v. 124, no. 11, p. 2521–2541, doi: 10.1029/2019JF005399.

Hock, R., Rasul, G., Adler, C., Cáceres, B., Gruber, S., Hirabayashi, Y., Jackson, M., Kääb, A., Kang, S., Kutuzov, S., Milner, A., Molau, U., Morin, S., Orlove, B., and Steltzer, H., 2019, High Mountain Areas.: IPCC Special Report on the Ocean and Cryosphere in a Changing Climate [H.-O. Pörtner, D.C. Roberts, V. Masson-Delmotte, P. Zhai, M. Tignor, E. Poloczanska, K. Mintenbeck, A. Alegría, M. Nicolai, A. Okem, J. Petzold, B. Rama, N.M. Weyer (eds.)].

Hondoh, T., 2000, Nature and behavior of dislocations in ice: Physics of ice core records, p. 3–14.

Hooke, R.L., 2020, Principles of glacier mechanics, Third edition, Cambridge University Press, 513 p.

Jacka, T.H., 1984, The time and strain required for development of minimum strain rates in ice: Cold Regions Science and Technology, v. 8, p. 261–268.

Journaux, B., Chauve, T., Montagnat, M., Tommasi, A., Barou, F., Mainprice, D., and Gest, L., 2019, Recrystallization processes, microstructure and crystallographic preferred orientation evolution in polycrystalline ice during high-temperature simple shear: The Cryosphere, v. 13, no. 5, p. 1495–1511, doi: 10.5194/tc-13-1495-2019.

Jun, L., Jacka, T.H., and Morgan, V., 1998, Crystal-size and microparticles record in the ice core from Dome Summit South, Law Dome, East Antarctica: Annals of glaciology, v. 27, p. 343–348.

Ketcham, W.M., and Hobbs, P.V., 1969, An experimental determination of the surface energies of ice: Philosophical Magazine, v. 19, no. 162, p. 1161–1173, doi: 10.1080/14786436908228641.

Kimizuka, H., Ogata, S., Li, J., and Shibutani, Y., 2007, Complete set of elastic constants of α -quartz at high pressure: A first-principles study: Physical Review B, v. 75, no. 5, doi: 10.1103/PhysRevB.75.054109.

Kruhl, J.H., and Peternell, M., 2002, The equilibriation of high-angle grain boundaries in dynamically recrystallized quartz: the effect of crystalloptaphy and temperature: Journal of Structural Geology, v. 24, p. 1125–1137.

La Chapelle, S. de, Castelnau, O., Lipenkov, V., and Duval, P., Dynamic recrystallization and texture development in ice as revealed by the study of deep ice cores in Antarctica and Greenland.

Li, J.C., Nield, V.M., Ross, D.K., Whitworth, R.W., Wilson, C.C., and Keen, D.A., 1994, Diffuse neutron-scattering study of deuterated ice Ih: Philosophical Magazine B, v. 69, no. 6, p. 1173–1181, doi: 10.1080/01418639408240187.

Lipenkov, V., Barkov, N.I., Duval, P., and Pimienta, P., 1989, Crystalline texture of the 2083m ice core at Vostok Station, Antarctica: Journal of Glaciology, v. 35, no. 121, p. 392–398.

Llorens, M.-G., Griera, A., Bons, P.D., Lebensohn, R.A., Evans, L.A., Jansen, D., and Weikusat, I., 2016, Full-field predictions of ice dynamic recrystallisation under simple shear conditions: Earth and Planetary Science Letters, v. 450, p. 233–242, doi: 10.1016/j.epsl.2016.06.045.

Meredith, M., Sommerkorn, M., Cassotta, S., Derksen, C., Ekaykin, A., Hollowed, A., Kofinas, G., Mackintosh, A., Melbourne-Thomas, J., Muelbert, M.M.C., Ottersen, G., Pritchard, H., and Schuur, E.A.G., 2019, Polar Regions: IPCC Special Report on the Ocean and Cryosphere in a Changing Climate [H.-O. Pörtner, D.C. Roberts, V. Masson-Delmotte, P. Zhai, M. Tignor, E. Poloczanska, K. Mintenbeck, A. Alegría, M. Nicolai, A. Okem, J. Petzold, B. Rama, N.M. Weyer (eds.)].

Middleton, C.A., Grindrod, P.M., and Sammonds, P.R., 2017, The effect of rock particles and D2O replacement on the flow behaviour of ice: Philosophical transactions. Series A, Mathematical, physical, and engineering sciences, v. 375, no. 2086, doi: 10.1098/rsta.2015.0349.

Montagnat, M., and Duval, P., 2004, Dislocations in Ice and Deformation Mechanisms: from Single Crystals to Polar Ice: Defect and Diffusion Forum, v. 229, 43-0, doi: 10.4028/www.scientific.net/DDF.229.43.

Morris, D.J.P., Tennant, D.A., Grigera, S.A., Klemke, B., Castelnovo, C., Moessner, R., Czternasty, C., Meissner, M., Rule, K.C., Hoffmann, J.-U., Kiefer, K., Gerischer, S., Slobinsky, D., and Perry, R.S., 2009, Dirac Strings and Magnetic Monopoles in the Spin Ice Dy2Ti2O7: Science, v. 326, no. 5951, p. 411–414, doi: 10.1126/science.1178868.

Murray, B.J., Knopf, D.A., and Bertram, A.K., 2005, The formation of cubic ice under conditions relevant to Earth's atmosphere: Nature, v. 434, no. 7030, p. 202–205, doi: 10.1038/nature03403.

Nada, H., and Furukawa, Y., 2005, Anisotropy in growth kinetics at interfaces between proton-disordered hexagonal ice and water: A molecular dynamics study using the six-site model of H2O: Journal of Crystal Growth, v. 283, 1-2, p. 242–256, doi: 10.1016/j.jcrysgro.2005.05.057.

Nada, H., van der Eerden, J.P., and Furukawa, Y., 2004, A clear observation of crystal growth of ice from water in a molecular dynamics simulation with a six-site potential model of H2O: Journal of Crystal Growth, v. 266, 1-3, p. 297–302, doi: 10.1016/j.jcrysgro.2004.02.058.

Nasello, O.B., Di Prinzio, C.L., and Guzmán, P.G., 2005, Temperature dependence of “pure” ice grain boundary mobility: Acta Materialia, v. 53, no. 18, p. 4863–4869, doi: 10.1016/j.actamat.2005.06.022.

Nishinaga, T., editor, 2015, Handbook of crystal growth, Second edition: Amsterdam, Elsevier, 1181 p.

Noguchi, N., Kubo, T., Durham, W.B., Kagi, H., and Shimizu, I., 2016, Self-diffusion of polycrystalline ice I h under confining pressure: Hydrogen isotope analysis using 2-D Raman imaging: Physics of the Earth and Planetary Interiors, v. 257, p. 40–47, doi: 10.1016/j.pepi.2016.05.010.

Passchier, C.W., and Trouw, R.A.J., 2014, Microtectonics, 2., rev. and enlarg. ed. 2005, repr: Berlin, Springer, 366 p.

Paterson, W.S.B., 1991, Why ice-age ice is sometimes "soft": Cold Regions Science and Technology, v. 20, p. 75–98.

Pauling, L., 1935, The Structure and Entropy of Ice and of Other Crystals with Some Randomness of Atomic Arrangement: Journal of the American Chemical Society, v. 57, no. 12, p. 2680–2684, doi: 10.1021/ja01315a102.

Peternell, M., Dierckx, M., Wilson, C.J.L., and Piazolo, S., 2014, Quantification of the microstructural evolution of polycrystalline fabrics using FAME: Application to in situ deformation of ice: Journal of Structural Geology, v. 61, p. 109–122, doi: 10.1016/j.jsg.2013.05.005.

Peternell, M., Hasalová, P., Wilson, C.J.L., Piazolo, S., and Schulmann, K., 2010, Evaluating quartz crystallographic preferred orientations and the role of deformation partitioning using EBSD and fabric analyser techniques: Journal of Structural Geology, v. 32, no. 6, p. 803–817, doi: 10.1016/j.jsg.2010.05.007.

Peternell, M., Kohlmann, F., Wilson, C.J.L., Seiler, C., and Gleadow, A.J.W., 2009, A new approach to crystallographic orientation measurement for apatite fission track analysis: Effects of crystal morphology and implications for automation: Chemical Geology, v. 265, 3-4, p. 527–539, doi: 10.1016/j.chemgeo.2009.05.021.

Peternell, M., and Wilson, C.J.L., 2016, Effect of strain rate cycling on microstructures and crystallographic preferred orientation during high-temperature creep: Geology, v. 44, no. 4, p. 279–282, doi: 10.1130/G37521.1.

Peternell, M., Wilson, C.J.L., and Hammes, D.M., 2019, Strain rate dependence for evolution of steady state grain sizes: Insights from high-strain experiments on ice: Earth and Planetary Science Letters, v. 506, p. 168–174, doi: 10.1016/j.epsl.2018.10.037.

Petrenko, V.F., and Whitworth, R.W., 2002, Physics of Ice, Oxford University Press, 408 p.

Piazolo, S., Wilson, C.J.L., Luzin, V., Brouzet, C., and Peternell, M., 2013, Dynamics of ice mass deformation: Linking processes to rheology, texture, and microstructure: Geochemistry, Geophysics, Geosystems, v. 14, no. 10, p. 4185–4194, doi: 10.1002/ggge.20246.

Prior, D.J., Chao, Q., Craw, L., Durham, W.B., Sheng, F., Golding, N., Goldsby, D.L., Seidemann, M., and Vaughan, M.J., 2018, The control of strain rate temperature and strain on the symmetry, shape and magnitude of anisotropy development during ice deformation: Geophysical Research Abstracts, v. 20, EGU2018-11349.

Prior, D.J., Lilly, K., Seidemann, M., Vaughan, M., Becroft, L., Easingwood, R., Diebold, S., Obbard, R., Daghlian, C., Baker, I., Caswell, T., Golding, N., Goldsby, D., Durham, W.B., Piazolo, S., and Wilson, C.J.L., 2015, Making EBSD on water ice routine: Journal of microscopy, v. 259, no. 3, p. 237–256, doi: 10.1111/jmi.12258.

Qi, C., Prior, D.J., Craw, L., Fan, S., Llorens, M.-G., Griera, A., Negrini, M., Bons, P.D., and Goldsby, D.L., 2019, Crystallographic preferred orientations of ice deformed in direct-shear experiments at low temperatures: The Cryosphere, v. 13, no. 1, p. 351–371, doi: 10.5194/tc-13-351-2019.

Ramirez, A.P., Hayashi, A., Cava, R.J., Siddharthan, R., and Shastry, B.S., 1999, Zero-point entropy in 'spin ice': Nature, v. 399, no. 6734, p. 333–335.

Roessiger, J., Bons, P.D., and Faria, S.H., 2014, Influence of bubbles on grain growth in ice: Journal of Structural Geology, v. 61, p. 123–132, doi: 10.1016/j.jsg.2012.11.003.

Saruya, T., Nakajima, K., Takata, M., Homma, T., Azuma, N., and Goto-Azuma, K., 2019, Effects of microparticles on deformation and microstructural evolution of fine-grained ice: Journal of Glaciology, v. 65, no. 252, p. 531–541, doi: 10.1017/jog.2019.29.

Schulson, E.M., and Duval, P., 2009, Creep and Fracture of Ice: Cambridge, Cambridge University Press.

Staroszczyk, R., 2019, Ice Mechanics for Geophysical and Civil Engineering Applications: Cham, Springer International Publishing, GeoPlanet, 334 p.

Steinbach, F., Bons, P.D., Griera, A., Jansen, D., Llorens, M.-G., Roessiger, J., and Weikusat, I., 2016, Strain localization and dynamic recrystallization in the ice–air aggregate: a numerical study: The Cryosphere, v. 10, no. 6, p. 3071–3089, doi: 10.5194/tc-10-3071-2016.

Steinbach, F., Kuiper, E.-J.N., Eichler, J., Bons, P.D., Drury, M.R., Griera, A., Pennock, G.M., and Weikusat, I., 2017, The Relevance of Grain Dissection for Grain Size Reduction in Polar Ice: Insights from Numerical Models and Ice Core Microstructure Analysis: Frontiers in Earth Science, v. 5, p. 197, doi: 10.3389/feart.2017.00066.

Stern, L.A., Durham, W.B., and Kirby, S.H., 1997, Grain-size-induced weakening of H2O ices I and II and associated anisotropic recrystallization: Journal of Geophysical Research, v. 102, B3, p. 5313–5325, doi: 10.1029/96JB03894.

Thorsteinsson, T., Waddington, E.D., Taylor, K.C., Alley, R.B., and Blankenship, D.D., 1999, Strain-rate enhancement at Dye 3, Greenland: Journal of Glaciology, v. 45, no. 150, p. 338–345.

Thürmer, K., and Nie, S., 2013, Formation of hexagonal and cubic ice during low-temperature growth: Proceedings of the National Academy of Sciences of the United States of America, v. 110, no. 29, p. 11757–11762, doi: 10.1073/pnas.1303001110.

Vallon, M., Petit, J.-R., and Fabre, B., 1976, Study of an ice core to the bedrock in the accumulation zone of an alpine glacier: Journal of Glaciology, v. 17, no. 75, p. 13–28.

Waddington, E.D., Bolzan, J.F., and Alley, R.B., 2001, Potential for stratigraphic folding near ice-sheet centers: Journal of Glaciology, v. 47, no. 159, p. 639–648.

Wakahama, G., 1967, On the Plastic Deformation of Single Crystal of Ice: Physics of Snow and Ice: proceedings, v. 1, no. 1, p. 291–311.

Wang, Y., Chai, Y., Soutis, C., and Withers, P.J., 2019, Evolution of kink bands in a notched unidirectional carbon fibre-epoxy composite under four-point bending: Composites Science and Technology, v. 172, p. 143–152, doi: 10.1016/j.compscitech.2019.01.014.

Weertman, J., 1955, Theory of Steady‐State Creep Based on Dislocation Climb: Journal of Applied Physics, v. 26, no. 10, p. 1213–1217, doi: 10.1063/1.1721875.

Weertman, J., 1968, Diffusion law for the dispersion of hard particles in an ice matrix that undergoes simple shear deformation: Journal of Glaciology, v. 7, no. 50, p. 161–165.

Weertman, J., 1983, Creep Deformation of Ice: Annual Review of Earth and Planetary Sciences, v. 11, no. 1, p. 215–240, doi: 10.1146/annurev.ea.11.050183.001243.

Weikusat, I., Jansen, D., Binder, T., Eichler, J., Faria, S.H., Wilhelms, F., Kipfstuhl, S., Sheldon, S., Miller, H., Dahl-Jensen, D., and Kleiner, T., 2017, Physical analysis of an Antarctic ice core-towards an integration of micro- and macrodynamics of polar ice: Philosophical transactions. Series A, Mathematical, physical, and engineering sciences, v. 375, no. 2086, doi: 10.1098/rsta.2015.0347.

Weikusat, I., Kipfstuhl, S., Azuma, N., Faria, S.H., and Miyamoto, A., 2009, Deformation Microstructures in an Antarctic Ice Core (EDML) and in Experimentally Deformed Artificial Ice: Low Temperature Science, v. 3, no. 242, p. 295–310.

Weikusat, I., Kuiper, E.-J.N., Pennock, G.M., Kipfstuhl, S., and Drury, M.R., 2017, EBSD analysis of subgrain boundaries and dislocation slip systems in Antarctic and Greenland ice: Solid Earth, v. 8, no. 5, p. 883–898, doi: 10.5194/se-8-883-2017.

Weikusat, I., Miyamoto, A., Faria, S.H., Kipfstuhl, S., Azuma, N., and Hondoh, T., 2011, Subgrain boundaries in Antarctic ice quantified by X-ray Laue diffraction: Journal of Glaciology, v. 57, no. 201, p. 111–120, doi: 10.3189/002214311795306628.

Whalley, E., 1983, Cubic ice in nature: Journal of Physical Chemistry, v. 87, no. 21, p. 4174–4179.

Wilson, C.J.L., Burg, J.-P., and Mitchell, J.C., 1986, The origin of kinks in polycrystalline ice: Tectonophysics, v. 127, p. 27–48.

Wilson, C.J.L., Hunter, N.J.R., Luzin, V., Peternell, M., and Piazolo, S., 2018, The influence of strain rate and presence of dispersed second phases on the deformation behaviour of polycrystalline D 2 O ice: Journal of Glaciology, v. 65, no. 249, p. 101–122, doi: 10.1017/jog.2018.100.

Wilson, C.J.L., and Peternell, M., 2011, Evaluating ice fabrics using fabric analyser techniques in Sørsdal Glacier, East Antarctica: Journal of Glaciology, v. 57, no. 205, p. 881–894.

Wilson, C.J.L., and Peternell, M., 2012, Ice deformed in compression and simple shear: control of temperature and initial fabric: Journal of Glaciology, v. 58, no. 207, p. 11–22, doi: 10.3189/2012JoG11J065.

Wilson, C.J.L., Peternell, M., Piazolo, S., and Luzin, V., 2014, Microstructure and fabric development in ice: Lessons learned from in situ experiments and implications for

understanding rock evolution: Journal of Structural Geology, v. 61, p. 50–77, doi: 10.1016/j.jsg.2013.05.006.
Wilson, C.J.L., Russell-Head, D.S., Kunze, K., and Viola, G., 2007, The analysis of quartz c-axis fabrics using a modified optical microscope: Journal of microscopy, v. 227, p. 30–41.
Wilson, C.J.L., Russell-Head, D.S., and Sim, H.M., 2003, The application of an automated fabric analyzer system to the textural evolution of folded ice layers in shear zones: Annals of glaciology, v. 37, p. 7–17.
Wilson, C.J.L., and Zhang, Y., 1994, Comparison between experiment and computer modelling of plane-strain simple-shear ice deformation: Journal of Glaciology, v. 40, no. 134, p. 46–55.
Wolovick, M.J., Creyts, T.T., Buck, W.R., and Bell, R.E., 2014, Traveling slippery patches produce thickness-scale folds in ice sheets: Geophysical Research Letters, v. 41, no. 24, p. 8895–8901, doi: 10.1002/2014GL062248.
Wusatowska-Sarnek, A.M., Miura, H., and Sakai, T., 2002, Nucleation and microtexture developemt under dynamic recrystallization of copper: Materials Science and Engineering A323, p. 177–186.

Appendix

(A) Calibration curve for motor speed calculation

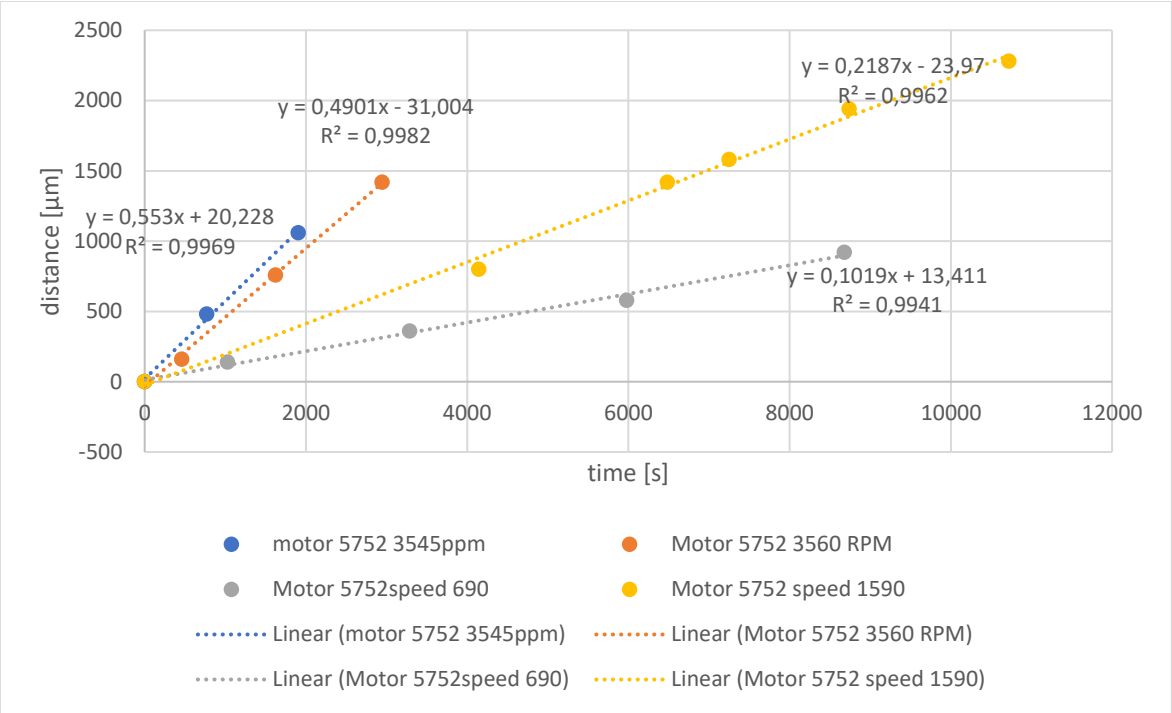

(B) Stress curves

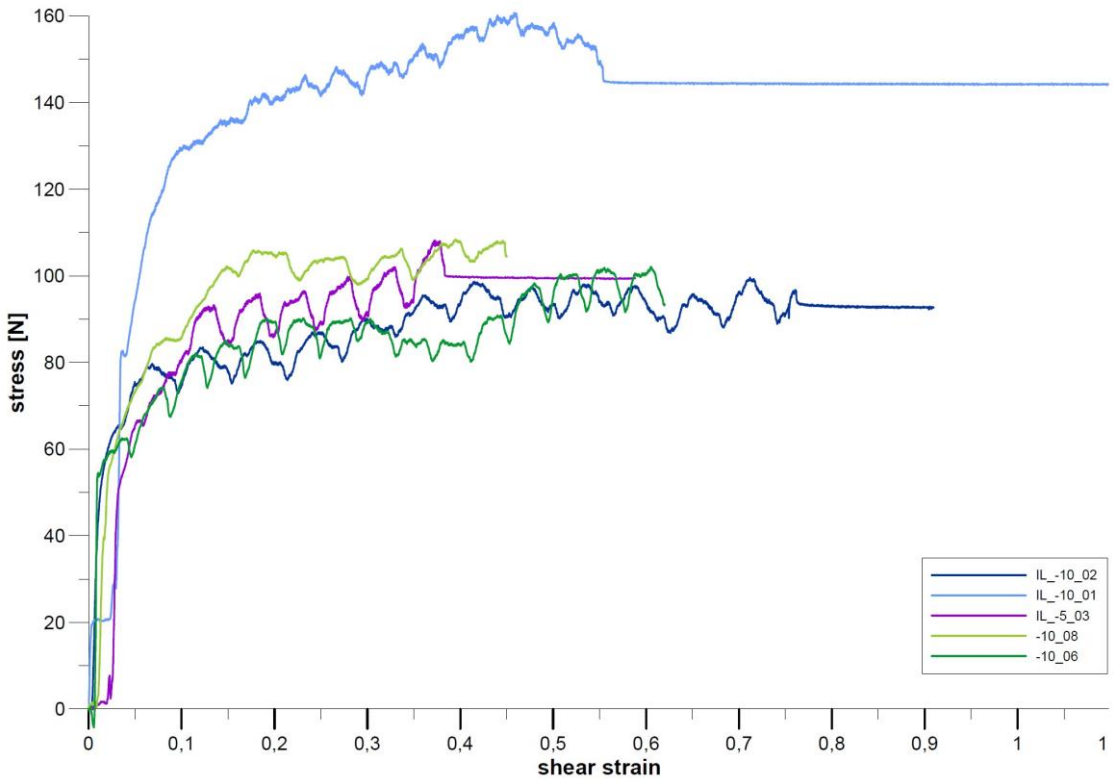

Note, stress data is not available for all deformation experiments.

(C) Comparisson before and after deformation/annealing (whole image)

-5_03

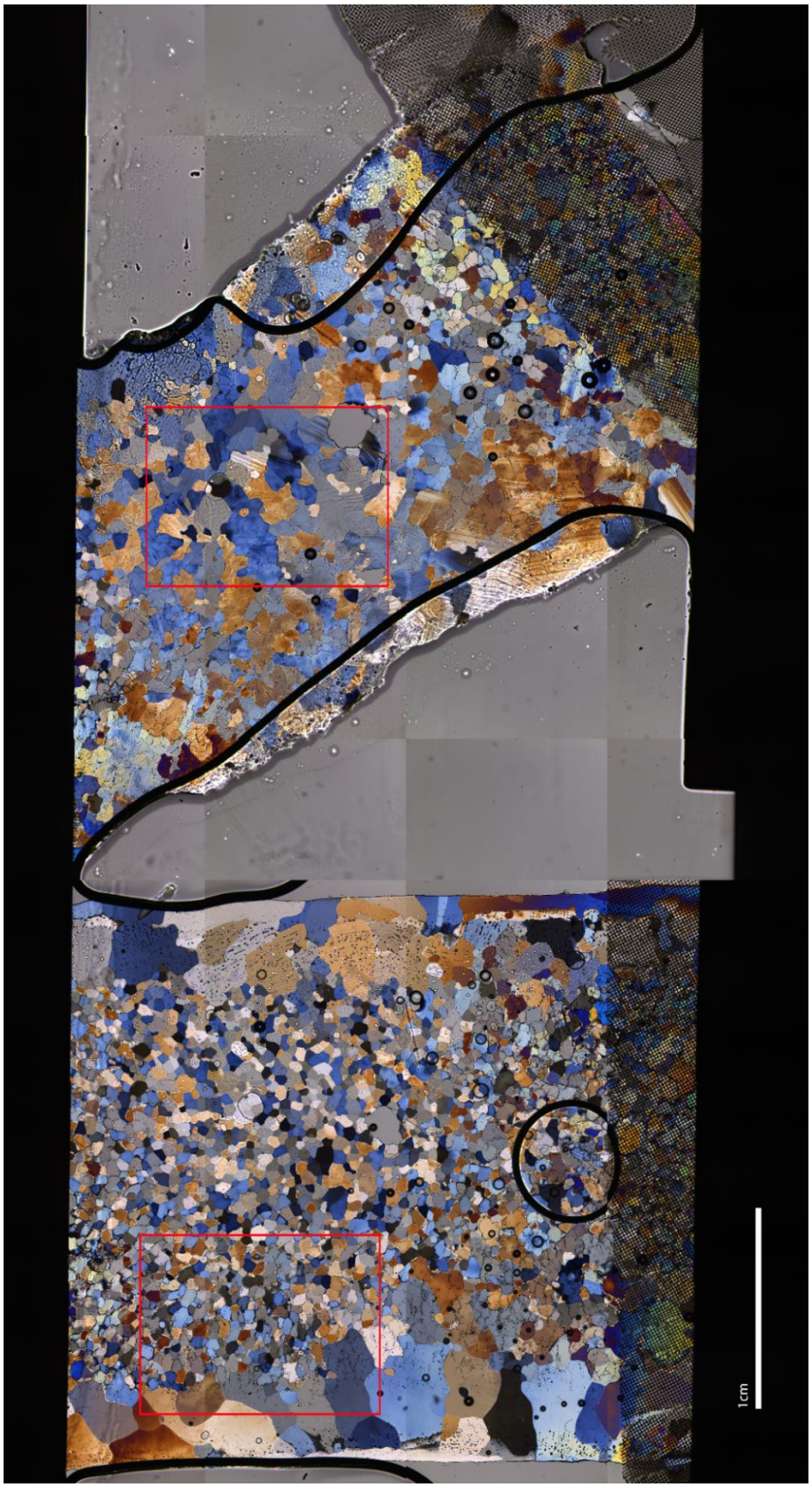

-10_02

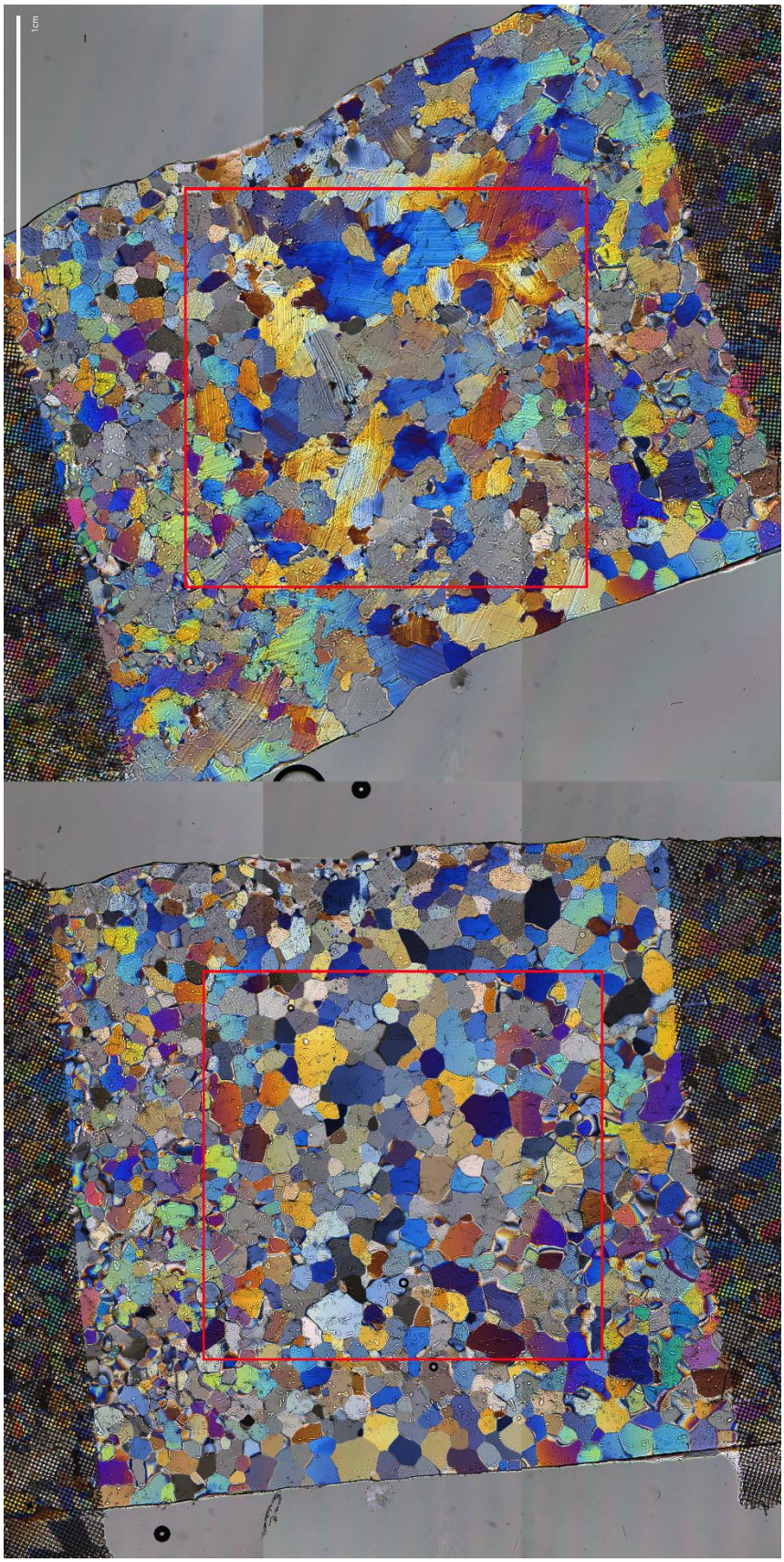

-10_06

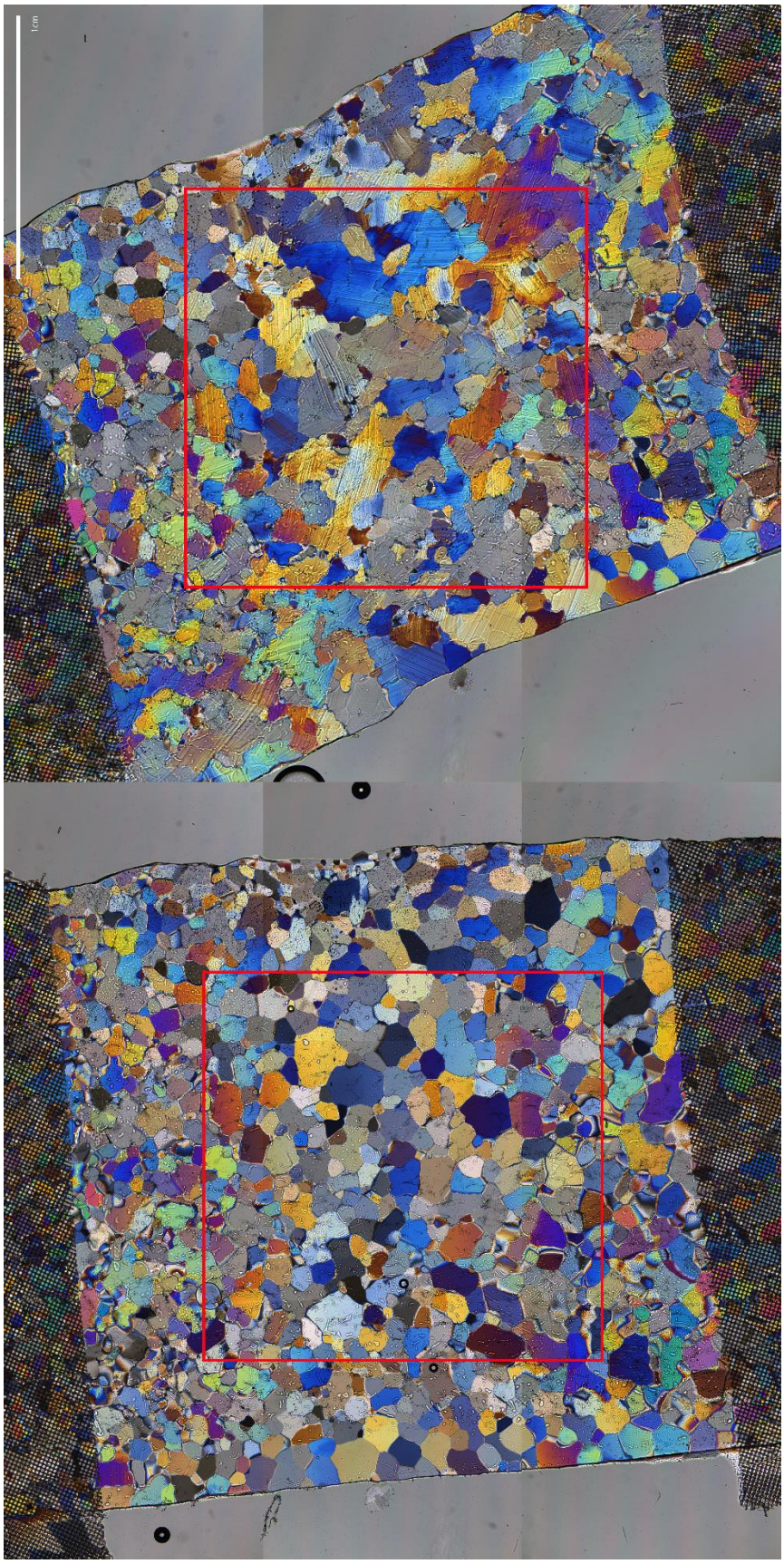

-10_08

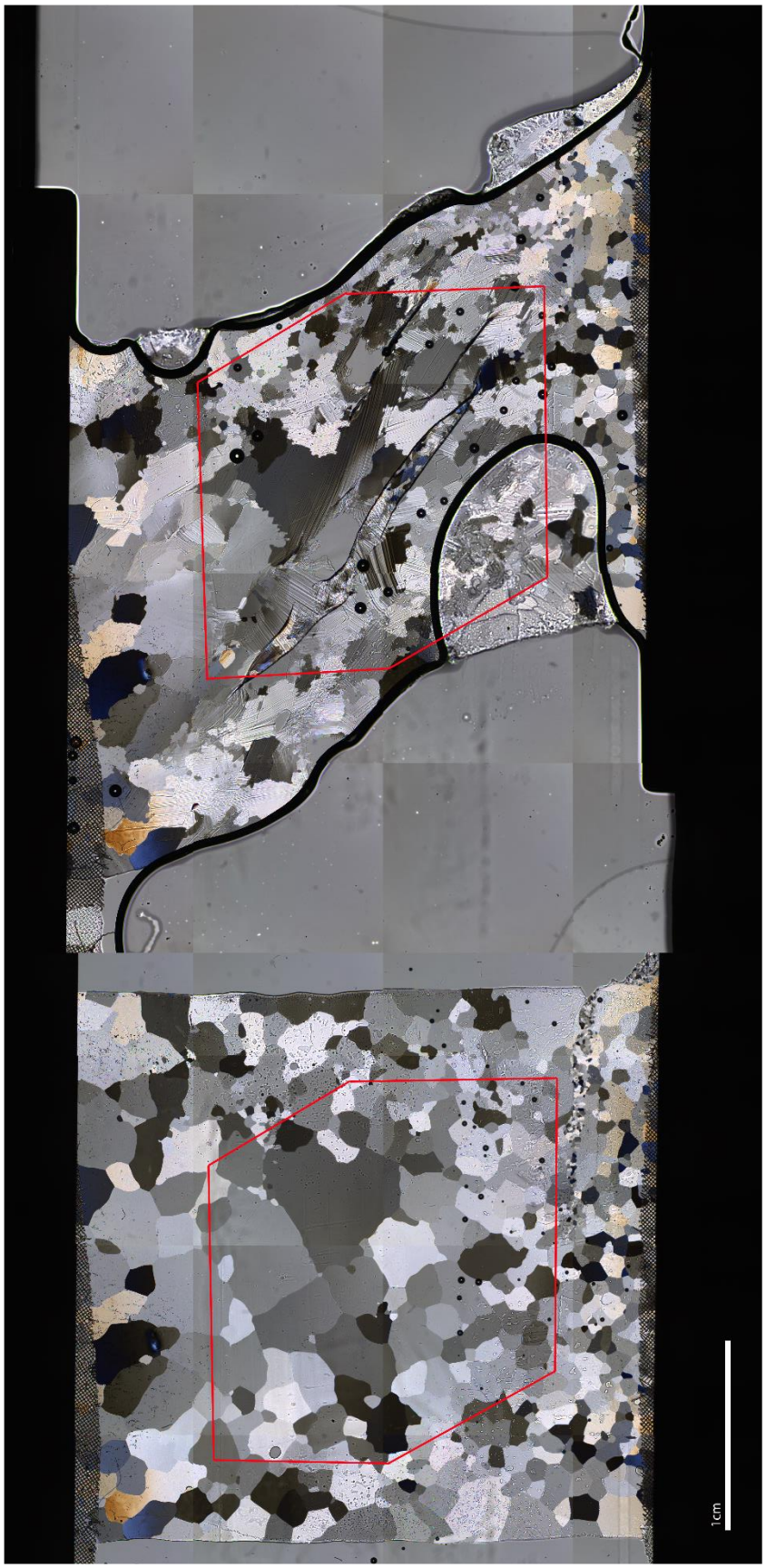

IL_-5_01

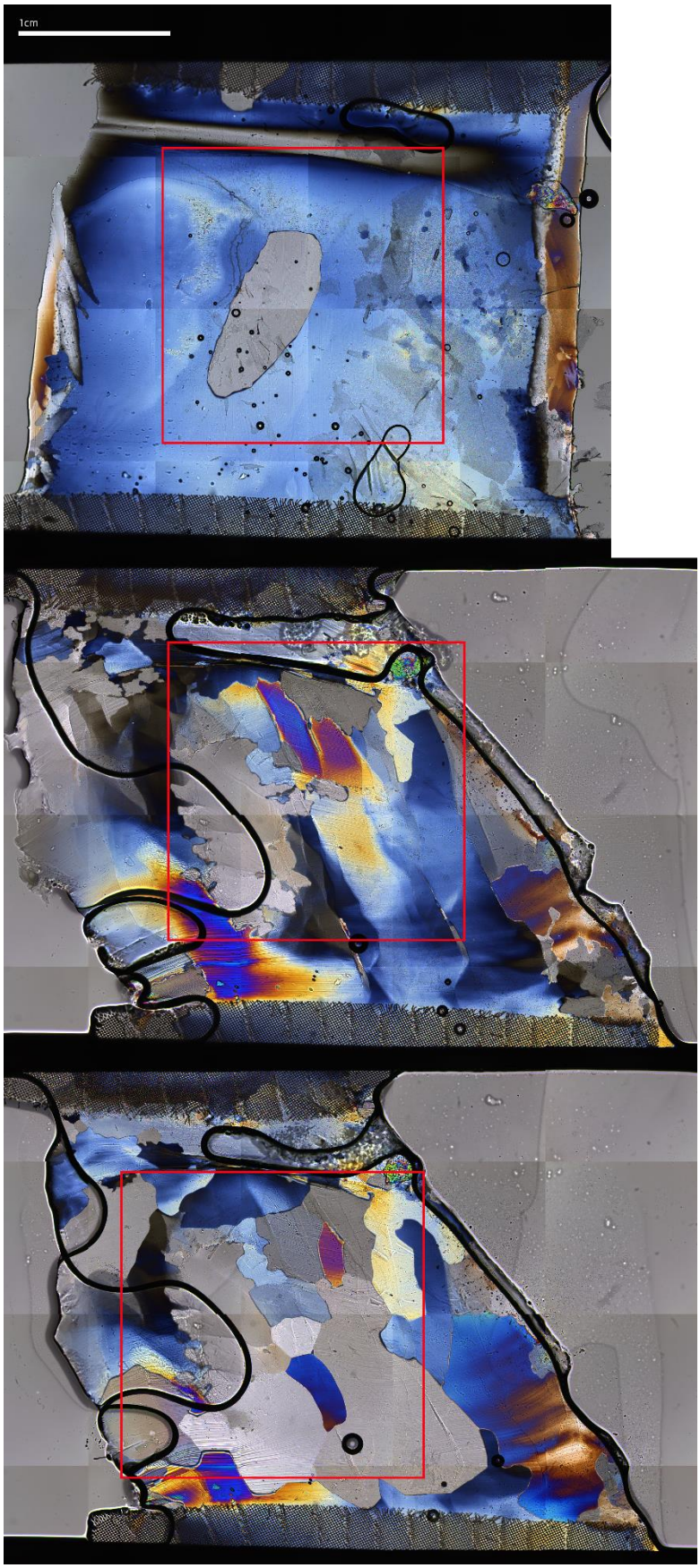

IL-5_03

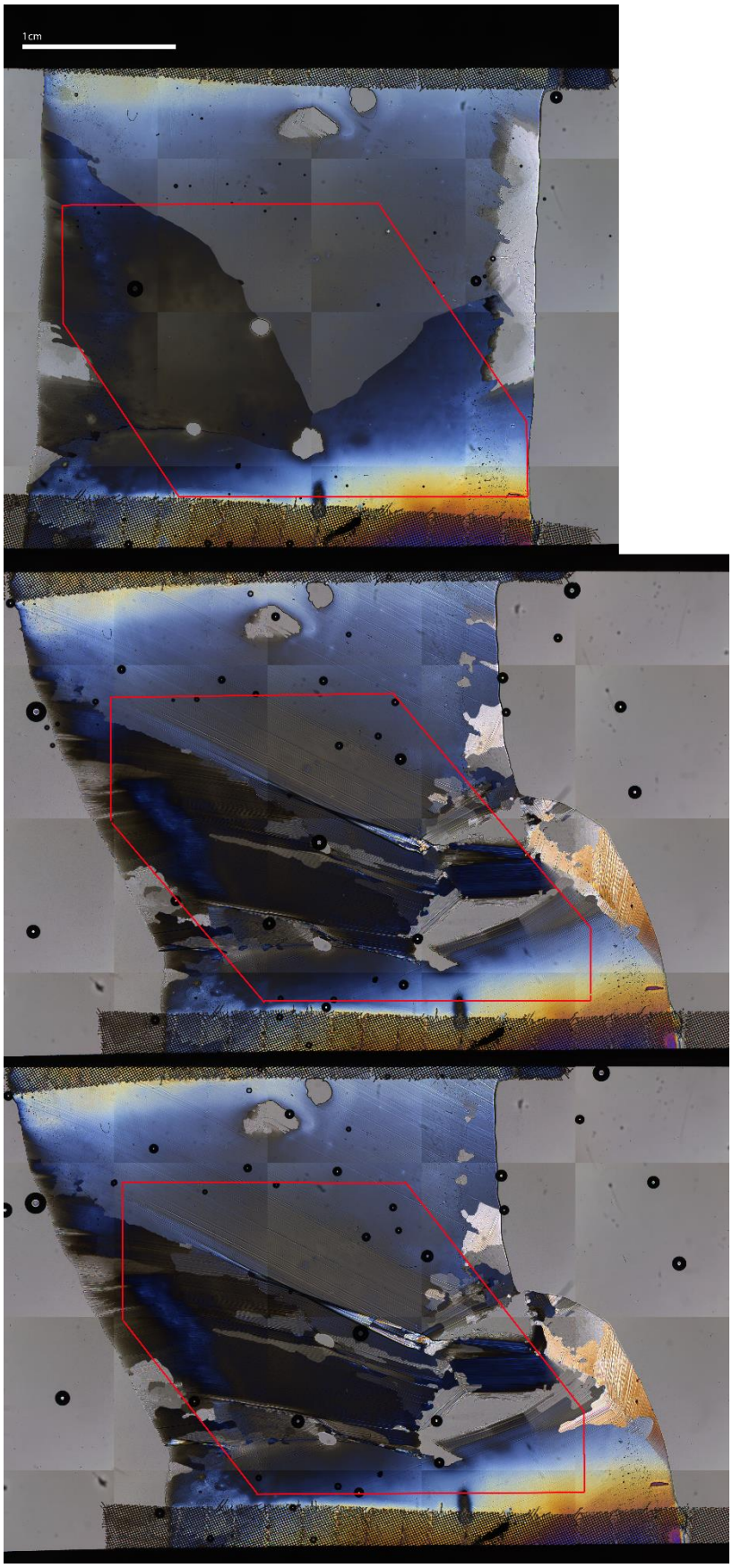

IL-10_01

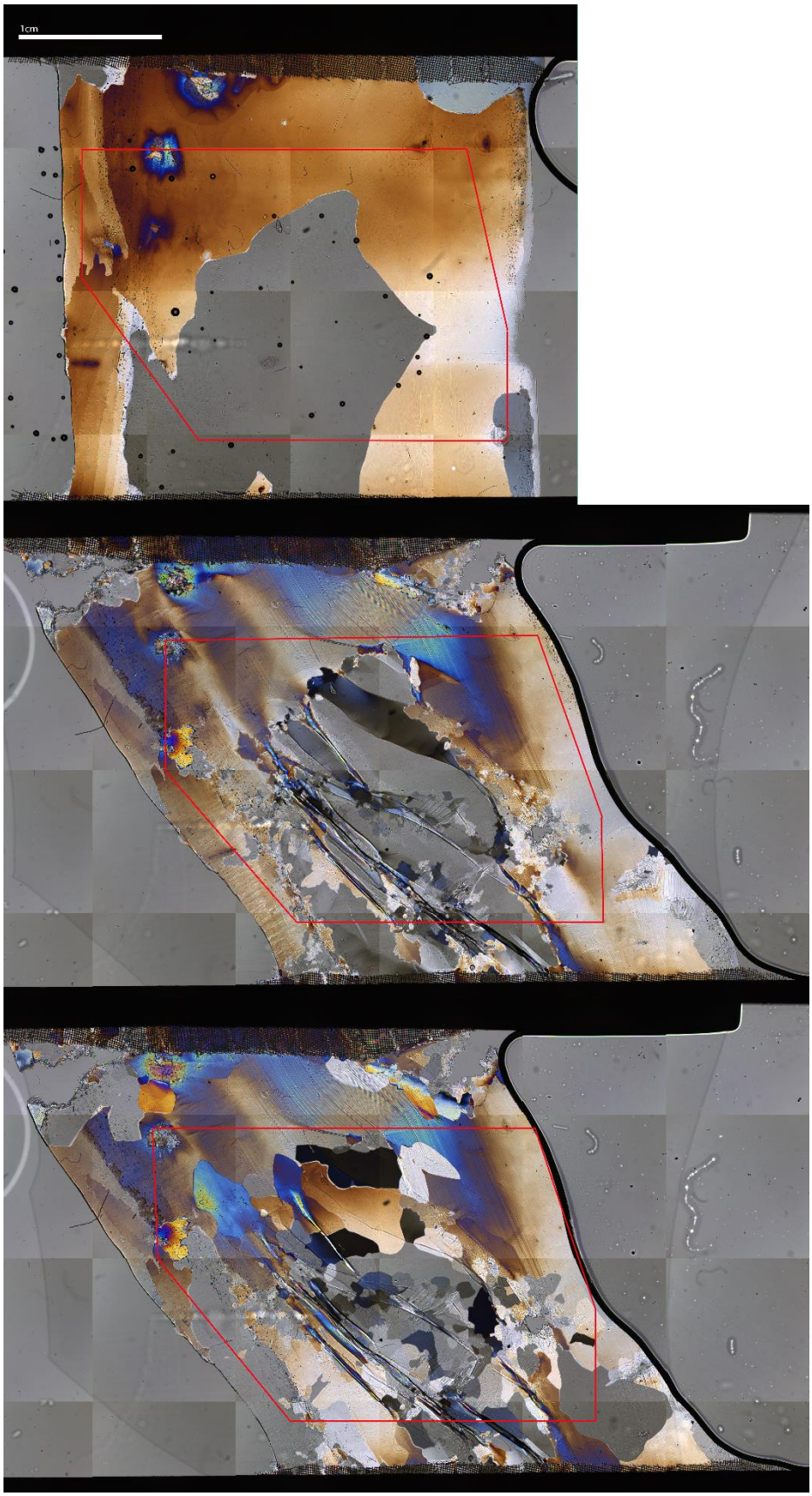

IL_-10_02

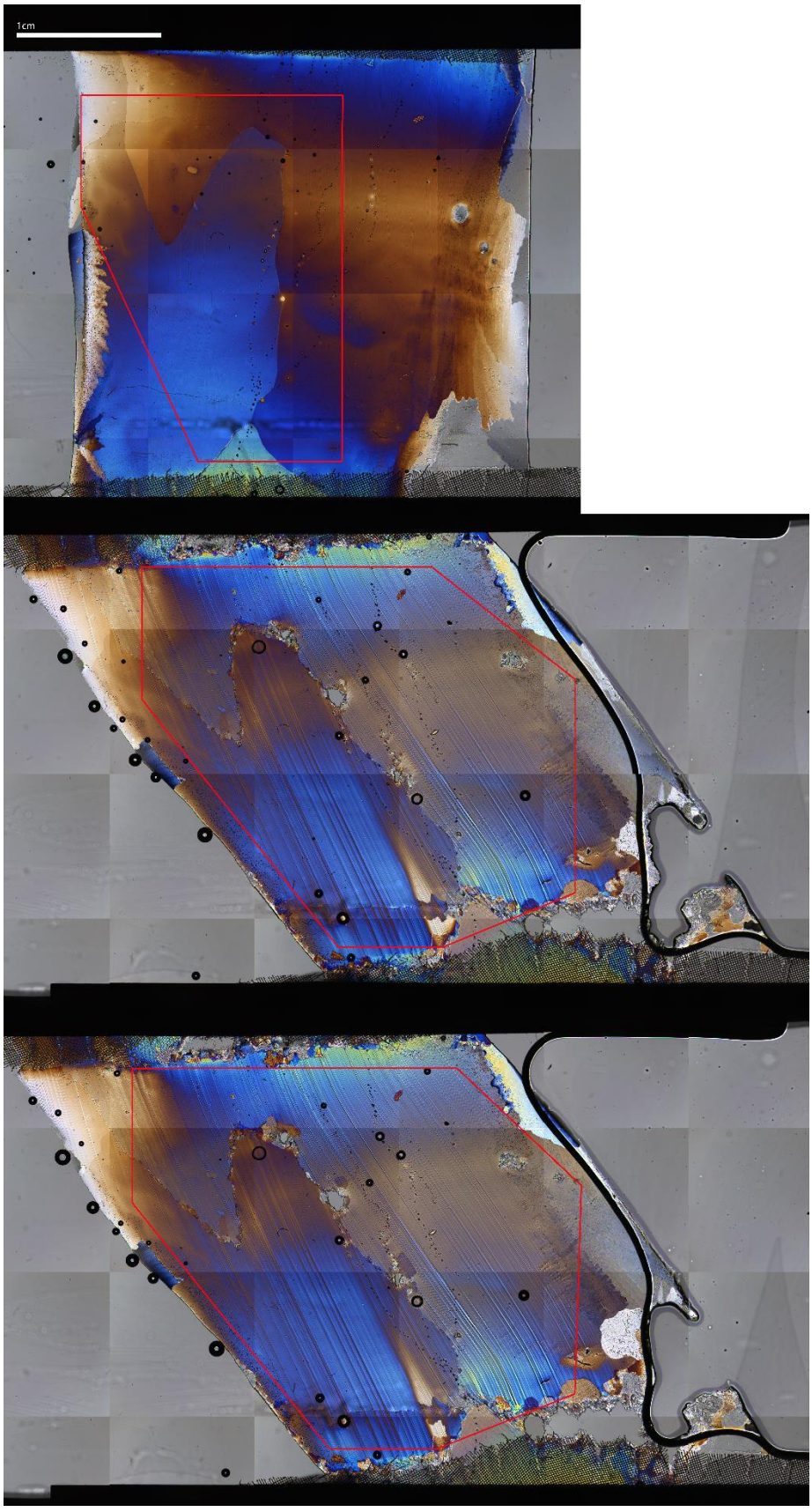

(D) Area fraction and number of grains in the analyzed area. Note that the fraction is calculated from the original captured image size which can be much bigger as the actual analyzed area for some experiments. Due to the adjustment of image size and position during the experiment IL_-10_02 the with FAME calculated data is split into three separate graphs (black box), for the full deformation with annealing all have to be seen as one.

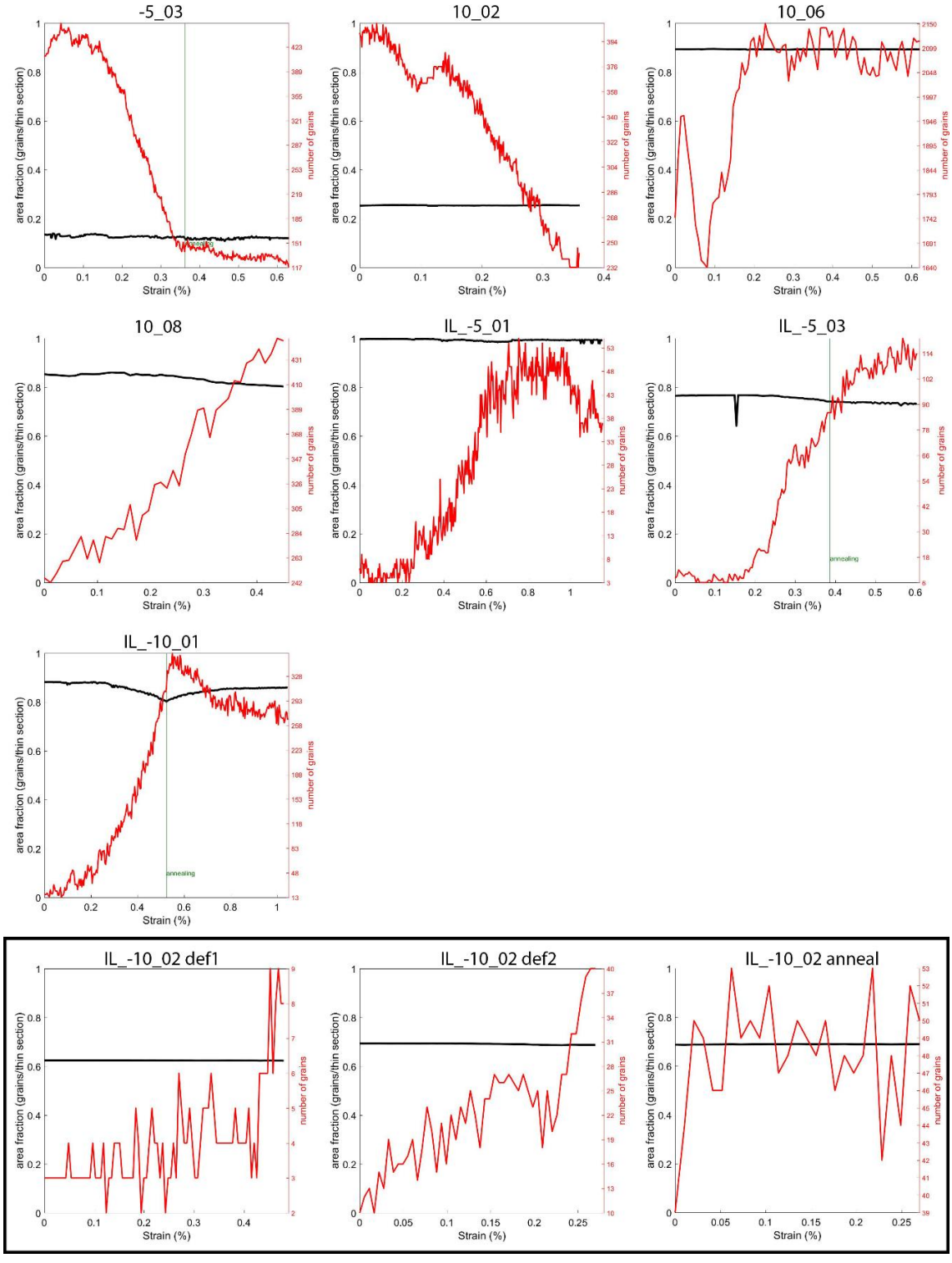

(E) Temperature of glass (blue) and substage (black) during experiments

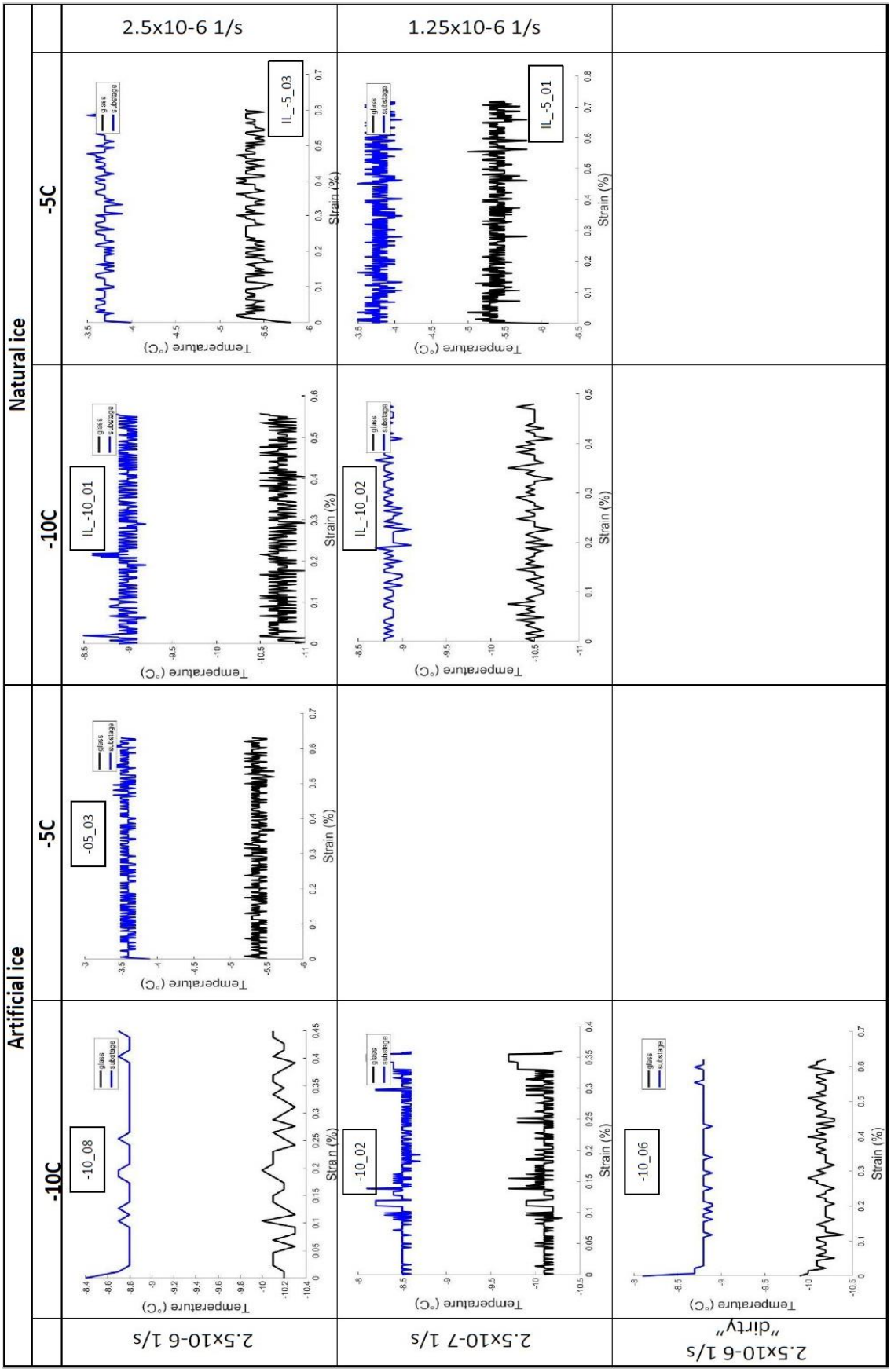

(F) Histogram with for angle distribution and normal distribution for angle abundance (top row) and distribution with subtracted normal distribution (bottom row)

-5_03

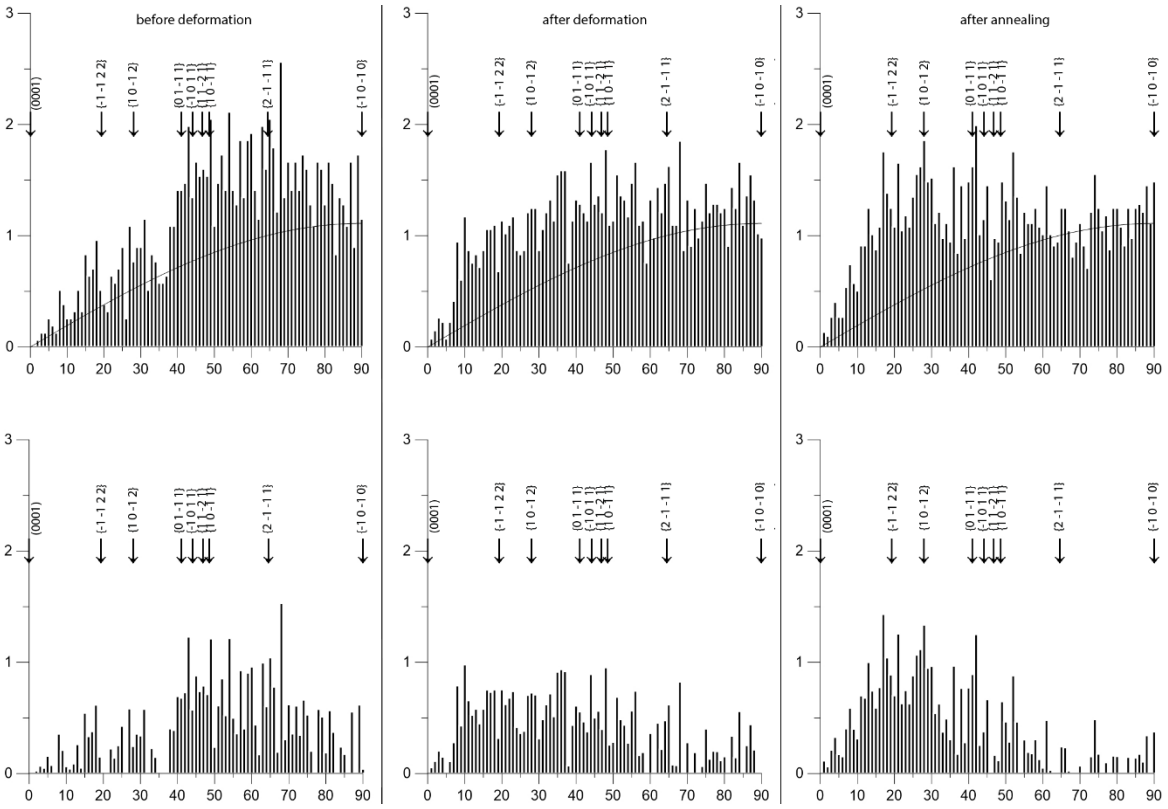

-10_02

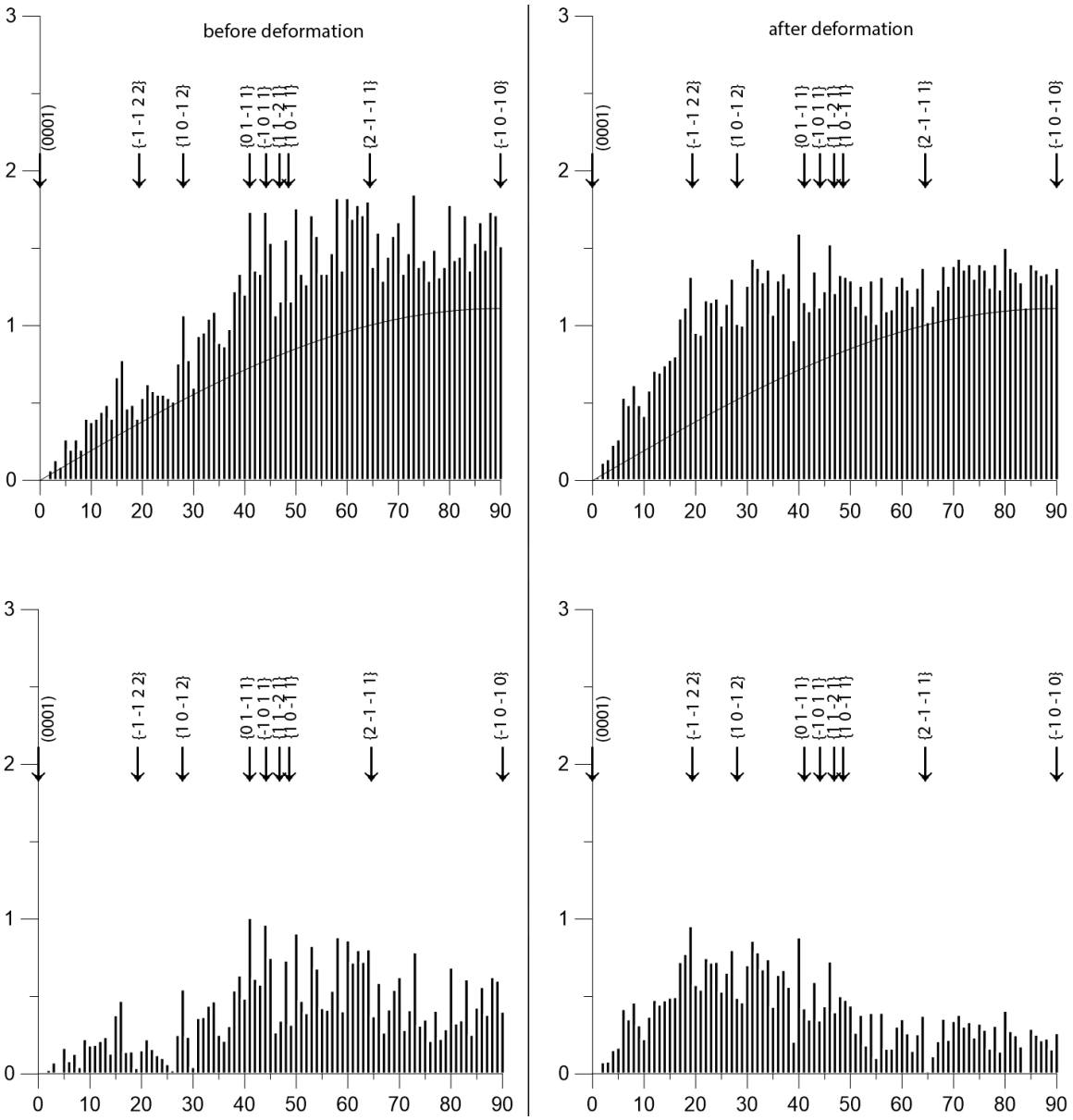
before deformation
after deformation
(0001)
{-1 -1 2 2}
{1 0 -1 2}
{0 1 -1 1}
{-1 0 1 1}
{1 1 -2 1}
{1 0 -1 1}
{2 -1 -1 1}
{-1 0 -1 0}
0
1
2
3
0 10 20 30 40 50 60 70 80 90

-10_06

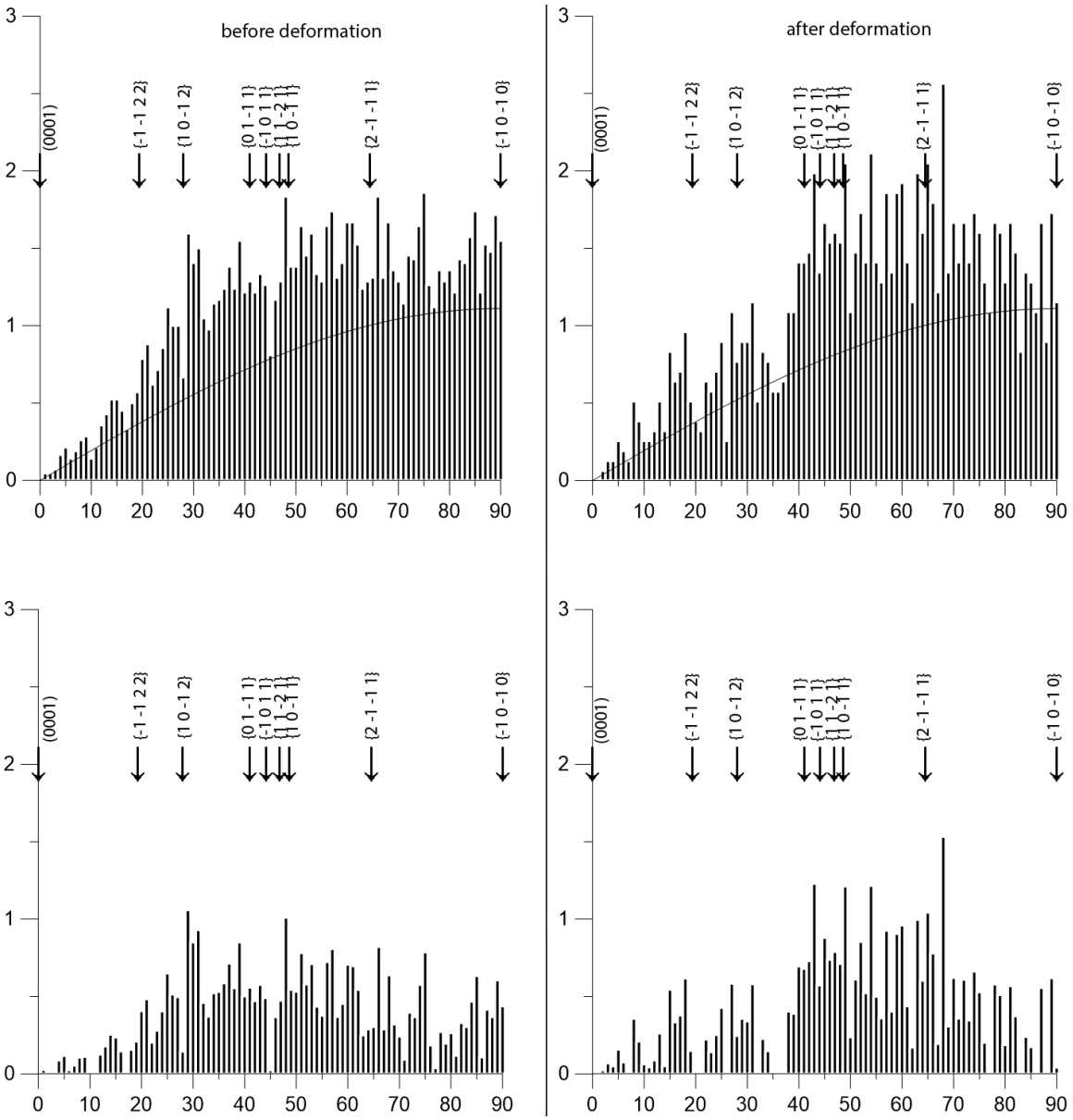
before deformation
after deformation
(0001)
{-1 -1 2 2}
{1 0 -1 2}
{0 1 -1 1}
{-1 0 1 1}
{1 1 -2 1}
{1 0 -1 1}
{2 -1 -1 1}
{-1 0 -1 0}

-10_08

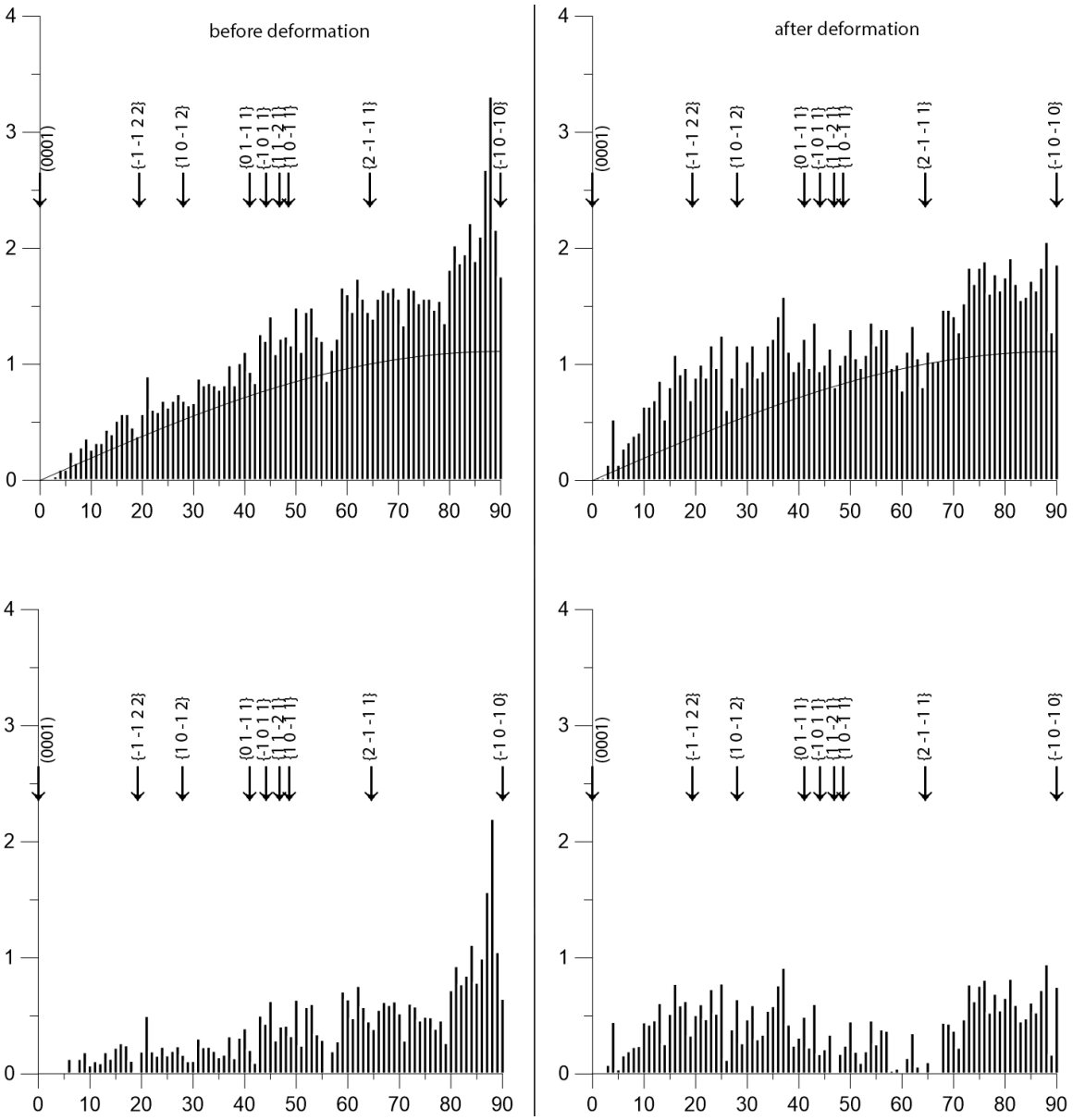
before deformation
after deformation
(0001)
{-1 -1 2 2}
{1 0 -1 2}
{0 1 -1 1}
{-1 0 1 1}
{1 1 -2 1}
{1 0 -1 1}
{2 -1 -1 1}
{-1 0 -1 0}

IL_-5_01

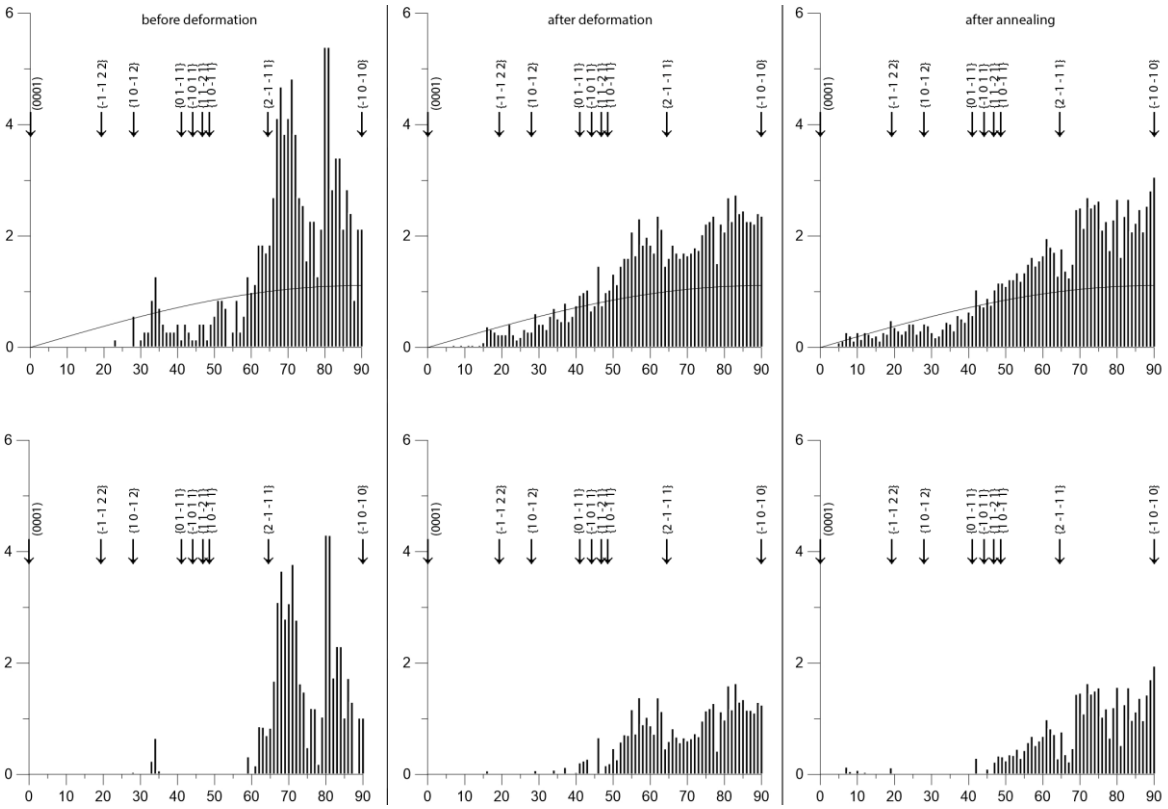
before deformation
after deformation
after annealing
(0001)
{-1-122}
{10-12}
{01-11}
{-1011}
{10-11}
{11-22}
{2-1-11}
{-10-10}

IL_-5_03

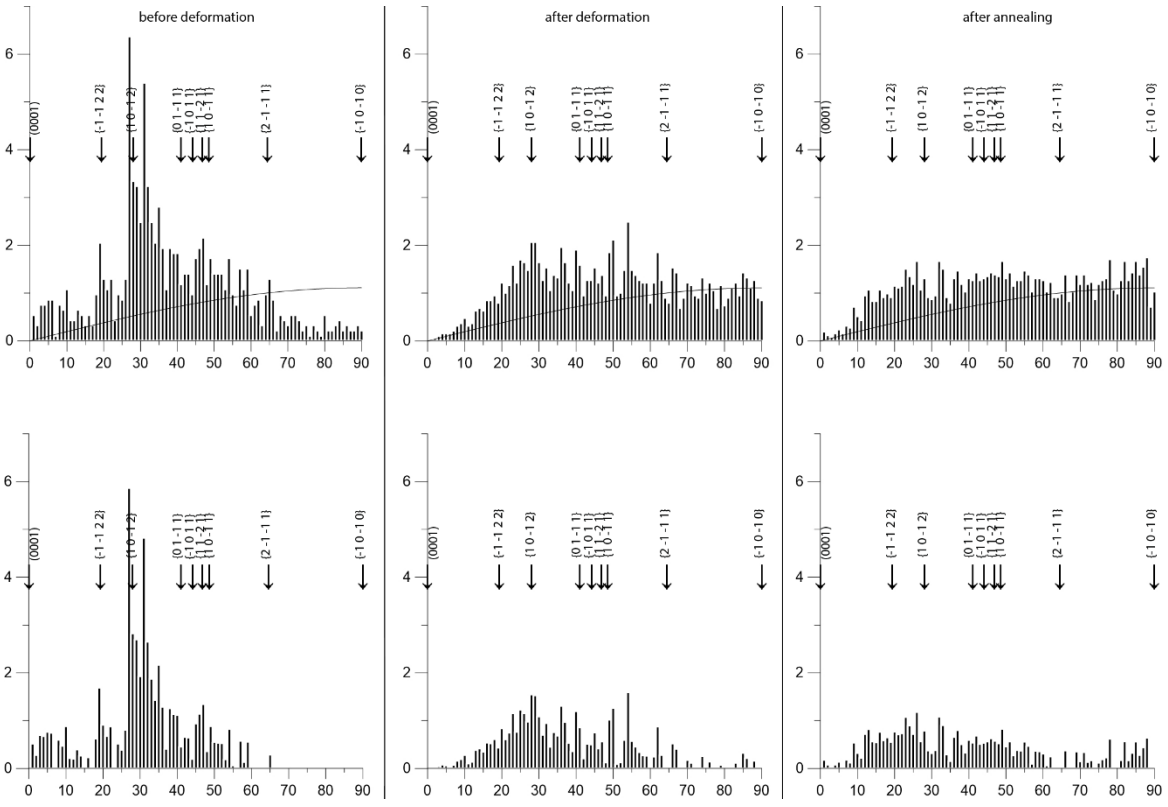
before deformation
after deformation
after annealing
(0001)
{-1-122}
{10-12}
{01-11}
{-1011}
{10-11}
{11-22}
{2-1-11}
{-10-10}

IL_-10_01

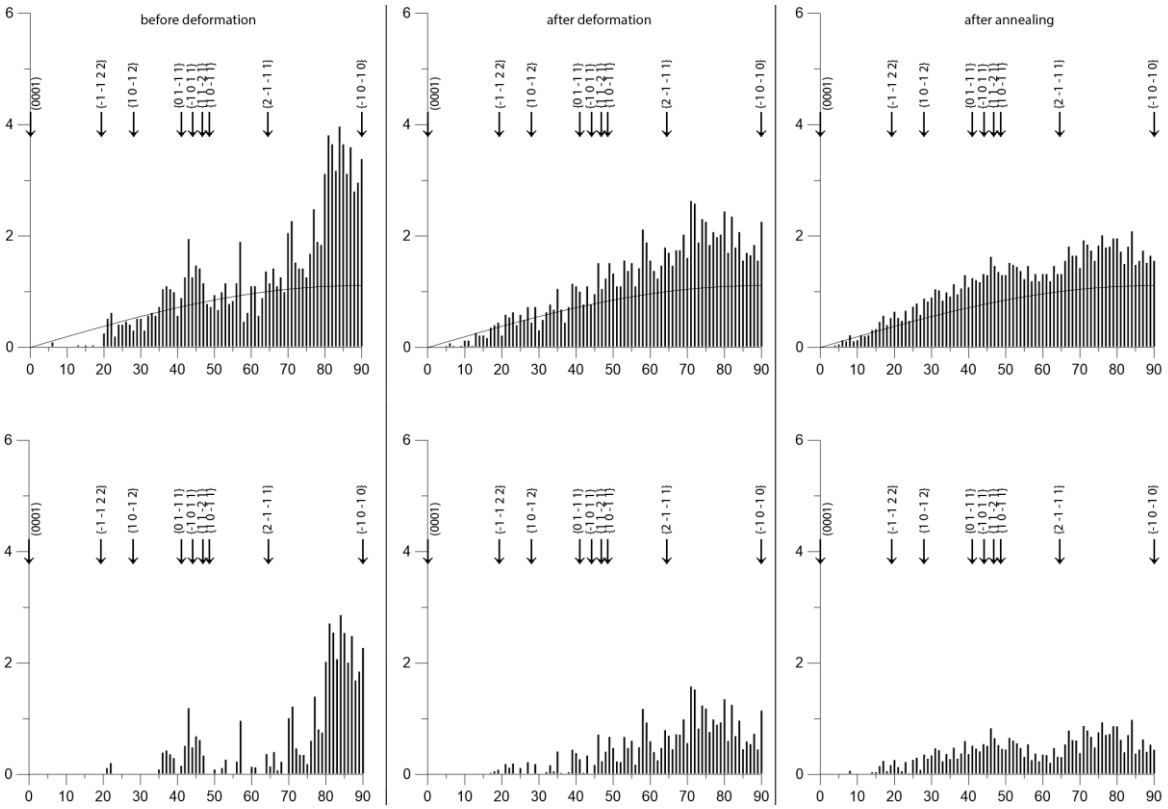

IL_-10_02

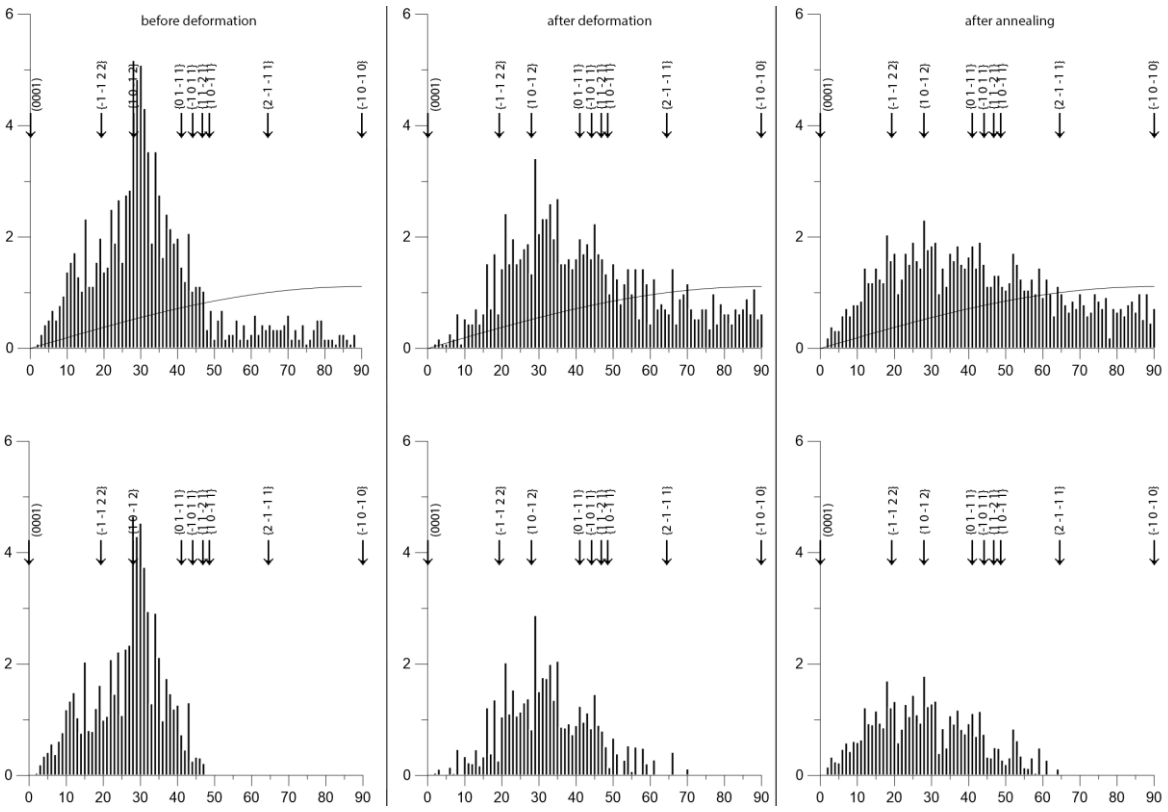

(G) Histogram of angle distribution after correction with normal distribution with fitted plots for determination of maxima

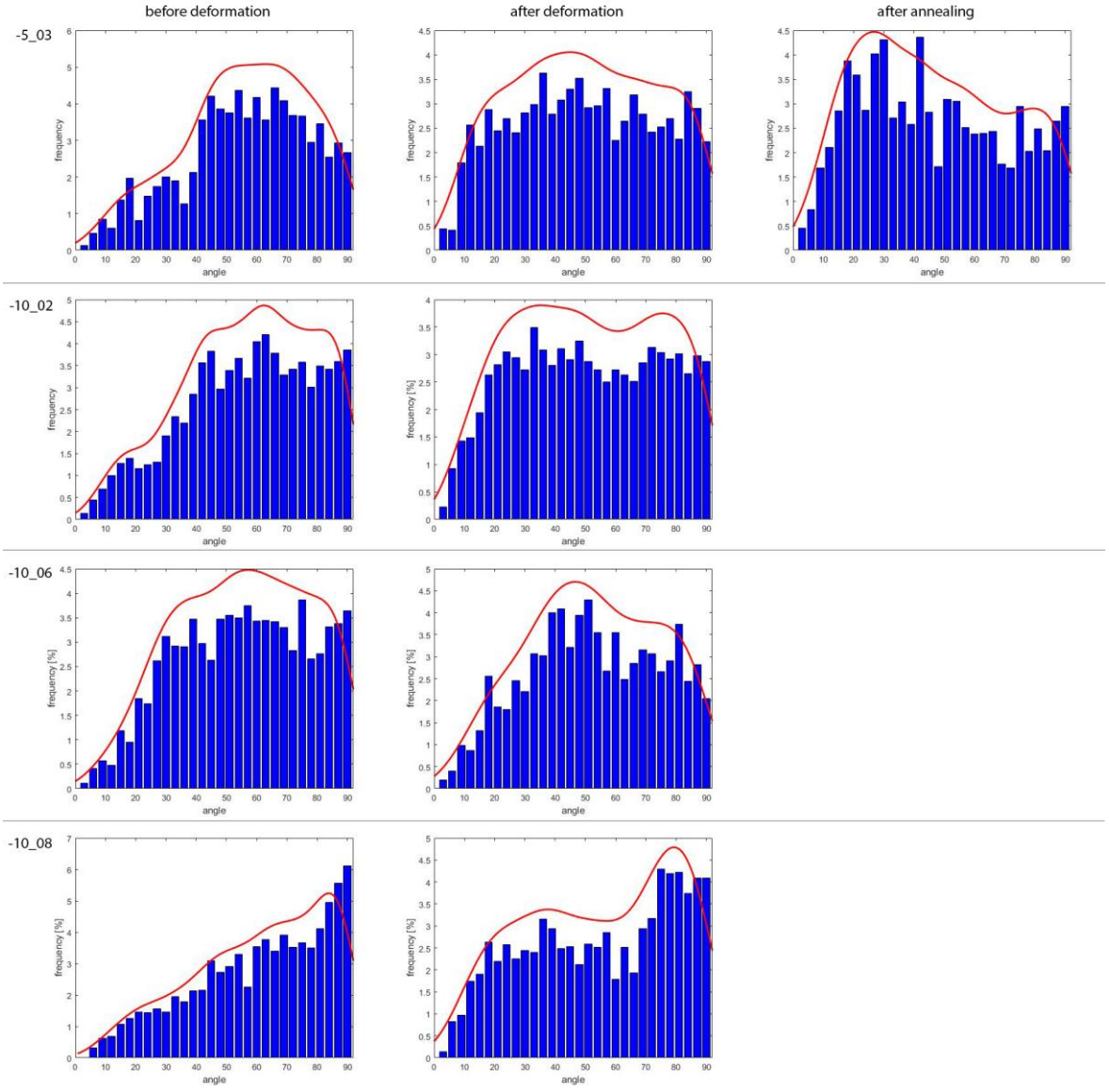

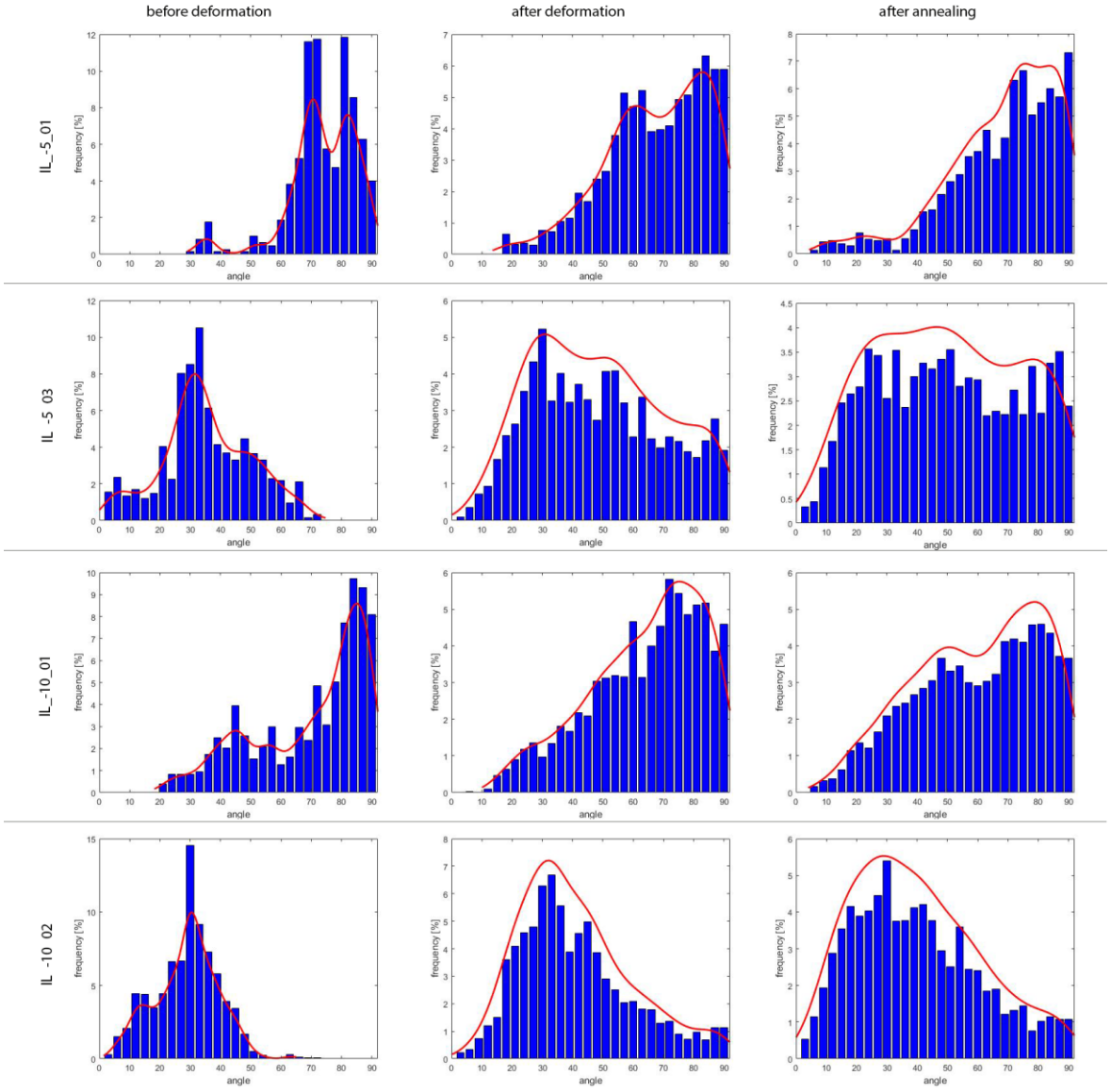
before deformation
after deformation
after annealing
IL_-5_01
IL -5 03
IL_-10_01
IL -10 02
frequency [%]
angle

(H) Triangle plots for the relation of the angle from the pole of the grain boundary to the <c>-axis without the correction for the standard distribution of the occurrence for each angle. First for the artificial ice samples and then for the natural ice samples. The smaller plots represent a detailed image of the newly grown grains after deformation and annealing respectively.

	before	after deformation	after annealing
-10_02	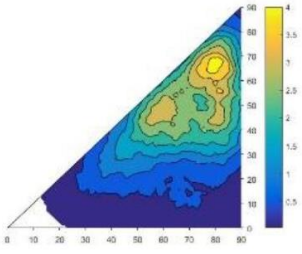	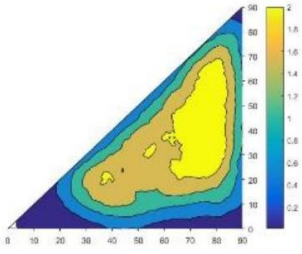	
-10_08	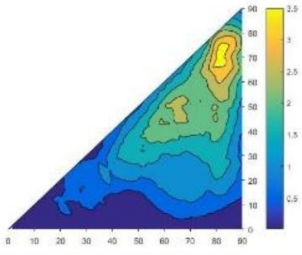	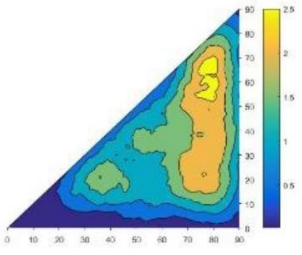	
-10_06	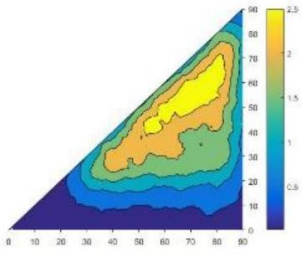	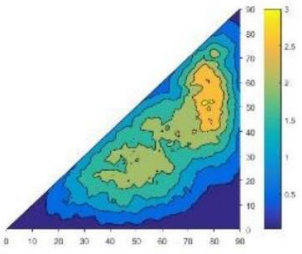	
-5_03	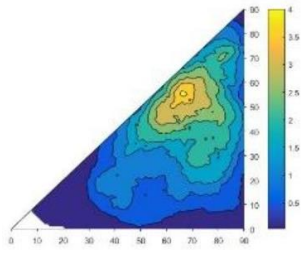	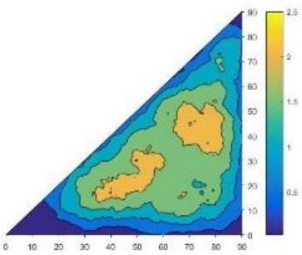	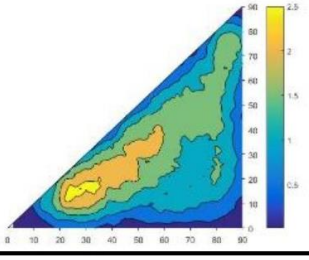

	before	after deformation	after annealing
IL_-10_01	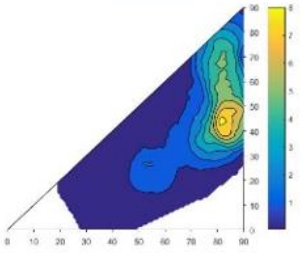	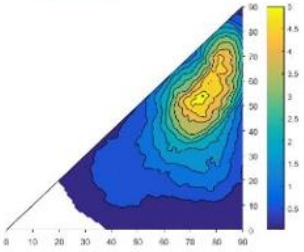	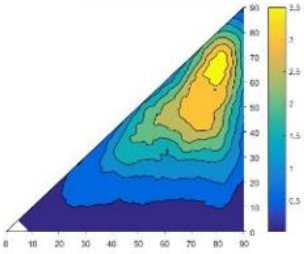
IL_-10_02	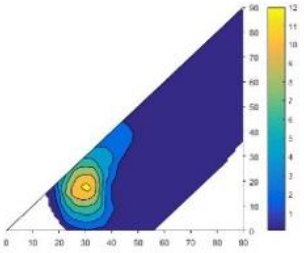	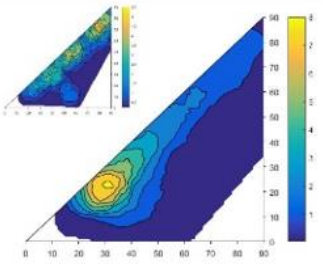	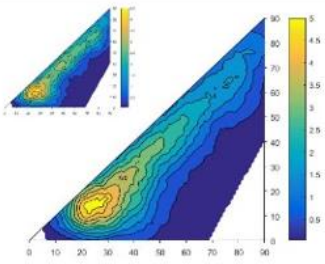
IL_-5_01	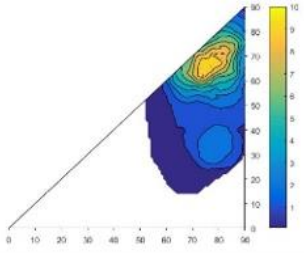	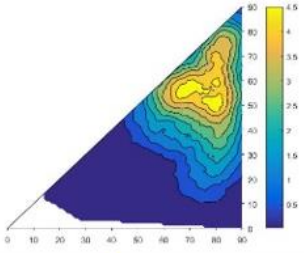	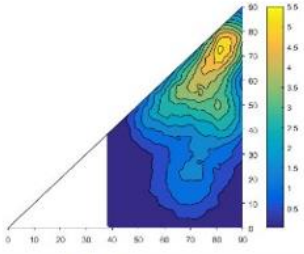
IL_-5_03	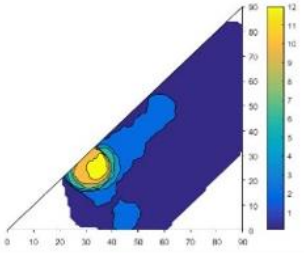	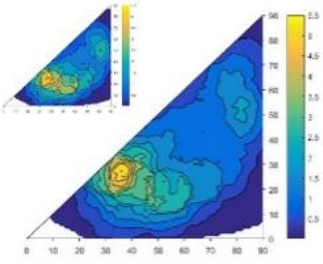	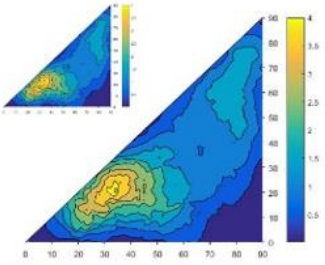

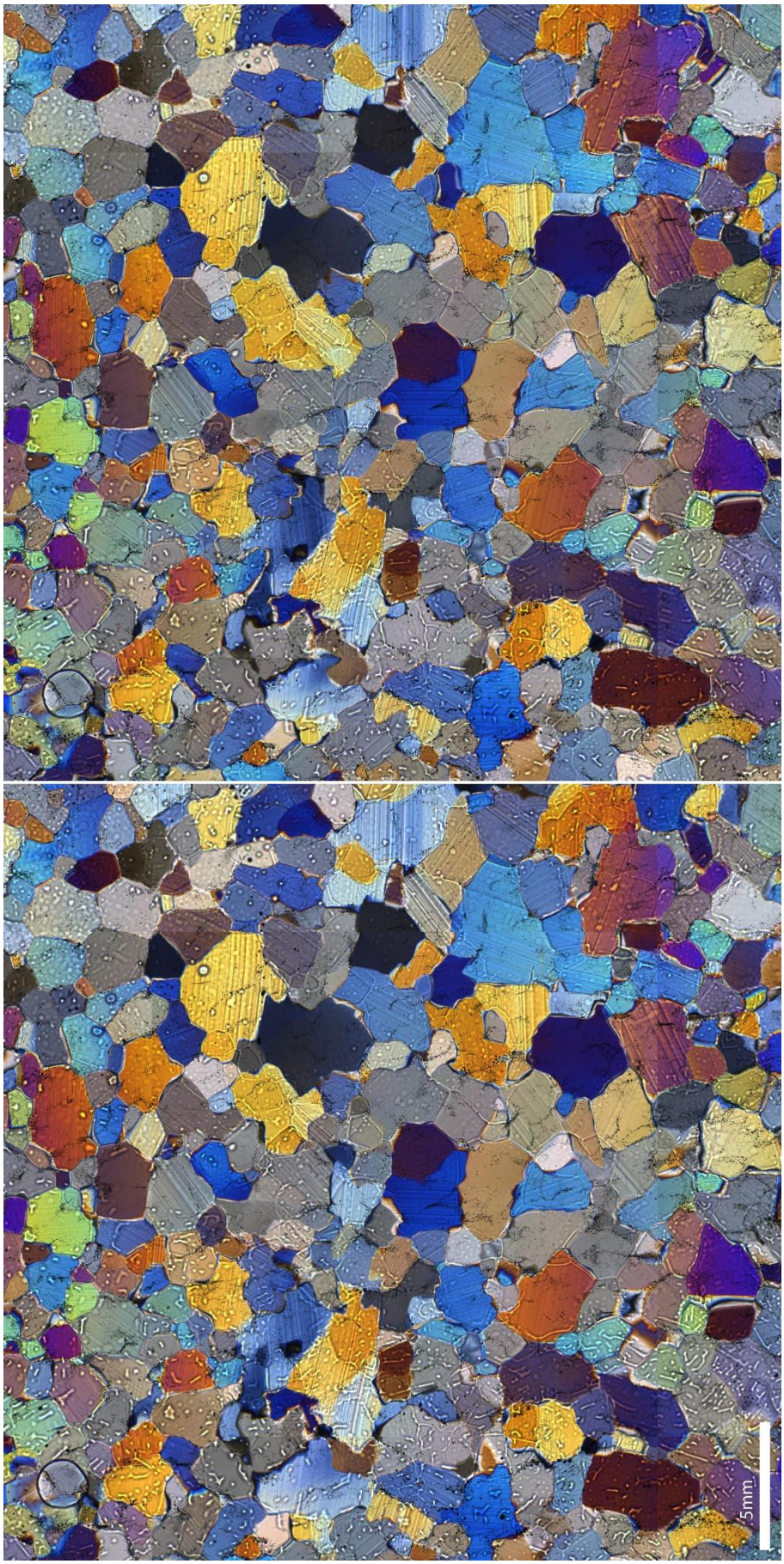

(I) -10_02 before (bottom) and after (top) image loss due to broken electric plug